

Radio Detection of Horizontal Extensive Air Showers

Zur Erlangung des akademischen Grades eines
DOKTORS DER NATURWISSENSCHAFTEN
von der KIT-Fakultät für Physik des
Karlsruher Instituts für Technologie (KIT)

genehmigte

DISSERTATION

von

Dipl.-Phys. Olga Kambeitz (geb. Pfeifer)
aus Abinsk (Russland)

Tag der mündlichen Prüfung: 03. Juni 2016
Referent: Prof. Dr. Dr. J. Blümer
Korreferent: Prof. Dr. U. Husemann

Radio Detection of Horizontal Extensive Air Showers

The radio measurements of horizontal extensive air showers opens the window for hybrid detection of high-energy cosmic rays with zenith angles above 60° , since with radio the electromagnetic component of air showers can be studied even when the particles are already absorbed in the atmosphere.

This work exhibits the first experimental proof that an array of antennas is sensitive to the radio emission of horizontal air showers, and of the large footprint of the radio emission from horizontal air showers, which was only predicted by simulations before. The size of the footprint rises with the zenith angle and the energy of the primary particle. It has been shown that radio signals of extensive air showers can be detected up to distances of 5 km to the shower axis of the extensive air shower. The large number of radio stations with clear signal above noise made it possible to study the characteristic shape of the lateral distribution function of horizontal air showers. The comparison of the amplitudes of the electric field of measured and simulated events results in a relative difference of 10% for simulations with proton primaries and of 13% for simulations with iron primaries. These relative differences lie within the uncertainty given by the antenna pattern of the radio stations. Hence, the Cherenkov cone valley, the elliptic shape and the sharp cut-off at the edges of the radio lateral distribution function could be reproduced with detailed CoREAS simulations.

A standard reconstruction for horizontal air showers for the Auger Engineering Radio Array (AERA) is established and made it possible to introduce a preliminary radio energy estimator for horizontal air showers. The application of this radio energy estimator on the AERA data sample results in a mean relative deviation of 49% from the primary energy determined by the Surface Detector. The application of the radio energy estimator for horizontal air showers to simulated events rendering the measured event sample results in a mean relative deviation of 22% for proton primaries and 21% for iron primaries relative to the input energy of the simulations, which is in agreement with the measurements considering the uncertainty of the energy determination by the surface array. The proven independence of the radio amplitude from the elemental composition makes the radio lateral distribution of horizontal air showers a good energy estimator. However, it is shown that using the hybrid detection of radio and particles of horizontal air showers also a composition determination can be achieved. In addition, it is discussed that the large-scale radio detection of horizontal air showers is possible. A future application can be the search for horizontal air showers initiated by high-energy neutrinos.

Radiodetektion horizontaler ausgedehnter Luftschauer

Die Radiodetektion von horizontalen Luftschauern ermöglicht die hybride Detektion von hochenergetischer Kosmischer Strahlung bei Zenitwinkeln von mehr als 60° , da mit der Radiodetektion die elektromagnetische Komponente des Schauers untersucht werden kann, selbst wenn die Teilchen in der Atmosphäre absorbiert wurden.

Diese Arbeit stellt den ersten experimentellen Beweis dafür dar, dass ein Feld von Radioantennen sensitiv auf die Radioemission von horizontalen Schauern ist und den ersten experimentellen Beweis für den großen Fußabdruck des Radiosignals, der zuvor nur durch Simulationen vorhergesagt wurde. Die Größe des Fußabdrucks nimmt mit steigendem Zenitwinkel und steigender Energie des Primärteilchens zu. Es wurde gezeigt, dass das Radiosignal von ausgedehnten Luftschauern in einem Abstand von bis zu 5 km zur Schauerachse detektiert werden kann. Die große Anzahl an Radiostationen mit klarem Signal über Rauschlevel hat es möglich gemacht die charakteristische Lateralverteilung von horizontalen Luftschauern zu untersuchen. Das Tal des Cherenkov-Kegels, die elliptische Struktur und das abrupte Abbrechen des Signals an der Kante der Lateralverteilung konnte mit detaillierten CoREAS-Simulationen reproduziert werden. Der Vergleich der Amplituden der gemessenen Ereignisse mit den simulierten Ereignissen, die der gemessenen Selektion der Ereignisse entsprechen, hat eine relative Abweichung von 10% für Simulationen mit Protonprimärteilchen und 13% für Simulationen mit Eisenprimärteilchen ergeben. Die relativen Abweichungen liegen innerhalb der Unsicherheiten, die durch das Antennen-Strahlungsdiagramm der Radiostationen gegeben sind.

Eine Standardrekonstruktion für horizontale Luftschauer für das Auger Engineering Radio Array (AERA) wurde etabliert und hat es möglich gemacht einen vorläufigen Radioenergieschätzer für horizontale Luftschauer einzuführen. Die Anwendung des Radioenergieschätzers auf AERA-Daten hat eine mittlere relative Abweichung von 49% im Vergleich zur Energiebestimmung durch die Oberflächendetektoren ergeben. Die Anwendung des Radioenergieschätzers auf die simulierten Ereignisse hat eine relative Abweichung von 21% für simulierte Ereignisse mit Protonprimärteilchen und 22% für simulierte Ereignisse mit Eisenprimärteilchen ergeben. Die Abweichungen sind mit den relativen Abweichungen der Energiebestimmung durch den Oberflächendetektor vereinbar. Die gezeigte Unabhängigkeit der Amplitude des Radiosignals von dem Primärteilchen macht die Lateralverteilung von horizontalen Luftschauern zu einem guten Energieschätzer. Zudem wurde gezeigt, dass durch eine hybride Detektion der Radioemission und der Teilchen von horizontalen Luftschauern eine Bestimmung der Zusammensetzung der Kosmischen Strahlung erreicht werden kann. Zusätzlich wurde gezeigt, dass die Radiodetektion von horizontalen Luftschauern mit einem großskaligen Radiodetektor möglich ist und eine Anwendung in der Zukunft die Suche nach horizontalen Luftschauern sein kann, die durch hochenergetische Neutrinos ausgelöst wurden.

Contents

1. Introduction	1
2. Cosmic Rays and Extensive Air Showers	3
2.1. Cosmic Rays	3
2.1.1. Cosmic Ray Flux	3
2.1.2. Composition	5
2.2. Extensive Air Showers	6
2.3. Radio Emission of Extensive Air Showers	8
2.3.1. Mechanism	8
2.3.2. Experiments	9
2.4. Horizontal Air Showers	11
2.4.1. Radio Detection of Horizontal Air Showers	13
2.5. Neutrino Detection	14
3. The Pierre Auger Observatory and AERA	17
3.1. Surface Detector	18
3.2. Fluorescence Detector	18
3.3. Auger Muons and Infill for the Ground Array	21
3.4. AERA - The Auger Engineering Radio Array	21
4. Analysis Methods and Tools	25
4.1. <u>Offline</u>	25
4.2. Monte Carlo Simulations	27
4.3. Lateral Distribution Functions	28
5. Preparatory Studies	29
5.1. Reconstruction Efficiency	29
5.1.1. Reconstruction Efficiency - Vertical Events	30
5.1.2. Reconstruction Efficiency - Horizontal Events	33
5.2. Prototype Stations	36
5.2.1. Horizontal Component	36
5.2.2. Prototypes Installed at the Auger Site	37
6. Reconstructed Data Sample and Data Selection	43
6.1. RdObsever	43

6.2. RdHASObserver	47
6.3. CoREAS Simulations	52
6.4. The Horizontal Polarisation Component	56
7. Analysis of Horizontal Air Showers Detected by AERA	59
7.1. Shower Footprint	59
7.2. Multi-Station Events	60
7.3. High-Energy Events	64
7.4. Events with Zenith Angle Larger than 80°	65
7.5. Comparison of Measured and Simulated Amplitudes	67
7.5.1. Example Event with Core Shift	67
7.5.2. Example Events with Energy Shift	72
7.5.3. Shower Composition	78
7.5.4. Zenith Angle	81
7.5.5. Energy	84
7.5.6. Core Position Relative to AERA	87
7.5.7. Antenna Type	88
7.5.8. Mean Lateral Distribution	89
7.6. Detection Thresholds of Horizontal Air Showers	91
7.7. Efficiency Considerations	93
7.8. Summary	93
8. Physics with Horizontal Air Showers Detected by AERA	95
8.1. Energy Estimation of Horizontal Air Showers	95
8.1.1. Radiation Energy of Horizontal Air Showers	95
8.1.2. Primary Energy	101
8.2. Composition Determination of Horizontal Air Showers	108
8.3. Large-Scale Array of Radio Detectors	116
8.4. Detection of Neutrinos	121
8.5. Summary	126
9. Conclusion	127
Appendix	137
A. Tables	139
A.1. ModuleSequence - Data	139
A.2. ModuleSequence - Simulation	141

1. Introduction

Particles from outer space reaching the Earth are a source of fascination for astroparticle physicists. The balloon experiment of Victor F. Hess [1] about 100 years ago raised questions on ionising radiation measured in the atmosphere. Robert A. Millikan later called this radiation cosmic rays [2]. In cosmic rays the muon [3], the pion [4], the kaon [5] and the first antiparticle, the positron [6], were first detected and so elementary particle physics was born. The energies of primary particles in cosmic rays can exceed by far the energies physicists are able to generate in particle accelerators like the Large Hadron Collider [7].

Nowadays questions about the acceleration mechanisms, the origin and the propagation of cosmic rays are still to be answered with satellite experiments, balloon experiments and ground based experiments. The world's largest cosmic ray experiment is the Pierre Auger Observatory in Argentina [8]. Analyses of the data taken by the Pierre Auger Observatory during 15 years of operation confirmed the suppression of the cosmic ray flux around 5×10^{19} eV, placed limits on the photon and neutrino components of the flux and found a large-scale dipole anisotropy for energies above 3×10^{18} eV [9]. There are still open questions and therefore, the motivation for an upgrade of the Pierre Auger Observatory are the mass composition, the origin of the flux suppression, the search for a flux contribution of protons and the study of hadronic multiparticle production at the highest energies [9].

One enhancement for studying lower energies at the Pierre Auger Observatory is the Auger Engineering Radio Array (AERA) [10]. AERA is a detector of more than 150 radio antennas spread over an area of 17 km² sensitive to the radio emission of cosmic rays.

In this work the nature of the radio emission of horizontal air showers is studied in detail. The feasibility of detecting these showers with radio detectors spread over several square kilometres for zenith angles larger than 60° is studied.

With the former LOPES [11] experiment it was shown that it is possible to detect horizontal air showers with radio detectors [12]. However, LOPES, the pioneering radio detection experiment at KIT, with less than 0.3 km² was too small to detect horizontal air showers on a large scale. Furthermore KASCADE [13] triggering LOPES and providing reliable energy and direction reconstruction up to zenith angles of 40° [14] made a study of horizontal air showers difficult. Therefore, the full potential of the radio detection of horizontal air showers could not be studied with LOPES.

The second largest experiment for the detection of the highest energy cosmic rays is the Telescope Array [15], which is located in the United States. It is not sensitive to horizontal air showers, because in contrast to the water Cherenkov tanks at the Pierre Auger Observatory it operates with scintillators, which are sensitive to zenith angles up to 45° [16] only. The photomultipliers of the Tunka-133 [17] experiment are sensitive up to 50° zenith angles [18]. Hence, at the Tunka-133 experiment it is not possible to detect horizontal air showers. Therefore all these detector sites except the Pierre Auger Observatory are not suitable for the detection of horizontal air showers.

The future GRAND [19] experiment will aim at detecting horizontal air showers initiated by primary high-energy neutrinos, interacting in the mountains surrounding the planned array with around 1,000,000 radio stations spread over 200,000 km². The sensitivity of the designed GRAND detector will ensure the detection of cosmogenic neutrinos considering the common source models. The results of this work provide insights for the large-scale radio detection of horizontal air showers and future applications like the search for horizontal air showers initiated by high-energy neutrino primaries.

AERA operating as a part of a hybrid detector of the Pierre Auger Observatory currently provides the best conditions to detect the radiation emitted in the MHz range by horizontal air showers with zenith angles above 60° . In this work cosmic rays and extensive air showers are introduced in chapter 2. The performed preparatory studies of the radio detection of horizontal air showers can be found in chapter 5. The reconstructed data sample and the selection of the data sample are described in chapter 6. The analysis of horizontal air showers is discussed in chapter 7 and the physics analyses performed with horizontal air showers is shown in chapter 8. The conclusion is the content of chapter 9. The preparatory studies of this work were published in [20].

2. Cosmic Rays and Extensive Air Showers

The framework describing the phenomena analysed in this work is described in this chapter. The phenomenology of cosmic rays is described in section 2.1, the development of extensive air showers in section 2.2, the theory of the radio emission of extensive air showers and current radio experiments in section 2.3, the particle showers and the radio emission of horizontal air showers in section 2.4 and the possible detection of high-energy neutrinos in section 2.5.

2.1. Cosmic Rays

Cosmic rays are radiation of particles from outer space. They can be divided into charged cosmic rays and neutral cosmic rays. Charged cosmic rays consist of charged particles (fully ionised atoms) and neutral cosmic rays consist of neutrons, neutrinos or photons. Cosmic ray particles interact in the Earth's atmosphere and produce secondary particles, called secondary cosmic rays. Apart from the particle type, cosmic rays can be characterised by their energy.

2.1.1. Cosmic Ray Flux

The flux of cosmic rays is the number of primary particles per energy bin divided by the detector area, the measurement period and the spatial angle. The course of the cosmic ray flux can be seen in figure 2.1 for a compilation of cosmic ray spectra of the all particle spectra, the proton spectra, the antiproton spectra, the electron spectra, the positron spectra, the neutrino spectra and photon spectra determined by the experiments listed in the legend. The cosmic ray spectra of the highest energy cosmic rays shown in figure 2.2 are scaled with the energy to the power of 2.5. This scaling reveals the features of the knee and the ankle of the cosmic ray spectrum. The power-law

$$N(E) \propto E^{-\gamma} \tag{2.1}$$

describes the flux of cosmic rays. N is the number of particles with energy E . The index γ changes from 2.7 to 3.1 at about 4×10^{15} eV, which is called the knee region and at about 4×10^{18} eV the spectrum flattens again [21]. This is called the ankle

2. Cosmic Rays and Extensive Air Showers

region. The region between the knee and the ankle is interpreted as the transition region from galactic to extragalactic origin of cosmic rays. The composition of sources of the cosmic rays changes in this region and therefore also the flux of cosmic rays. At energies larger than 10^{20} eV a sharp cut-off can be seen. The Pierre Auger Observatory was built to study cosmic rays of ultra-high energy and the steep flux suppression of the highest energy cosmic rays.

The flux of cosmic rays of about 10 MeV to 10 TeV is suited to perform direct measurements, because the flux is high enough for reasonable detector area or measurement time. The direct detection of cosmic rays is realised with satellite or balloon experiments. For energies larger 10 TeV the lower flux leads to the preference of ground based detectors measuring the secondary particles generated in the air shower experiment.

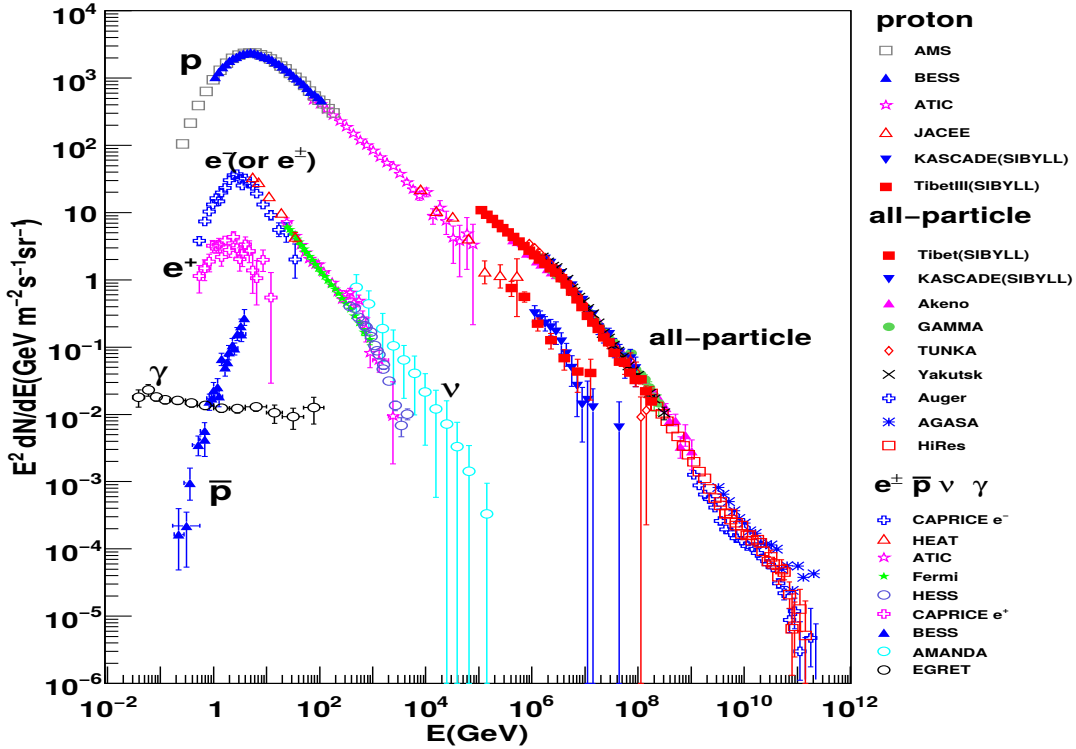


Figure 2.1.: Compilation of measured cosmic ray spectra [22]. The spectra determined by the experiments listed shows the all-particle spectra, the proton spectra, the antiproton spectra, the electron spectra, the positron spectra, the neutrino spectra and photon spectra.

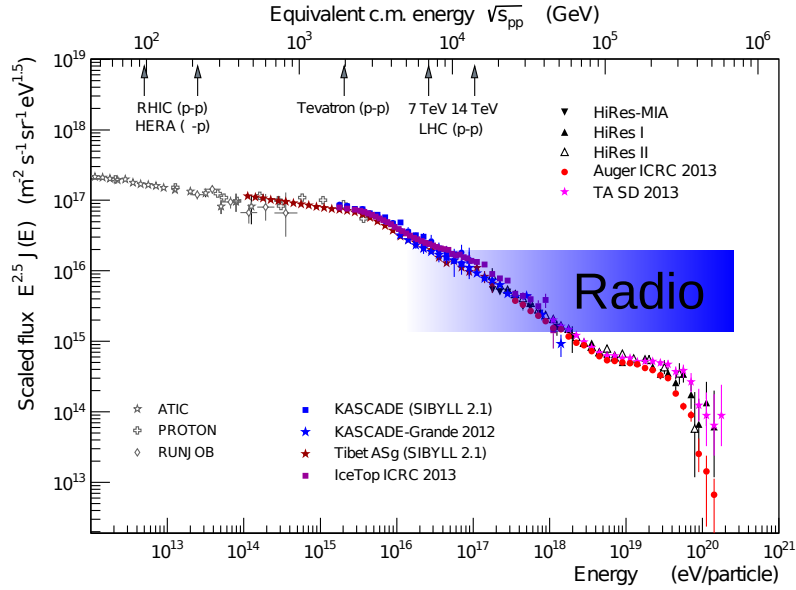


Figure 2.2.: Scaled flux of cosmic rays of the highest energies. The figure is adapted from [23] with respect to the compilation shown in reference [24]. The blue band marks the energy range the radio detection is sensitive to.

2.1.2. Composition

The determination of the composition of cosmic rays can answer the question about the origin of the cosmic ray. As can be seen in figure 2.1 the composition of primary particles is resolved better in direct measurements. In indirect measurements the mass of the primary particle has to be estimated from the detection of the secondary particles. The measured events have to be simulated with Monte Carlo codes (see section 4.2) to study the detector response for different primary particles. The fluctuation of the shower arises because the depth of the first interaction and the multiplicity is essential on the longitudinal and lateral development of the shower [25]. The recent measurements of the Pierre Auger Observatory (see figure 2.3) indicate a tendency of a composition change from lighter to heavier composition at the highest energies. This was determined by measuring X_{\max} , the depth of shower maximum (see section 3.2). Above 10^{17} eV the AERA experiment is also sensitive.

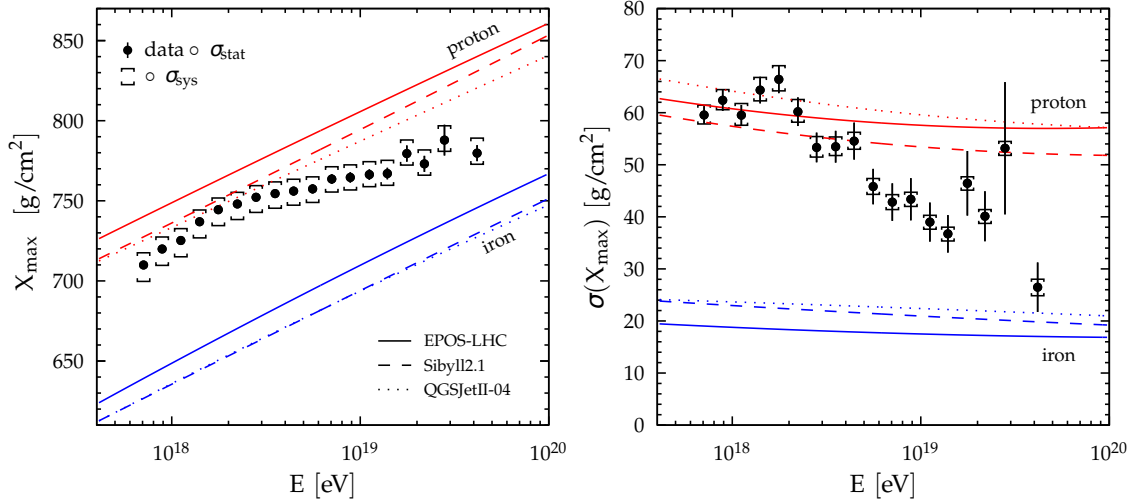


Figure 2.3.: Composition determination at the Pierre Auger Observatory for the highest energies [9]. On the left X_{\max} over primary energy and on the right the width of X_{\max} over energy is shown. The X_{\max} values determined by the measurement is compared to simulated events with proton and iron primaries using high-energy hadronic interaction models EPOS-LHC, Sibyll2.1 and QGSJetII.4.

2.2. Extensive Air Showers

Extensive air showers are defined as the cascade of ionised particles and electromagnetic radiation produced after the interaction of the primary particle in the Earth's atmosphere. The schematic view of an extensive air shower developing in the atmosphere can be seen in figure 2.4. A primary particle interacts with an air molecule through a nuclear interaction and produces secondary particles. These particles can be grouped into three components, the muonic component (seen on the left of figure 2.4), a hadronic components (seen in the middle of figure 2.4) and an electromagnetic component (seen on the right of figure 2.4). The muonic component consists of muons, the hadronic component consists of nuclear fragments, protons, neutrons, neutral and charged pions and kaons and the electromagnetic component consists of electrons, positrons and photons. The electromagnetic component produces the radio emission this thesis is about.

The lateral and longitudinal shower profile of the components of the extensive air showers can be seen in figure 2.5. The longitudinal shower profile can be measured by detecting the Cherenkov light or Fluorescence light. The bulk of particles can be measured and the amount of produced particles differs for the shower components. The lateral distribution can be measured by particle detectors on ground. A small fraction of produced particles is reaching the ground, which is dependent on the X_{\max} . The amount of particles of the lateral distribution differs for the

shower components. The shower profiles differ for different primaries, too and can be distinguished according to their profile.

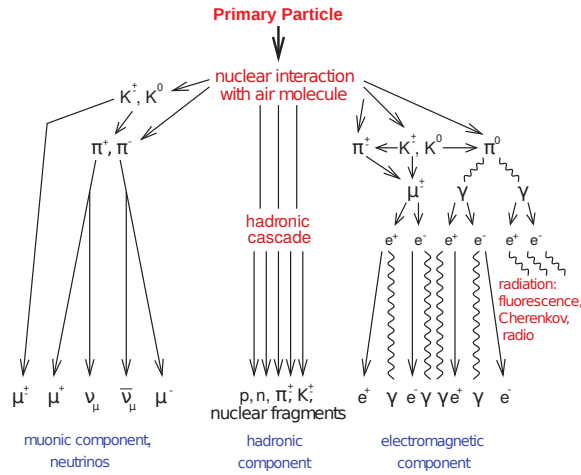


Figure 2.4.: Schematic view of an extensive air shower developing in the atmosphere, adapted from [26]. The muonic component is drawn on the left, the hadronic component is drawn in the middle and the electromagnetic component is drawn on the right.

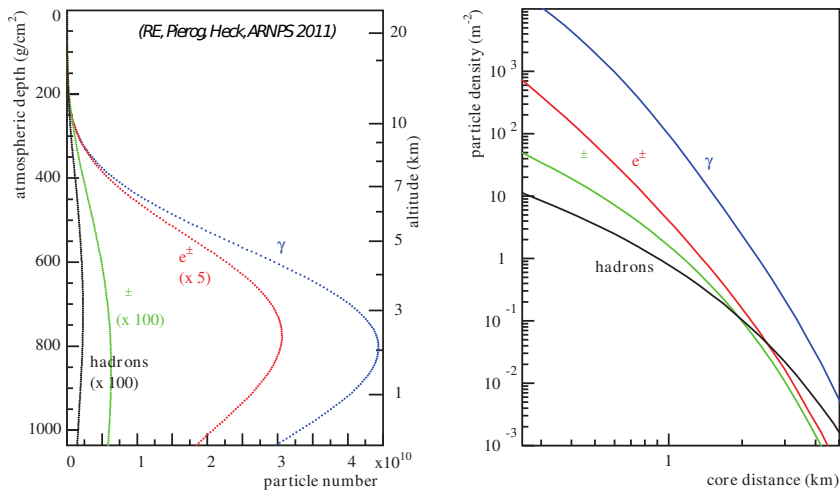


Figure 2.5.: Longitudinal shower profile on the left is the atmospheric depth over the particle number and lateral shower profiles on the right is the particle density over the core distance. Drawn are components of the air shower, adapted from [27].

2.3. Radio Emission of Extensive Air Showers

The first radio detection of extensive air showers was realised in 1965 [23]. The second-generation experiments started with LOPES and CODALEMA [28] in 2003 due to the available digital signal processing techniques. The mechanisms underlying the radio emission of extensive air showers is described in section 2.3.1 and can be detected with radio experiments, some are described in section 2.3.2.

2.3.1. Mechanism

Due to the Lorentz force charged particles get deflected in the Earth's magnetic field. During this deflection the particles emit coherent radiation with wavelengths smaller than the thickness of the particle shower. This radio frequencies are ≤ 100 MHz and therefore inside the frequency range common radio experiments operate. The geomagnetic effect (left sketch of figure 2.6) is the main source of the radio emission of extensive air shower. It is a time varying transverse current with linear polarisation across the $\vec{v} \times \vec{B}$ direction of the Lorentz force. The secondary mechanism of radio emission is the charge effect (right sketch of figure 2.6). This effect occurs because the positrons produced during the shower development annihilate and the remaining electrons travel with the shower front and meanwhile emit radiation. This is a time varying net charge excess and it is linearly polarised with the electric field vector. Thanks to the different polarisations, the fraction of the strength of the two mechanisms of the radio emission could be studied at the AERA site. It results in approximately 90% contribution of the geomagnetic and approximately 10% contribution of the charge excess to the radio emission [29]. The strength of the radio emission also depends on the geomagnetic angle [30]. The geomagnetic angle is the angle between the shower direction and the local magnetic field. The amplitude of the radio signal is measured in $\mu\text{V}/\text{m}/\text{MHz}$.

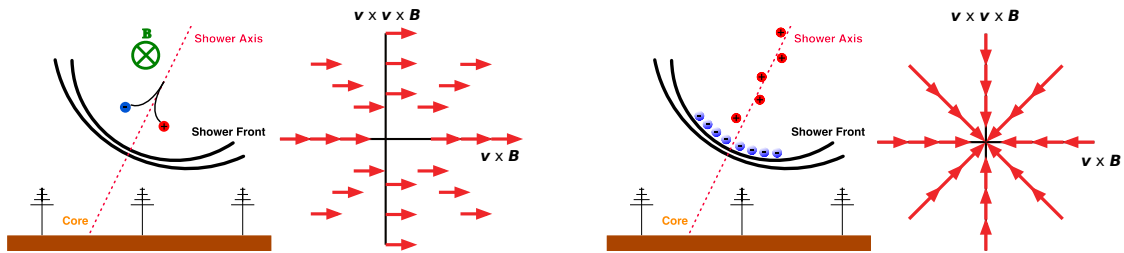


Figure 2.6.: Geomagnetic effect (left figure) and charge excess mechanism (right figure) [23].

2.3.2. Experiments

Some ground based radio experiments of the past, present and future are sketched in figure 2.7.

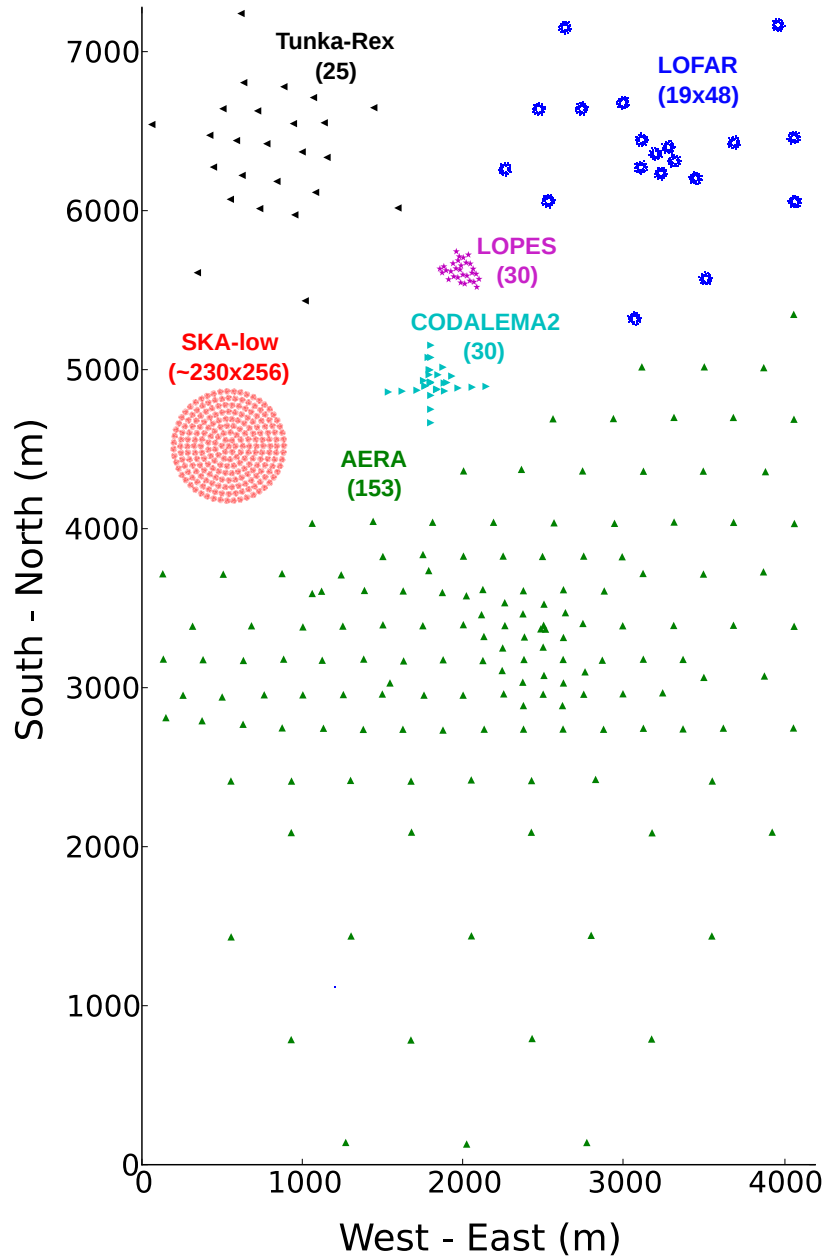


Figure 2.7.: Compilation of several radio experiments shown in the same scale [31].

AERA

The Auger Engineering Radio Array (AERA) is an enhancement of the Pierre Auger Observatory and is located in Malargüe, Argentina. The setup is described in section 3.4. In its final phase AERA consists of 153 radio stations covering an area of 17 km². In AERA self-triggered stations triggered by scintillators and externally triggered stations triggered by the surface tanks and the fluorescence telescopes are combined in one experiment. The AERA stations operate in the frequency range of 30 to 80 MHz. Greatest achievements until now are the results on the polarisation measurements [29], the energy determination of cosmic rays with AERA [32] and the nanosecond-level time synchronization [33]. AERA is currently the largest radio detector world-wide for measuring air showers.

CODALEMA

The COsmic ray DEtection Array with Logarithmic ElectroMagnetic Antennas (CODALEMA) is located at the Nançay radio observatory in France. CODALEMA consists of 30 radio station triggered by scintillators. The frequency range is 24 to 82 MHz. One result of CODALEMA was the determination of the charge excess contribution to the total radio emission in air showers [34].

LOFAR

The LOw Frequency ARray (LOFAR) [35] is a digital radio interferometer with antennas distributed over several European countries with a dense core located in the Netherlands. It consist of low-frequency antennas operating from 20 to 80 MHz and high-frequency antennas operating from 110 to 240 MHz. It was built to perform radio astronomy. With the particle array LORA (LOfar Radboud Air shower array) triggering LOFAR at the central LOFAR station, it is possible to detect cosmic ray showers. The dense packing of the inner core of LOFAR makes it possible to study the lateral distribution function of the radio emission in great detail [36]. The LOFAR composition measurements estimated a light mass contribution in the energy range of 10^{17} to $10^{17.5}$ eV [37].

LOPES

The LOfar PrototypE Station (LOPES) was located in Karlsruhe, Germany. It was triggered by the particle detector KASCADE and operated from 2003 to 2013. The frequency range of LOPES was 40 to 80 MHz and up to 30 antenna stations were operating at once. It was the first experiment which showed the proof-of-principle of digital radio interferometry [38]. The direct measurement of the horizontal component of the electric field vector was first performed with LOPES-3D stations [39].

SKA

The future Square Kilometre Array (SKA) will be the world's largest radio telescope. It will be located in Australia and South Africa and will probably start measurements in 2023. The frequency range of the low-frequency antennas to be installed in Australia will be 50 to 350 MHz. Together with a particle array, SKA will perform tomography of the radio emission with a dense array of about 60,000 antenna stations spread over 1 km².

TREND

The TIANSHAN Radio Experiment for Neutrino Detection (TREND) [40] is located in XinJiang, China. TREND consists of 80 self-triggered antennas. The science goal is the detection of horizontal air showers induced by tau neutrinos interacting in close-by mountains. First extensive air showers are detected with TREND.

Tunka-Rex

The Radio extension of the Tunka Cherenkov array (Tunka-Rex) is located in Siberia, Russia. It consists of 44 antenna stations covering an area of about 1 km². Recent results are the energy determination by the cross calibration with the Cherenkov detectors and a first X_{max} determination [41].

GRAND

The future Giant Radio Array for Neutrino Detection (GRAND) [42] will search for extensive air showers initiated by cosmogenic neutrinos interacting in the mountains surrounding the planned array. In order to achieve this, 1,000,000 radio detectors spread over 200,000 km² [43] will be installed. This will make it possible to perform neutrino astronomy with radio detectors.

2.4. Horizontal Air Showers

Horizontal air showers (HAS) are air-shower which come close to the horizon. The height of the first interaction of the primary particle is unchanged for horizontal air shower but they travel more atmosphere then vertical showers (see figure 2.8). The shower has more time to develop and will look older, i.e. the number of particles arriving at ground will be smaller and dominated by muons [44]. For an older shower the X_{max} is farer away from the ground than for a young shower. Horizontal air showers are more difficult to model, because the curvature and the geomagnetic field of the Earth cannot be neglected for horizontal air showers [45].

The correlation of the energy estimator R_μ of the surface detector and the energy determined by FD of horizontal air showers detected at the Pierre Auger Observatory can be seen in figure 2.9. Requiring full efficiency and applying quality cuts of the reconstruction of horizontal air showers lead in ten years of Auger data to 174 high-quality hybrid events [46]. The energy calibration of the surface detector with the fluorescence detector allows to determine a cosmic ray spectrum above 4×10^{18} eV for events with zenith angle larger than 60° [47]. The cosmic ray spectrum of horizontal events confirms a flux suppression at the highest energies.

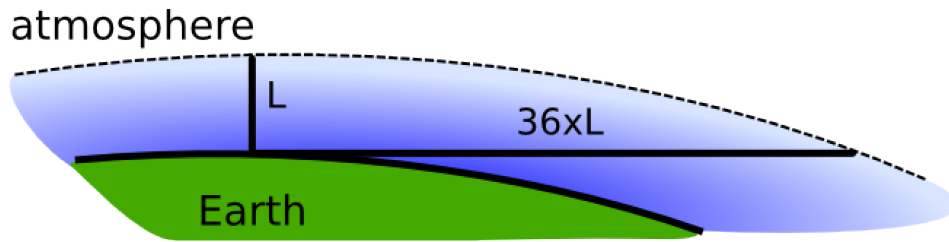


Figure 2.8.: Horizontal air showers travel up to 36 times the atmosphere than vertical shower. [48]

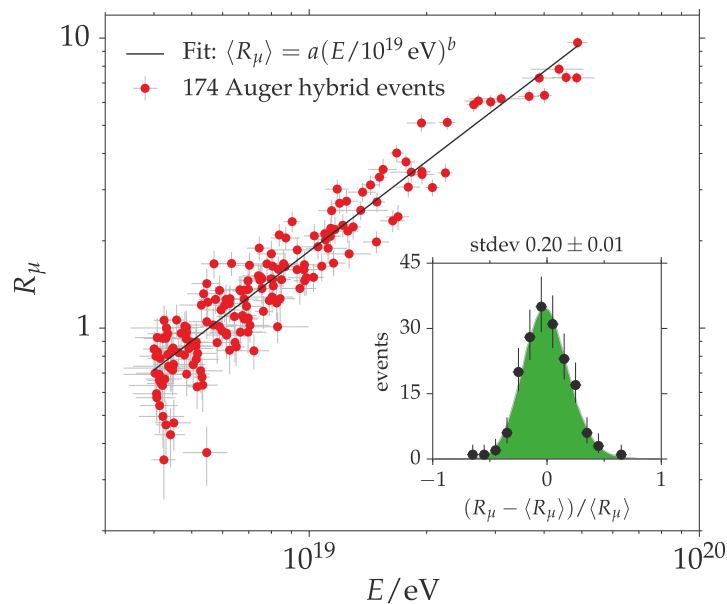


Figure 2.9.: The calibration of the energy estimator R_μ of the surface detector with the energy determined by the fluorescence detector of horizontal air shower at the Pierre Auger Observatory, adapted from [49].

2.4.1. Radio Detection of Horizontal Air Showers

The radio detection of horizontal air showers has some advantages compared to the detection of the particle shower. The radio signal is not absorbed in the atmosphere and therefore the radio signal can still be detected if the early part of the shower, the electromagnetic and hadronic component is absorbed. This is illustrated in figure 2.10. The footprint of the shower on ground is large, because the distance to the source is larger if a shower has to travel more atmosphere. During the overall development of the shower radiation is emitted. Additionally, there is a projection effect resulting in an elliptical shape of the footprint. The footprint of a 10^{18} eV proton shower for different inclinations is shown in figure 2.11. This predicts a footprint of several square kilometres for horizontal air showers of this energy. Considering the surface plot (see figure 2.12) the detection of horizontal air showers with an antenna grid of 750 m should be possible.

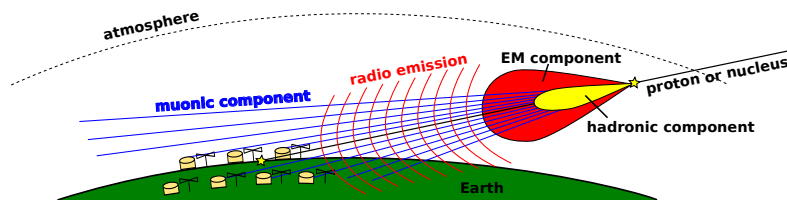


Figure 2.10.: Illustration of a horizontal shower [50]. The hadronic and electromagnetic component is absorbed and the muonic component and the radio signal can be measured on the ground.

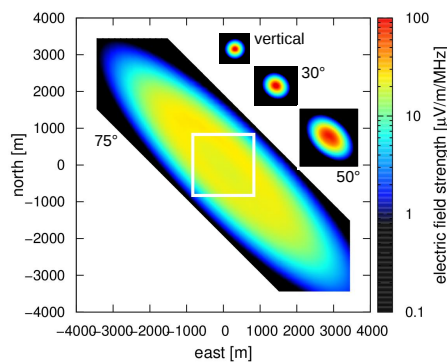


Figure 2.11.: Field strength over position of CoREAS simulations for primary proton showers of 10^{18} eV for different zenith angles, adapted from [51, 23]. The white box marks the change of antennas distance from 40 m to 100 m in the simulation to save computing time [52].

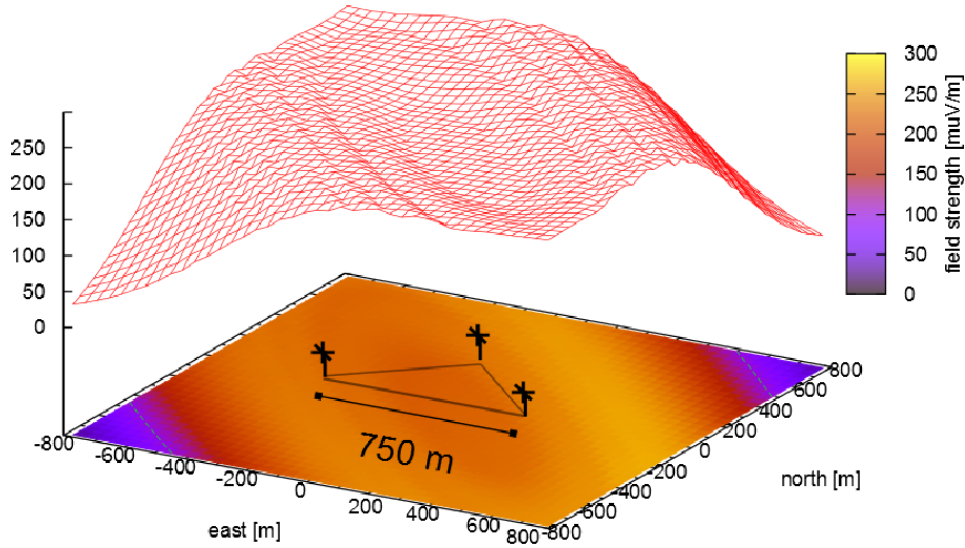


Figure 2.12.: Field strength over position of a CoREAS simulation of a proton primary with 1 EeV energy and 75° zenith angle, adapted from [52]. In addition three stations with a distance of 750 m between the stations are drawn.

2.5. Neutrino Detection

The detection principle of neutrino-induced horizontal air showers with surface detectors is the detection of a young horizontal air shower with electromagnetic, hadronic and muonic component on ground (see right sketch of the upper part of figure 2.13). For young cosmic ray showers the X_{\max} is close to the ground. The secondary particles of horizontal air showers with hadronic primaries are absorbed during the shower development (see left sketch of upper part of figure 2.13). The detection of neutrinos at the Pierre Auger Observatory would work like sketched on the lower part of figure 2.13. A horizontal neutrino-induced shower could interact deep in the atmosphere, and produce a tau which interacts close to the detector, e.g. in surrounding mountains or up-going in the Earth and can then be detected by the surface detector. No neutrino candidate was found in ten years of Auger data [53]. This provides the current limit on the diffuse flux of ultra-high energy neutrinos with an E^{-2} spectrum in the energy range 1.0×10^{17} eV - 2.5×10^{19} eV of $E_\nu^2 dN_\nu/dE_\nu \leq 6.4 \times 10^{-9}$ GeV cm $^{-2}$ s $^{-1}$ sr $^{-1}$ [54]. The latest limits on the neutrino flux can be seen in figure 2.14 for Auger, IceCube and ANITA-II, with the current predictions on the neutrino flux from cosmogenic neutrino models. IceCube is a particle detector at the South Pole that detects neutrinos interacting in the Antarctic ice and the Antarctic Impulsive Transient Antenna (ANITA) is a balloon experiment using an array of radio antennas to detect radio pulses emitted by the interactions of neutrinos with the Antarctic ice sheet.

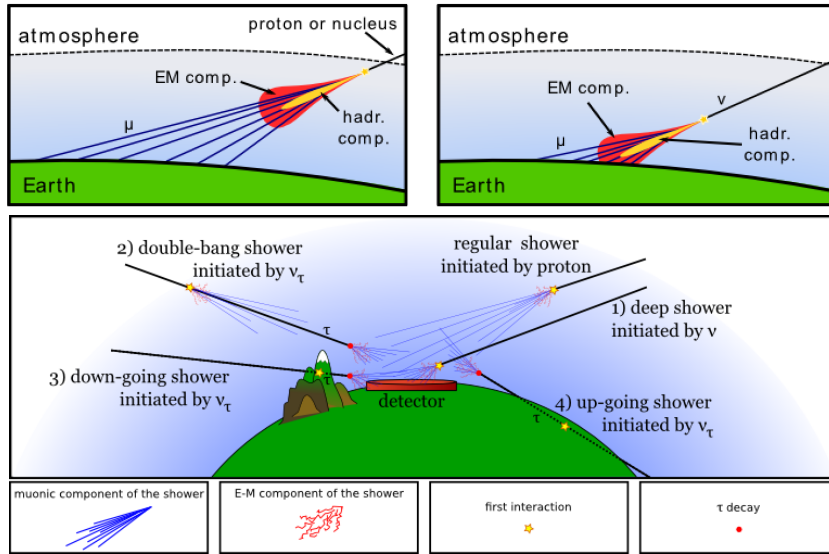


Figure 2.13.: The detection of a horizontal air shower initiated by a proton or a nucleus on the left and by a neutrino on the right of the upper part. The lower part shows the detection principles of neutrino-induced showers at the Pierre Auger Observatory [48].

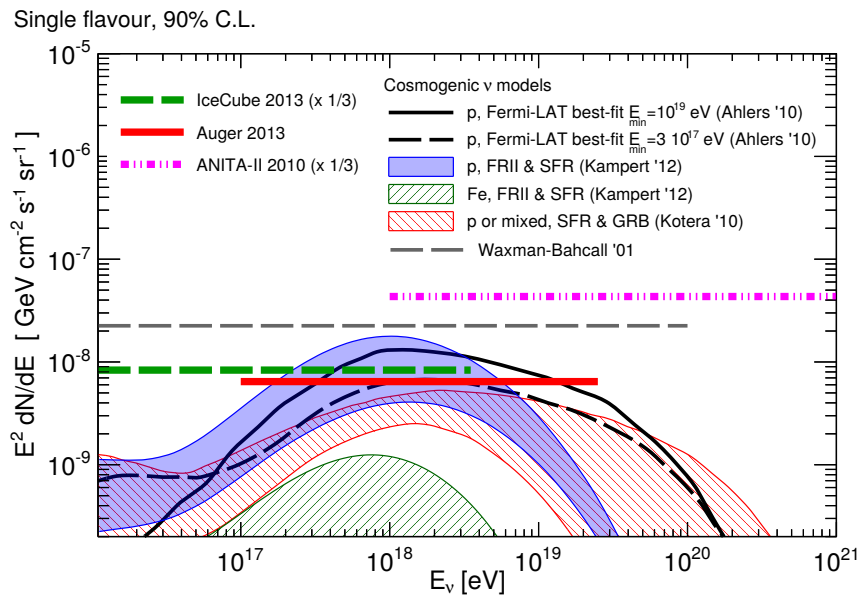


Figure 2.14.: Limits on neutrino flux obtained from the Pierre Auger Observatory, IceCube and ANITA-II with current predictions on the neutrino flux from cosmogenic neutrino models. [9].

3. The Pierre Auger Observatory and AERA

The analyses in this work are based on data collected at the Pierre Auger Observatory [8] located in Malargüe, Argentina. The Pierre Auger Observatory was built to detect extensive air showers in a hybrid detector mode and takes data since 1998. It is the world's largest cosmic ray observatory. It consists of 1660 water Cherenkov particle detector stations spread over 3000 km^2 (see section 3.1) and 24 air fluorescence telescopes (see section 3.2). AERA (see section 3.4), HEAT [55] and AMIGA (see section 3.3) are enhancements to the Pierre Auger Observatory. In figure 3.1 one surface detector (SD) and one AERA station can be seen in the foreground and one fluorescence detector (FD) building and the HEAT telescopes in the background.



Figure 3.1.: Picture of one surface detector and one AERA station in the front, one of the four fluorescence detector buildings and the three HEAT telescopes in the back [56].

3.1. Surface Detector

The Surface Detector (SD) consists of 1660 water Cherenkov particle detectors deployed on a grid size of 1500 m [57]. One example event can be seen in figure 3.2 with the shower observable S_{1000} of the lateral distribution function of the particle detector showing also the principles of shower reconstruction. The S_{1000} observable is the value of the lateral distribution function at the reference distance of 1000 m from the SD shower axis measured in vertical equivalent muons (VEM), the signal a muon traversing the SD tank vertically deposits in the tank. The S_{1000} observable is proportional to the energy of the primary particle initiating the cosmic ray shower. The SD array is fully efficient from 3×10^{18} eV onwards for vertical showers of zenith angles smaller than 60° and from 4×10^{18} eV onwards for horizontal air showers in the zenith angle range from 62° to 80° [58]. The zenith angle range from 60° to 62° is not studied.

The design drawing of one SD tank can be seen in figure 3.3. The SD tank is filled with 12 tons of highly purified water which is overseen by three photomultipliers. Charged particles passing the tank with a speed faster than the phase velocity of light in water emit Cherenkov radiation. A low energy extension of SD is the SD Infill array. The SD Infill array consists of 61 SD tanks deployed on a grid size of 750 m. The SD Infill is fully efficient from 3×10^{17} eV onwards for air showers with zenith angles $> 55^\circ$ [58]. This makes the SD Infill sensitive to the transition region of the cosmic ray spectrum, the region between the second knee and the ankle. The duty cycle, the fraction of data-taking of SD is nearby 100%. Individual SD tanks can drop out of the data acquisition, but the SD array will still detect events.

3.2. Fluorescence Detector

The Fluorescence Detector (FD) consists of 24 air fluorescence telescopes detecting ultraviolet light emitted by excited atmospheric nitrogen [60]. With FD the track of the nitrogen fluorescence in air showers can be detected. One example event can be seen in figure 3.4. The four fans represent the four FD sites collecting the emitted fluorescence light. The maximum of the longitudinal profile is called X_{\max} , the depth of the shower maximum. X_{\max} is sensitive to the composition of the primary particle as can be seen on the right plots of figure 3.4.

The design drawing of one FD site can be seen on the left of figure 3.5. The FD camera consists of 440 photomultipliers, which can be seen on the right of figure 3.5. The fluorescence light passes the shutter and is reflected on segmented mirrors towards the camera. The resolution of the X_{\max} determination is better than 20 g/cm^2 [8] for events detected with SD and FD and the duty cycle, the fraction of data-taking time of FD is about 13 % [60] due to the requirement of measuring during moonless nights.

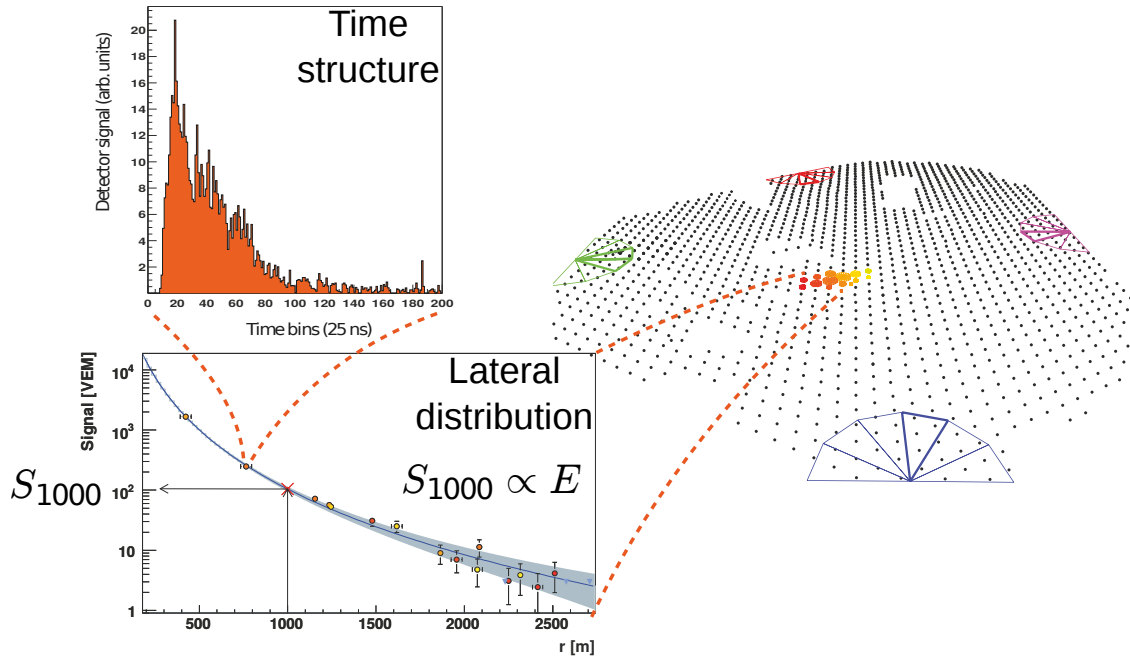


Figure 3.2.: One example event detected by the surface detectors of the Auger Observatory with the shower observable S_{1000} , adapted from [49]. Each circle represents an SD tank. The coloured tanks in the middle of the array are triggered by the air shower. The color scheme represents the timing and the size of the marker the signal height. The triggered tanks are drawn in the lateral distribution function. The LDF is fitted and the S_{1000} , the signal in VEM at 1000 m distance from the shower axis, is determined.

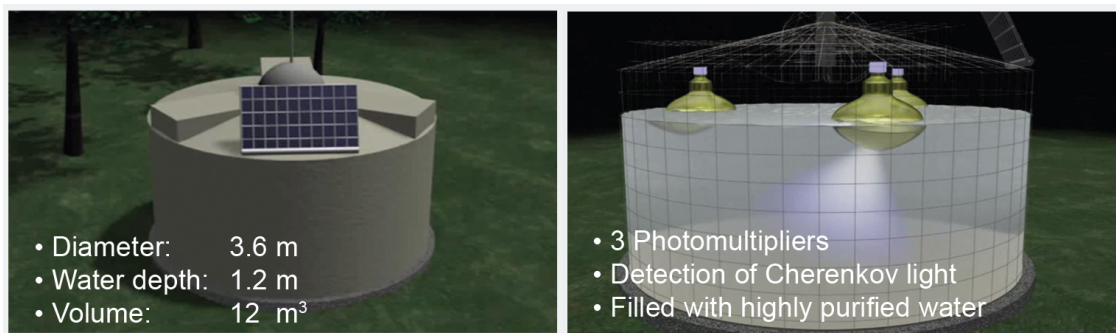


Figure 3.3.: Design drawing of an SD tank, adapted from [59].

3. The Pierre Auger Observatory and AERA

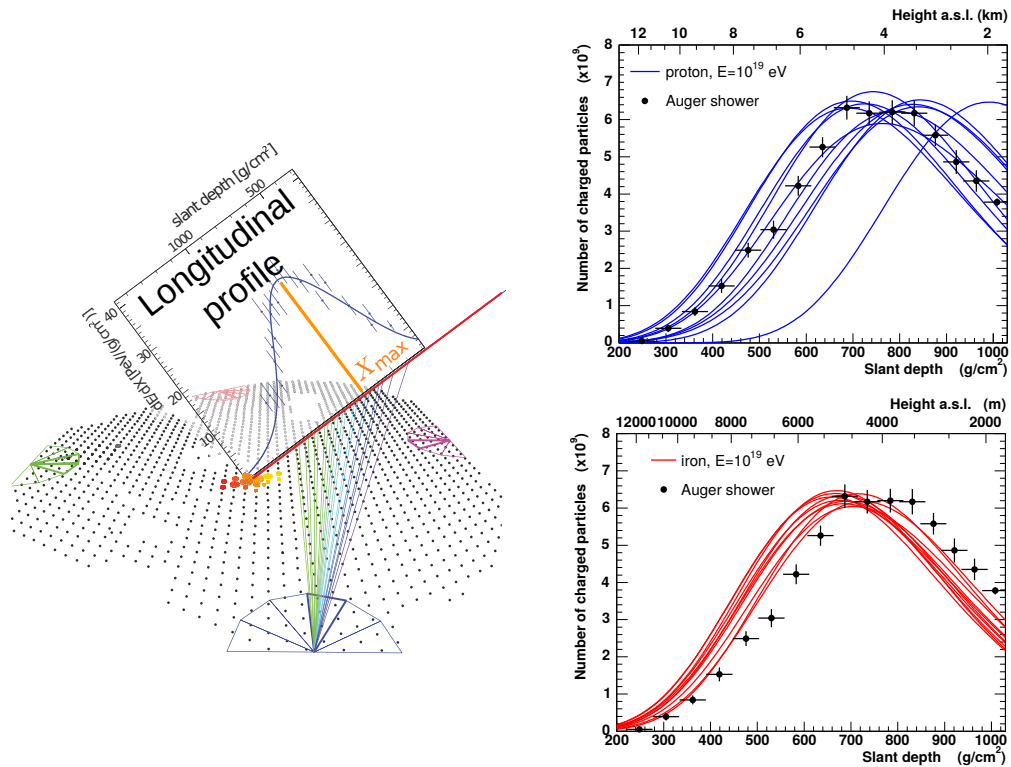


Figure 3.4.: One example event detected by the fluorescence detector of the Pierre Auger Observatory with the shower observables X_{max} , adapted from [49]. The four fans represent the FD sites. The longitudinal shower development can be reconstructed by the emitted fluorescence light trail. X_{max} is the depth of the shower maximum, the maximum of the longitudinal profile. X_{max} is sensitive to the primary mass as can be seen on the left plots. Longitudinal profiles of simulated events with proton and iron primaries differ in their X_{max} values.

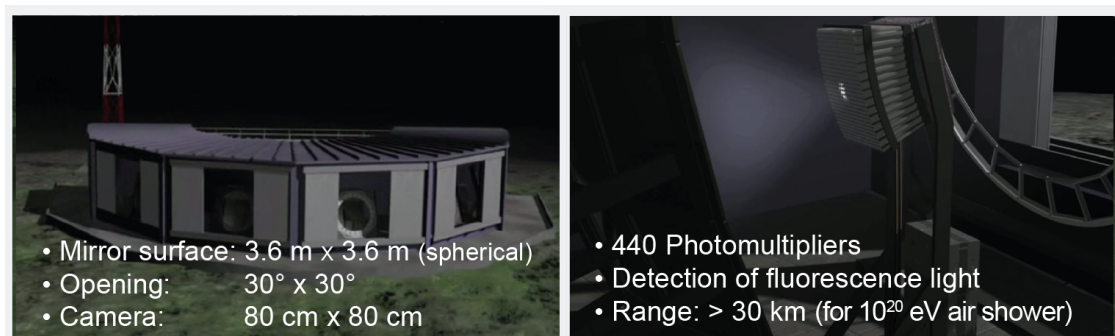


Figure 3.5.: Design drawing of an FD telescope building on the left and the FD camera on the right, adapted from [61].

3.3. Auger Muons and Infill for the Ground Array

The Auger Muons and Infill for the Ground Array (AMIGA) is an enhancement to the Pierre Auger Observatory and located at the SD Infill [62]. AMIGA consists of underground muon counters. Each muon counter consists of 64 plastic scintillator strips buried 2.3 m underground next to an SD tank. The depth is necessary to shield from electrons and to measure only the muonic component of the air shower. The design drawing of an AMIGA muon counter can be seen in figure 3.6. The completed AMIGA detector will consist of 61 muon counters and cover an area of 25 km². The AMIGA engineering array called Unitary Cell consists of seven muon counter. The Unitary Cell is arranged in a hexagonal structure and is taking data since 2013 [63].

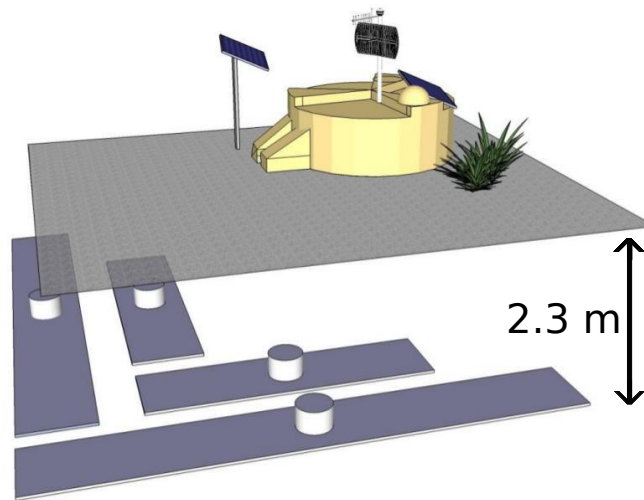


Figure 3.6.: Design drawing of the AMIGA muon counter [64].

3.4. AERA - The Auger Engineering Radio Array

AERA, the Auger Engineering Radio Array, is located at the SD Infill [10]. It measures the radio emission of extensive air showers in the 30-80 MHz frequency range. It was designed to explore the radio emission of extensive air showers above an energy threshold of 10^{17} eV in a hybrid detection mode. AERA can measure events detected by SD, FD and AMIGA as well as self-triggered events.

AERA is an engineering array and was deployed in the phases AERA-24, AERA-124 and AERA-153 with different antenna types. A map of AERA can be found in figure 3.7. The antenna types used in AERA are the log-periodic dipole antenna (LPDA) and the Butterfly antenna. The picture of one LPDA station can be

3. The Pierre Auger Observatory and AERA

found on the left of figure 3.8 and the picture of one Butterfly station can be found on the right of figure 3.8. The LPDA assembles a series of half wave dipoles of increasing length to keep the radiation resistance of the LPDA constant over a wide frequency range [10]. The dimension of the LPDA is about $4 \times 4 \times 3.5 \text{ m}^3$. The Butterfly antenna is an active bowtie antenna, the successor of the active short dipole antenna [10]. The potential of the Butterfly antenna of detecting cosmic rays was tested in the CODALEMA experiment before [65]. The dimension of the Butterfly is about $2 \times 2 \times 1 \text{ m}^3$.

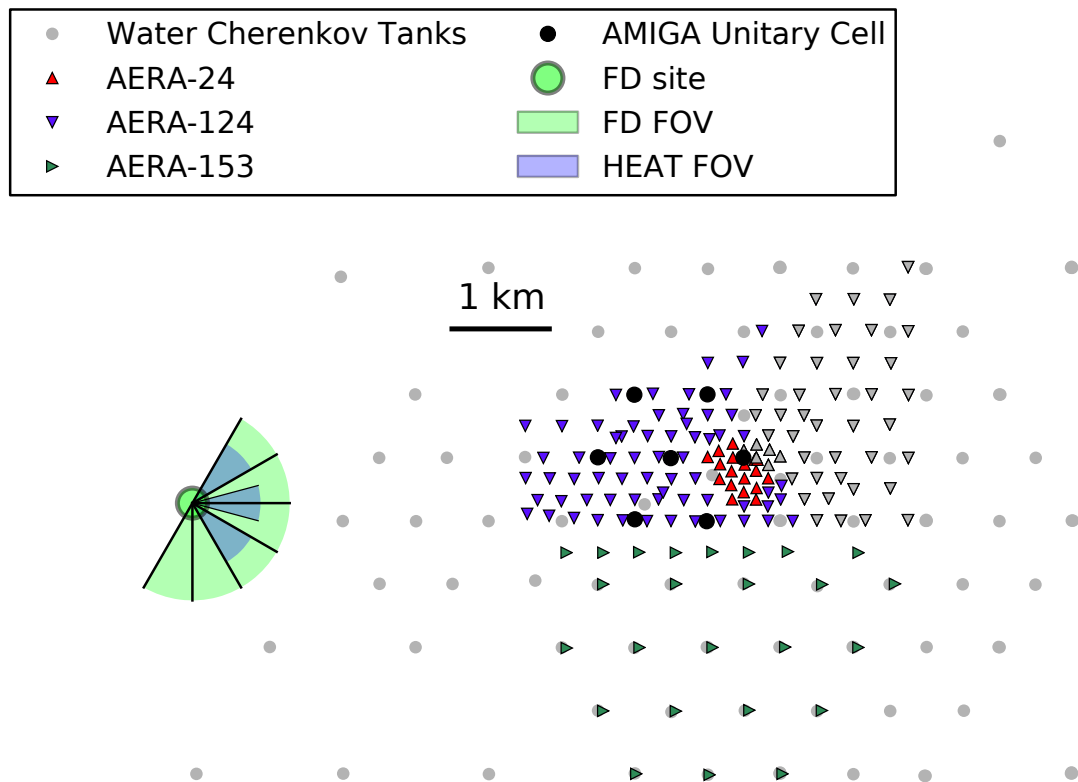


Figure 3.7.: Map of AERA with the AERA phases AERA-24, AERA-124 and AERA-153, adapted from [67]. In red triangles the AERA phase AERA-24, in blue triangles AERA-124 and in green triangles AERA-153 are marked. The light blue triangles are the self-triggered stations of AERA-24 and AERA-124. The SD tanks are marked with grey circles and the field of view of FD and HEAT at the Coihueco site are marked by fans. The AMIGA Unitary Cell is marked by black circles.



Figure 3.8.: Picture of one LPDA station on the left and picture of one Butterfly station on the right [68].

The frequency range of both antennas is 30 to 80 MHz and they have a north-south and east-west polarisation. Each polarisation holds two channels, a low-gain and a high-gain channel. The antenna stations consist of the physics antenna itself, attached to a pole with an aluminium box hosting the electronics, a solar cell and a battery for the power supply. At the pole also a GPS antenna for time adjustments of the antenna stations and for the Butterfly station a Wi-Fi antenna for the data transfer are attached. The antenna stations are surrounded by a fence in order to protect the station from environmental influences.

The detected signal is preprocessed at the antenna station. The LDPA stations transmit their recorded data by cable to the the Central Radio Station (CRS) and there the data is transmitted further to the Data Acquisition (DAQ) system. The Butterfly stations transmit their recorded data directly to the DAQ system. The DAQ system is located at the Coihueco FD building.

AERA-24 consists of 24 LDPA stations of which 17 are externally triggered by SD and six are self-triggered by scintillators. The radio stations are deployed on a grid size of 144 m. AERA-124 consists of 24 LPDA stations and 100 Butterfly stations of which 57 are externally triggered and 43 are self-triggered with a grid size of 250 m and 375 m. AERA-153 consists of 24 LPDA stations and 125 Butterfly stations with a grid size up to 750 m. The additional 25 Butterfly stations of AERA-153 are externally triggered. Four prototype stations measuring the horizontal components were deployed (see section 5.2.2) and five self-triggered Butterfly stations were attached with Whisk antennas [66]. An overview of the data sample of the three different stages of AERA used in this work can be found in table 3.1. In the final stage AERA covers an area of 17 km².

The electric-field is measured at the radio station. A Hilbert Envelope is applied to the square root of the quadratic sum of the electric field components. The

Phase of AERA	start	stop
AERA-24	01.11.2011	24.06.2013
AERA-124	26.06.2013	01.03.2015
AERA-153	02.03.2015	15.08.2015
Prototype stations	22.11.2013	15.08.2015

Table 3.1.: Overview of the periods for data taking relevant for this work.

Hilbert transform is a tool in signal processing to transform measured signal in an analytic representation. For a sine wave the magnitude of the signal will look like the Hilbert Envelope. This can be seen for one example in figure 3.9. The amplitude is measured in $\mu\text{V}/\text{m}$. The simulated antenna response has to be applied during the reconstruction and introduces an uncertainty depending on the incoming direction [10]. The LPDA stations are absolutely calibrated regarding the analog signal chain of the stations, but the calibration of the Butterfly stations is ongoing. Due to the small sample of detected horizontal air shower events in phase AERA-24 the data of the phases AERA-124 and AERA-153 are also used in this work despite the missing calibration of the Butterfly stations.

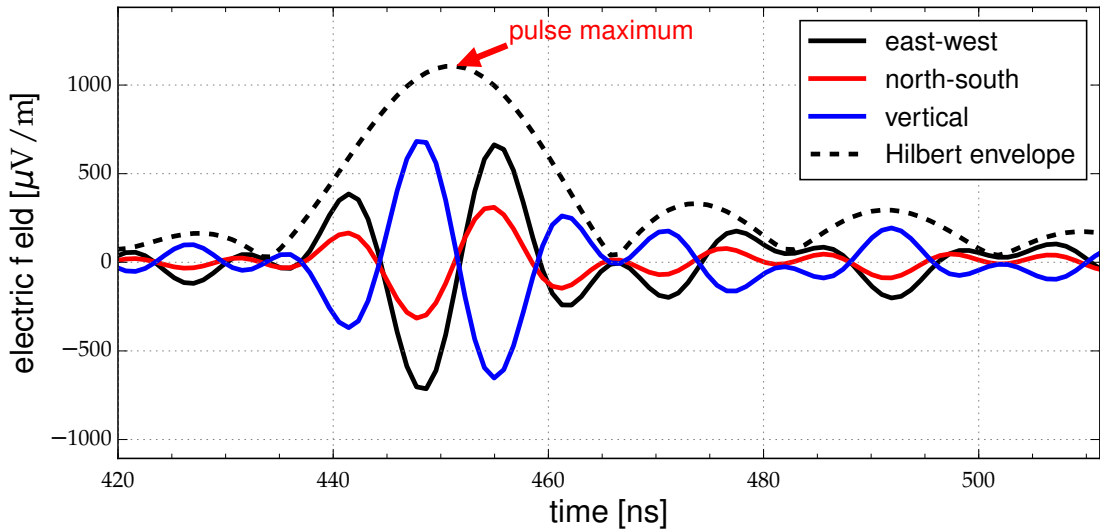


Figure 3.9.: Reconstructed electric-field measured in $\mu\text{V}/\text{m}$ at a radio station. The maximal pulse is determined by applying a Hilbert Envelope to the square root of the quadratic sum of the electric field components [32].

4. Analysis Methods and Tools

The analysis methods and tools used in this work will be described in this chapter. The `Offline` [69] framework described in section 4.1 is the framework used to analyse data detected by the Pierre Auger Observatory. The Monte Carlo simulation codes are described in section 4.2. Used in this work are CORSIKA [70] with FLUKA [71] and QGSJETII4 [72] for the simulation of the particle signal and CoREAS [73] for the simulation of the radio signal emitted by the cosmic rays. The analyses are performed with ROOT [74]. The applied lateral distribution function for radio is described in section 4.3.

4.1. `Offline`

`Offline` is a framework written in C++ using a sequence of analysis modules configurable in Extensible Markup Language (XML) integrating databases containing detector descriptions or measurement conditions. The Auger Package Environment (APE) provides all external dependencies. The reconstruction of data works sequentially. Each module is performed one after the other and the result is written in Advanced Data Summary Tree (ADST) ROOT files. Afterwards the properties of the reconstructed events can be analysed with external code. Originally the framework was written to analyse data of SD and FD. There are special radio modules in `Offline` developed for AERA and described in [75]. “Its functionality has achieved a high degree of sophistication and offers advanced features such as vectorial reconstruction of the electric field, advanced signal processing algorithms, a transparent and efficient handling of FFTs, a very detailed simulation of detector effects, and the read-in of multiple data formats including data from various radio simulation codes“ [75]. The framework is partly published as open source software. For example, the Tunka-Rex collaboration [76] also uses the radio modules of the `Offline` framework to reconstruct their data. The reconstruction steps of AERA data is diagrammed in figure 4.1.

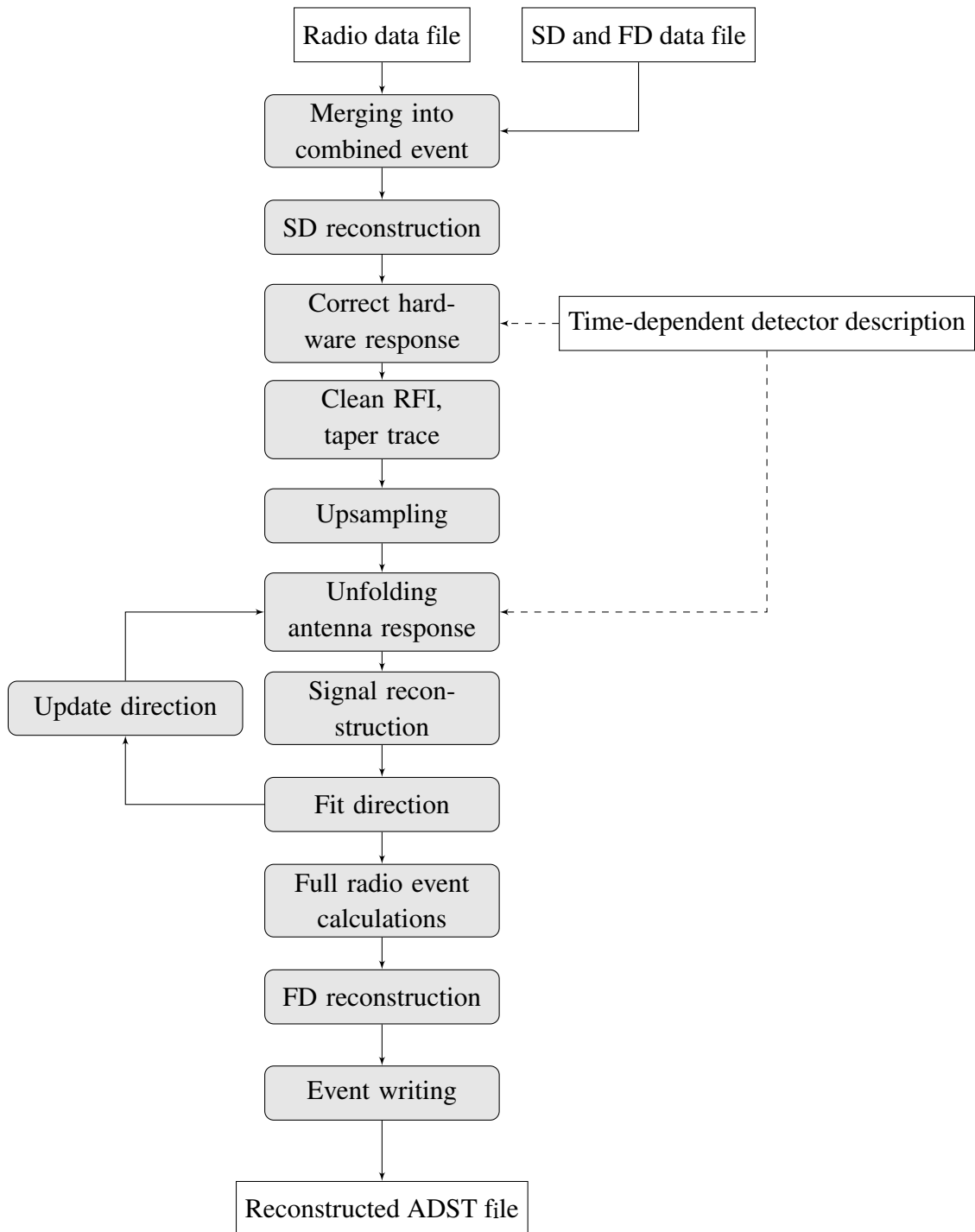


Figure 4.1.: Offline event reconstruction pipeline for AERA data [77].

4.2. Monte Carlo Simulations

The Monte Carlo simulation code used in this work is CORSIKA (COsmic Ray SIMulations for KAscade), the detailed simulation program for extensive air showers initiated by high energy cosmic particles [78]. “CORSIKA is a multi-purpose simulation for 4-d (space & time) particle showers in the atmosphere“ [79]. It handles hadronic interactions, electromagnetic interactions, particle decays and it is tracking the produced particles. The primary particle type, the primary energies, and the direction of the primary particle can be adjusted in a steering file. For this work the low-energy hadronic interaction model FLUKA was chosen and the high-energy hadronic interaction model QGSJetII4 to be able to compare the obtained results to the common simulations generated for AERA.

There are different modern models and Monte Carlo codes available to simulate the radio emission of cosmic rays. A summary can be found in table 4.1.

Simulation Code	Description
MGMR	time-domain, analytic, parametrized shower, fast, free parameters, summing up mechanism
EVA	time-domain, parametrisation of distributions derived from cascade equations or MC
SELFAS2	time-domain, shower from universality, summing up vector potentials for tracks
REAS3.1	time-domain, histogrammed CORSIKA showers, endpoint formalism
ZHAireS	time-and frequency-domain, Aires showers, ZHS formalism
CoREAS	time-domain, CORSIKA showers, endpoint formalism

Table 4.1.: Summary of available simulation codes for simulating the radio emission. From top to bottom the codes are more microscopic [80].

In this work the CoREAS (Corsika-based Radio Emission from Air Showers) simulation code, which is an option in CORSIKA, is used to simulate all measured horizontal events detected by AERA. A detailed simulation study for one AERA-24 event detected in 17 stations showed that the simulation code CoREAS and ZHAireS are in good agreement [81, 82] and can both be used to described events detected by AERA. CoREAS uses the endpoint formalism, which tracks the motion of particles via a series of discrete, instantaneous acceleration events and sums up the emitted radiation [83]. ZHAireS is an AIRES-based Monte Carlo code [84] (not CORSIKA), which tracks each single particle and calculates its contribution to the radio emission and adds it to the total electric field [85]. The SLAC T-510 [86] experiment was a laboratory experiment and confirmed that the simulation codes

CoREAS and ZHaireS can be used to describe the radio emission.

In order to guarantee the model independence all low-energy and high-energy hadronic interaction models of CORSIKA should be tested. This was not possible in the course of this work due to the high computing time required by CoREAS.

4.3. Lateral Distribution Functions

There are three different lateral distribution functions available in `Offline` to describe the lateral distribution of the measured amplitudes of radio stations. They have different complexities to describe the asymmetric footprint of the amplitudes of the radio emission at observation level. The use depends primarily on the number of antennas hit by the individual air shower.

The simple exponential LDF is

$$f_1(x) = a \cdot e^{-b \cdot (x/m-100)}. \quad (4.1)$$

The fit parameters are a and b and the function argument x should be passed in the unit meter. This lateral distribution function is suited to fit the distribution of experiments with sparse antenna arrays or vertical air showers triggering a few antennas only. The simple exponential is used in the LOPES experiment and the Tunka-Rex experiment. The reference values are 100 m for the LOPES experiment and 120 m for the Tunka-Rex experiment. These values were found empirically.

In order to get the extended exponential LDF a Gaussian is added

$$f_2(x) = a \cdot e^{-b \cdot (x/m-100)^2 + c \cdot (x/m-100)}. \quad (4.2)$$

Here the parameters a , b and c are the fit parameters and the function argument x should be passed in the unit meter. One additional antenna is needed to perform the fit compared to the simple exponential. The proposed two-dimensional lateral distribution function by LOFAR [87] is

$$f_3(\vec{r}) = A_+ \cdot e^{-\frac{(\vec{r}-\vec{r}_+)^2}{\sigma_+^2}} - A_- \cdot e^{-\frac{(\vec{r}-\vec{r}_-)^2}{\sigma_-^2}}. \quad (4.3)$$

$f_3(\vec{r})$ is the subtraction of two Gaussian functions. The fit parameters are the amplitudes A_+ , A_- , σ_+ , σ_- and the reference points \vec{r}_+ and \vec{r}_- . In the RdObserver (see section 6.1) and the RdHASObserver (see section 6.2), the standard analyses of AERA and in this work, the two-dimensional LDF is used. In section 8.1.1 the reduction of the two-dimensional LDF for AERA and the possibility to determine the radiation energy with the two-dimensional LDF will be discussed.

5. Preparatory Studies

During the course of this work some aspects of the general feasibility of the radio detection of horizontal air showers were investigated. First, the reconstruction efficiencies of vertical and horizontal showers were studied, described in section 5.1. Then, prototype stations were deployed at the AERA site in order to quantify the importance of the vertical component of the electric field. This is described in section 5.2.

5.1. Reconstruction Efficiency

To get a better understanding what can be gained by the radio detection of extensive air showers compared to the detection of extensive air showers with SD and FD it is important to quantify the efficiency of AERA, which is triggered by the Auger surface detector. The relative reconstruction efficiency is studied in this section and defined as the number of reconstructed cosmic ray event candidates divided by all reconstructed events of the reconstruction pipeline of AERA. This gives a hint how good the AERA reconstruction works and how much can be expected regarding the determination of physical parameters of the cosmic air shower.

In this study the closest AERA station to the core position reconstructed by SD was taken and the magnitude of the highest pulse in the AERA trace was analysed. This was done for vertical and horizontal air showers separately due to different reconstruction pipelines and is explained in subsections 5.1.1 and 5.1.2. To first approximation the closest AERA station to the SD core position has the highest signal.

In the AERA trace of the closest station the time of the highest pulse is determined. To be independent from fluctuations of ADC values, the Hilbert envelope of the magnitude of the electric field strength is considered for this. The magnitude of the electric field strength is calculated as the magnitude squared of the absolute north-south and the east-west components of the electric field. The not measured vertical component, which can be extracted by the geometry of the shower and the antenna pattern of the station, was not evaluated due to high uncertainties. In section 5.2 the vertical component is discussed further. All externally triggered events stored by the AERA DAQ are considered. Core position and direction of the shower are taken from the SD reconstruction. On the basis of the position of the highest pulse in the trace a difference between the measured arrival time and

the expected time is calculated. A sketch of the timing calculation is shown in figure 5.1. This calculation of the expected time is now used in the current RdObserver version v1r3 to determine the pulse search window.

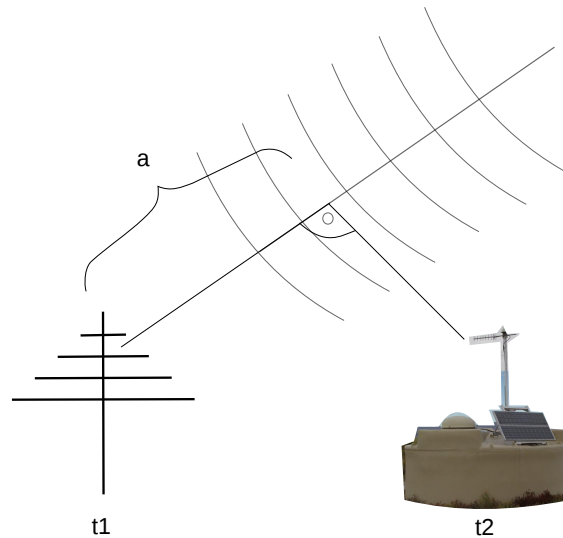


Figure 5.1.: Sketch of the calculated difference of measured and expected time of the pulse in the AERA trace. t_2 is the measured time at the surface detector tank (orthogonal to the SD shower axis) and t_1 the time of the radio pulse in the AERA trace. The radio shower front travels the distance a with the speed of light.

5.1.1. Reconstruction Efficiency - Vertical Events

The SD Infill reconstruction is valid in the zenith angle range from 0° to 55° . One typical AERA trace of such a vertical event is shown in figure 5.2. The following quality cuts are applied:

- take events which pass the SD Infill reconstruction quality cuts, as θ smaller than 55°
- exclude SD Infill bad periods
- exclude time periods of modification or maintenance of AERA stations [2012/02/28–2012/03/04]
- exclude AERA Octocopter calibration [2012/11/30–2012/12/10]

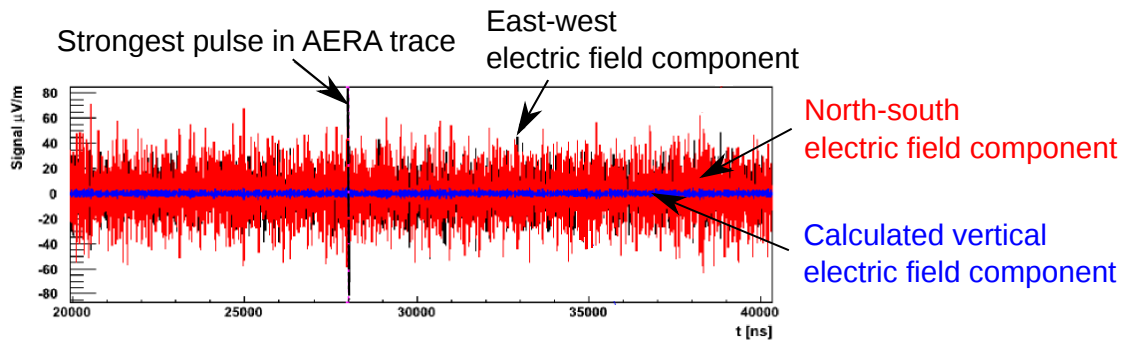


Figure 5.2.: AERA trace of a vertical event. In red the north-south component, in black the east-west component and in blue the calculated vertical component of the electric field strength is shown. The dashed line marks the strongest pulse in the trace.

To be able to derive predictions for physical parameters the following physical cuts are applied:

- select events with energy reconstructed by SD of larger than 10^{17} eV
- distance to closest AERA station to the reconstructed shower axis of SD of smaller than 200 m

Applying these cuts and calculating the time difference of expected and measured time results in the time distribution shown in figure 5.3. The histogram on the left shows a peak in the interval of $\pm 2\mu\text{s}$. Taking the events in this time interval and plotting the electric field amplitude against the energy reconstructed by SD shows that the radio amplitude correlates with the cosmic ray energy. In figure 5.4 the distance to the closest AERA station to the shower axis reconstructed by SD versus the energy reconstructed by SD for events fulfilling the selection criteria of energy larger than 10^{17} eV and distance to the shower axis of smaller than 200 m are shown. In red the events in the expected time window and in black the events not in the expected time window are shown. Reducing the distance to the closest station or increasing the energy of the cosmic ray event improves the probability to detect a cosmic ray event candidate up to 75% reconstruction efficiency [88], which can be considered as a large enough reconstruction efficiency to be useful. The efficiency of 28.3% was derived with the described cuts for the time period of 2012/01/01 to 2012/12/10. The reconstruction efficiency defined here is derived by a simple approach considering the time of the detected pulse in the closest radio station to the shower core reconstructed by SD. Adding the second and third closest station improves the reconstruction efficiency.

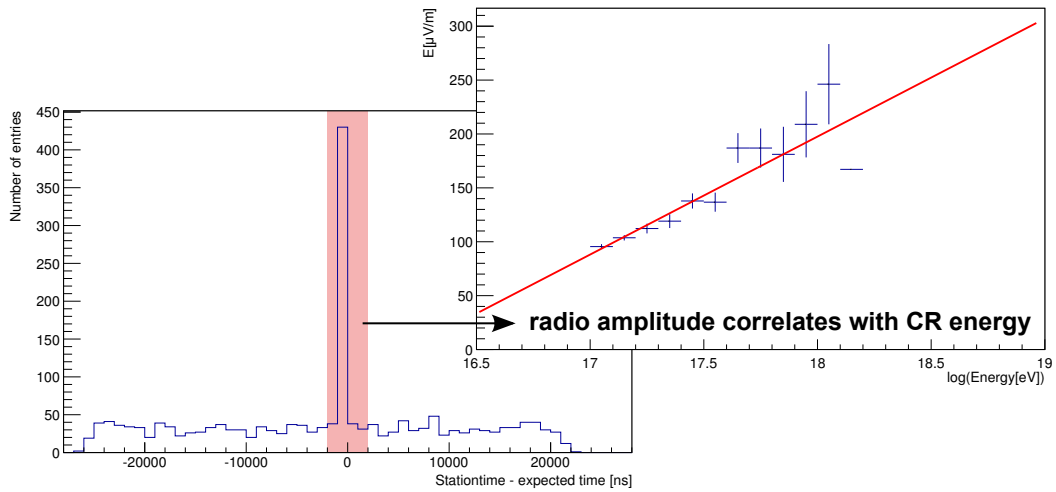


Figure 5.3.: Difference of measured and expected time. Events in the time interval of $\pm 2\mu\text{s}$ show that the radio amplitude correlates with the cosmic ray energy.

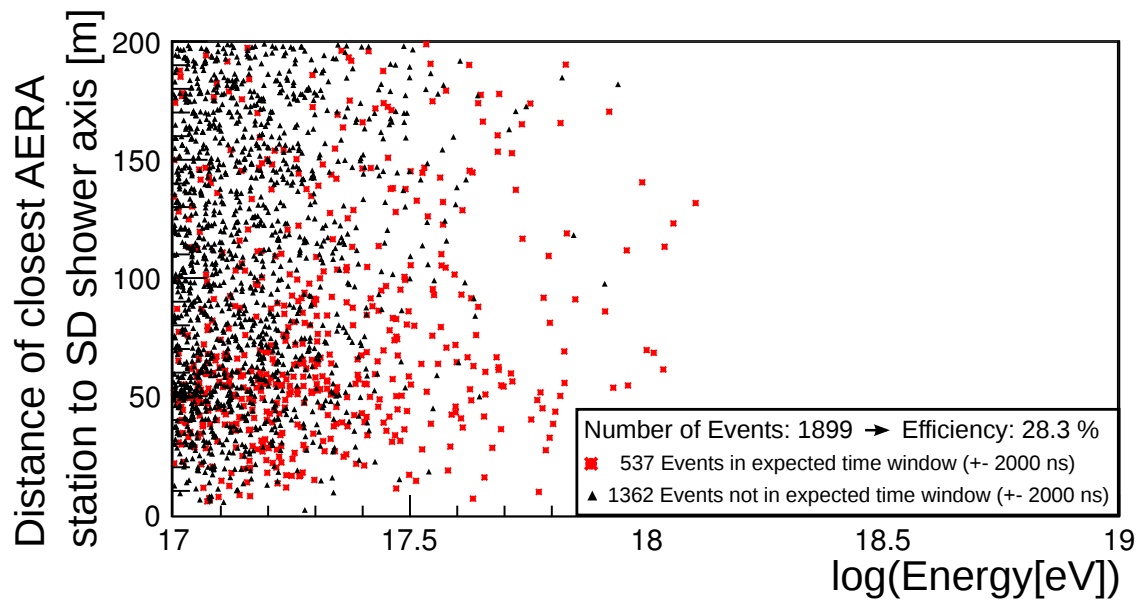


Figure 5.4.: Events with $\theta < 55^\circ$ (standard SD Infill reconstruction) as a function of energy and distance. In red the events in the expected time interval and in black the events not in the expected time interval are shown.

5.1.2. Reconstruction Efficiency - Horizontal Events

The AERA reconstruction efficiency analysis of horizontal events was published as a conference proceeding [20]. A surface detector reconstruction for events with zenith angles larger than 55° has never been validated for the SD Infill array. To derive valid values for the SD reconstructed parameters the SD HAS reconstruction of the SD array for horizontal air showers was used. One AERA trace of a horizontal event example is shown in figure 5.5.

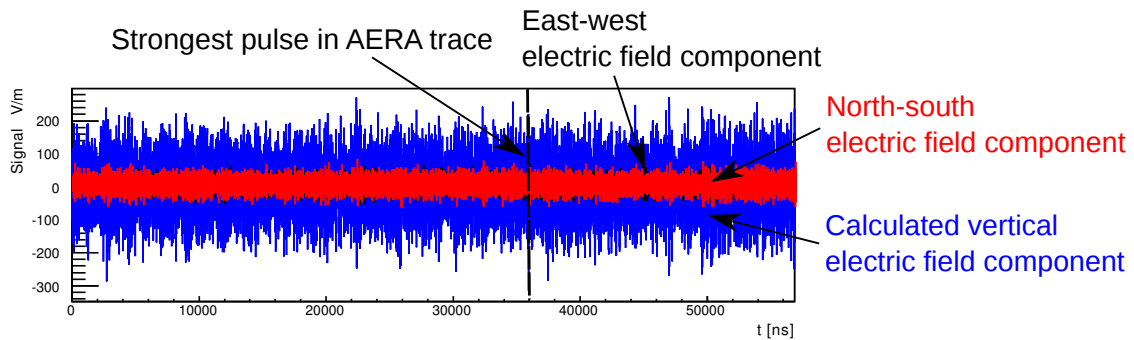


Figure 5.5.: AERA trace of a horizontal event. In red the north-south component, in black the east-west component and in blue the calculated vertical component of the electric field strength is shown. The dashed line marks the strongest pulse in the trace.

The horizontal component has large fluctuations due to the uncertainty of the antenna pattern for horizontal events and due to the higher noise background. Therefore only the east-west and north-south component was used. The event selection criteria for the single pulse analysis of horizontal events are:

1. take all externally triggered events by surface detector stored by AERA DAQ
 - that means 2.5 years of data taking:
 - AERA-24: [2012/01/01–2013/04/07]
 - AERA-124: [2013/04/22–2014/03/13]
2. no SD energy cut
3. apply SD HAS quality cuts, as defined for the ICRC 2013:
 - zenith angle $62^\circ - 80^\circ$
 - minimum of 4 SD tanks
 - independent reconstruction of FD energy
 - apply SD T4 trigger cut (Physics trigger) [45]

5. Preparatory Studies

- apply SD T5 trigger cut (Quality trigger) [45]
 - exclude SD bad periods
4. search for the highest pulse in the closest AERA station
 5. apply signal-to-noise (SNR) cut of 8 to highest pulse in the AERA trace
 6. distance of the closest AERA station to the SD shower axis should be smaller than 10 km

There are no energy selection criteria needed, because the SD array is more efficient for events with higher energies than the SD Infill array due to the larger distance of the SD tanks. The maximal distance of the closest AERA station to the SD shower axis could be enlarged to 10 km.

The histogram with the station time minus the expected time, which can be seen in figure 5.6, shows a broader peak for horizontal events than for vertical events. The reason for this could be the larger uncertainties of the SD HAS reconstruction. The distance of the SD tanks is 1500 m instead of 750 m for the SD Infill. Additionally, the maximal allowed distance of the closest AERA station to the SD shower axis is enlarged, so the selected event sample could contain more background events. The background by noise contamination can be larger in radio for horizontal events. A time difference of $\pm 7\mu\text{s}$ has been used to define reconstructed cosmic ray candidates. Figure 5.7 shows the events which fulfil the distance cut of 10 km.

Increasing the cosmic ray energy and decreasing the distance to the closest station raises the probability to detect a cosmic ray event, as for vertical events. The calculation of the efficiency results in 30.0%. The number of events is smaller for horizontal air showers than for vertical events, because the SD array and not the SD Infill array is used to reconstruct the events. This method needs further improvement, because, as can be seen in figure 5.7 in the right lower corner one high energetic event with its radio lateral distribution can be seen, which originates from a cosmic ray event, but has the highest pulse not in the right time interval and therefore would not pass the selection criteria. The events are plotted in figure 5.8 on the left in polar coordinates and the SD core distribution is shown on the right. The core position of horizontal events does not have to be inside the AERA array to be a cosmic ray candidate.

The reconstruction efficiency of horizontal air showers is not worse than the reconstruction efficiency of vertical showers. The two efficiencies are difficult to compare because of the different SD grids. The grid distance is 750 m for vertical events and 1500 m for horizontal events. Therefore the uncertainties of the reconstructed parameters of SD differ too for vertical and horizontal events. The method described in this section helped to define the search window currently used for the cosmic ray pulse in the official Offline reconstruction of AERA data.

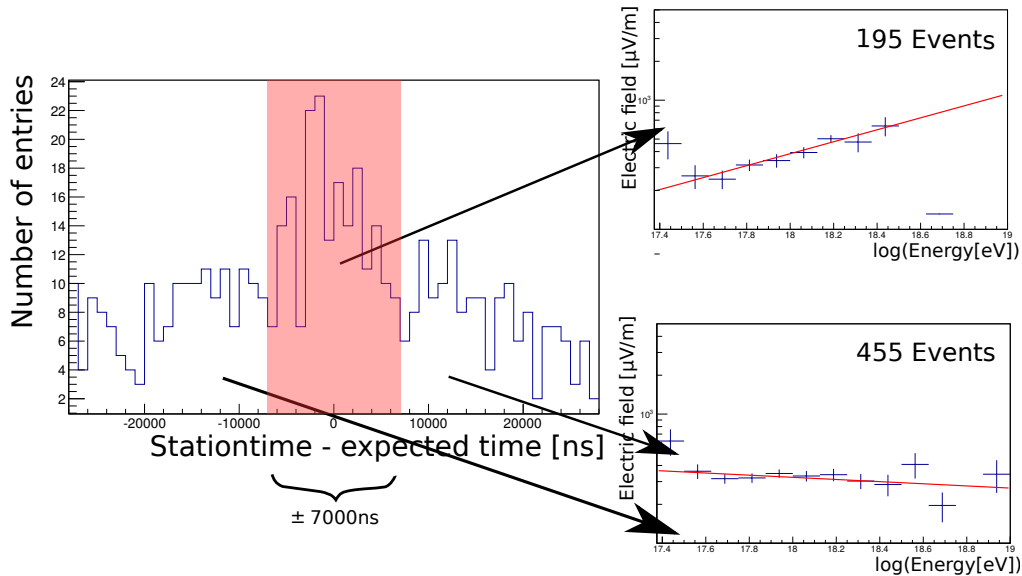


Figure 5.6.: Difference of measured and expected time. Events in the time interval of $\pm 7\mu\text{s}$ show a correlation of amplitude of the electric field and cosmic ray energy determined by SD.

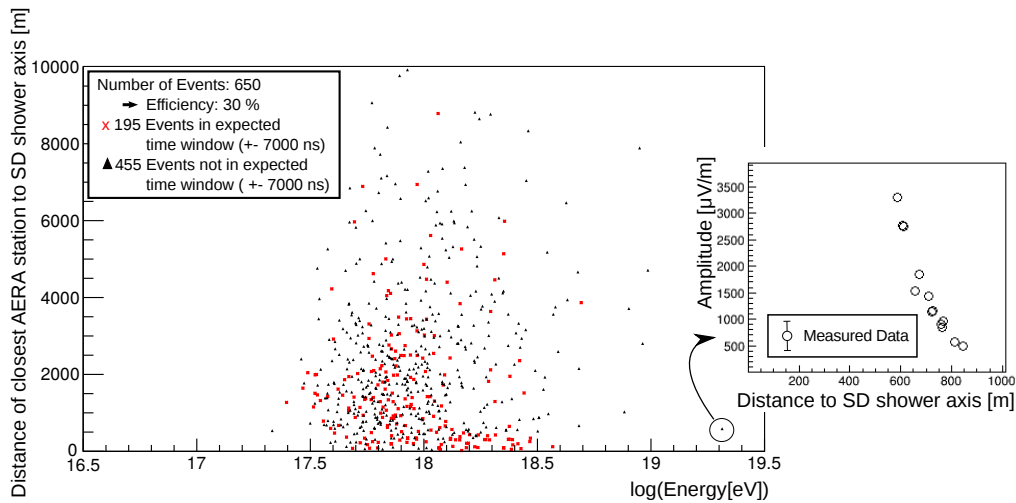


Figure 5.7.: The events which pass the horizontal event selection criteria are shown. 195 of 650 events pass the time difference of $\pm 7\mu\text{s}$ in measured and expected time. These events are drawn in red. In black the events with larger than $\pm 7\mu\text{s}$ time difference of measured and expected time are shown. On the lower right corner the LDF of a high energetic cosmic event is shown, which is not in the expected time probably because of the wrong determined core position by the SD HAS reconstruction.

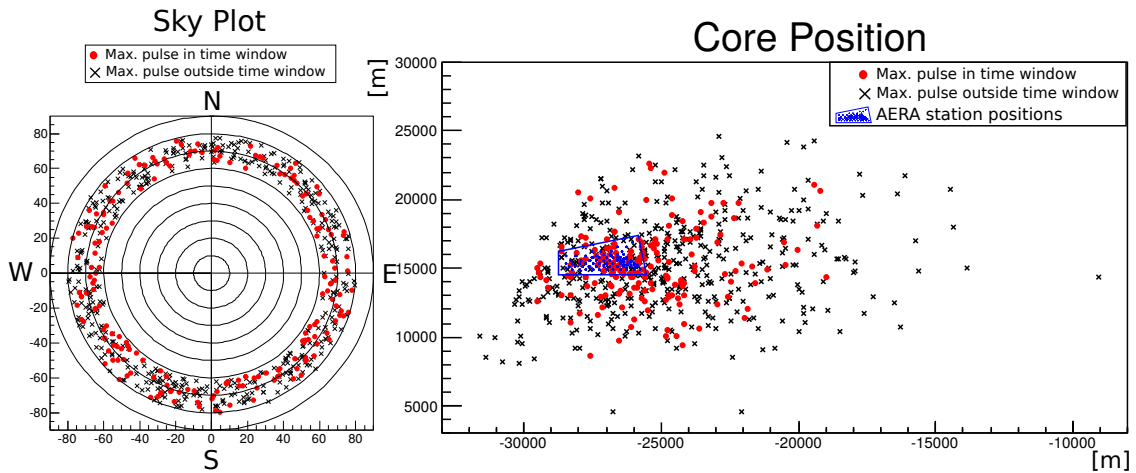


Figure 5.8.: The events which pass the horizontal event selection criteria are shown. On the left the Sky plot and on the right the distributions of the SD cores can be seen. In red the events inside the $\pm 7\mu\text{s}$ time interval and in black the events outside the $\pm 7\mu\text{s}$ time interval are shown.

5.2. Prototype Stations

During the course of this work three tripole stations and one prototype station for low-frequencies were proposed, designed, assembled and installed at the Auger site in Argentina. The intention was to extend the existing antenna technique by a direct measurement of the vertical component of the electric field with tripole antenna stations and explore the potential of low-frequency radio detection in the 1.5 – 6.5 MHz range. Below 10 MHz a minimum external noise is expected during night measurements [89].

In order to determine the strategy for next generation radio detector experiments it is important to investigate the optimal antenna configuration and design. Key aspects are the sensitivity to all incoming directions, finding the optimal frequency range and the coverage of large areas at low cost.

5.2.1. Horizontal Component

In the example trace seen in figure 5.5 the calculated horizontal component can become larger for horizontal air showers than the horizontal component for vertical air showers. An example trace of a vertical event can be seen in figure 5.2. The relative strength of the electric field component assuming purely geomagnetic radiation for the AERA site can be seen in figure 5.9. For the geomagnetic radiation the horizontal component is larger than the north-south component.

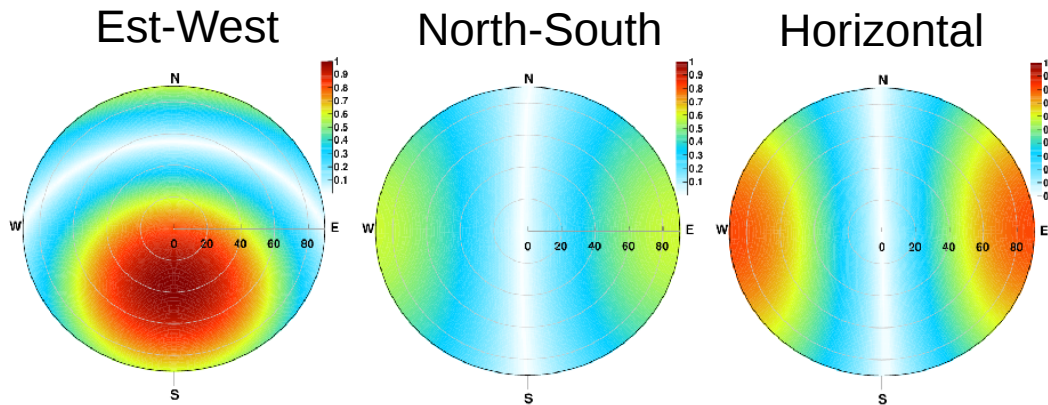


Figure 5.9.: Relative strength of the electric components for pure geomagnetic radiation at the Auger site. [90].

The horizontal component of the electric field vector was first studied at the LOPES site [39]. The result was that measuring the horizontal component of the electric field directly did not improve the reconstruction of LOPES data due to the noise background. By installing the LOPES-3D [91] antennas at the Auger site, conclusions gained by the LOPES experiment are validated in this thesis.

5.2.2. Prototypes Installed at the Auger Site

In the Offline reconstructions of AERA data the magnitude of the north-south and east-west component of the electric field is used, because the calculated horizontal component underlies too much fluctuations. The reason for this can be the larger uncertainties of the antenna pattern. In order to test if measuring the horizontal component of the electric field improves the reconstruction three LOPES-3D tripole antennas were attached with new AERA hardware and installed on the AERA field with a distance of 750 m between the stations and one low-frequency antenna with three polarisations were installed in the AERA-24 field. A map of the station positions can be found in figure 5.10. A photograph of the deployed tripole station can be seen in figure 5.11. After the deployment of the prototype stations the spectra were measured. The spectra of the tripole station number 87 can be seen in the upper plot of figure 5.12 and the spectra of the low-frequency station can be found in the lower plot of figure 5.12. The spectra of the tripole station reveals that the station has some hardware problems indicated by the high and broad peaks in the east-west and north-south component. Unfortunately all three tripole stations showed similar peaks in the spectra. Problems with the grounding of the electronics and the antennas were assumed and fixed. The high and broad peaks still remained.

5. Preparatory Studies



Figure 5.10.: Positions of the four prototype stations deployed at the Auger site. Three tripole stations with LOPES 3D antennas with station number 87, 91 and 98 and one low-frequency station with station number 107 have been deployed from 15 November 2013 till 22 November 2013.



Figure 5.11.: Photograph of AERA station number 98. The LOPES 3D antenna can be seen next to the station sign.

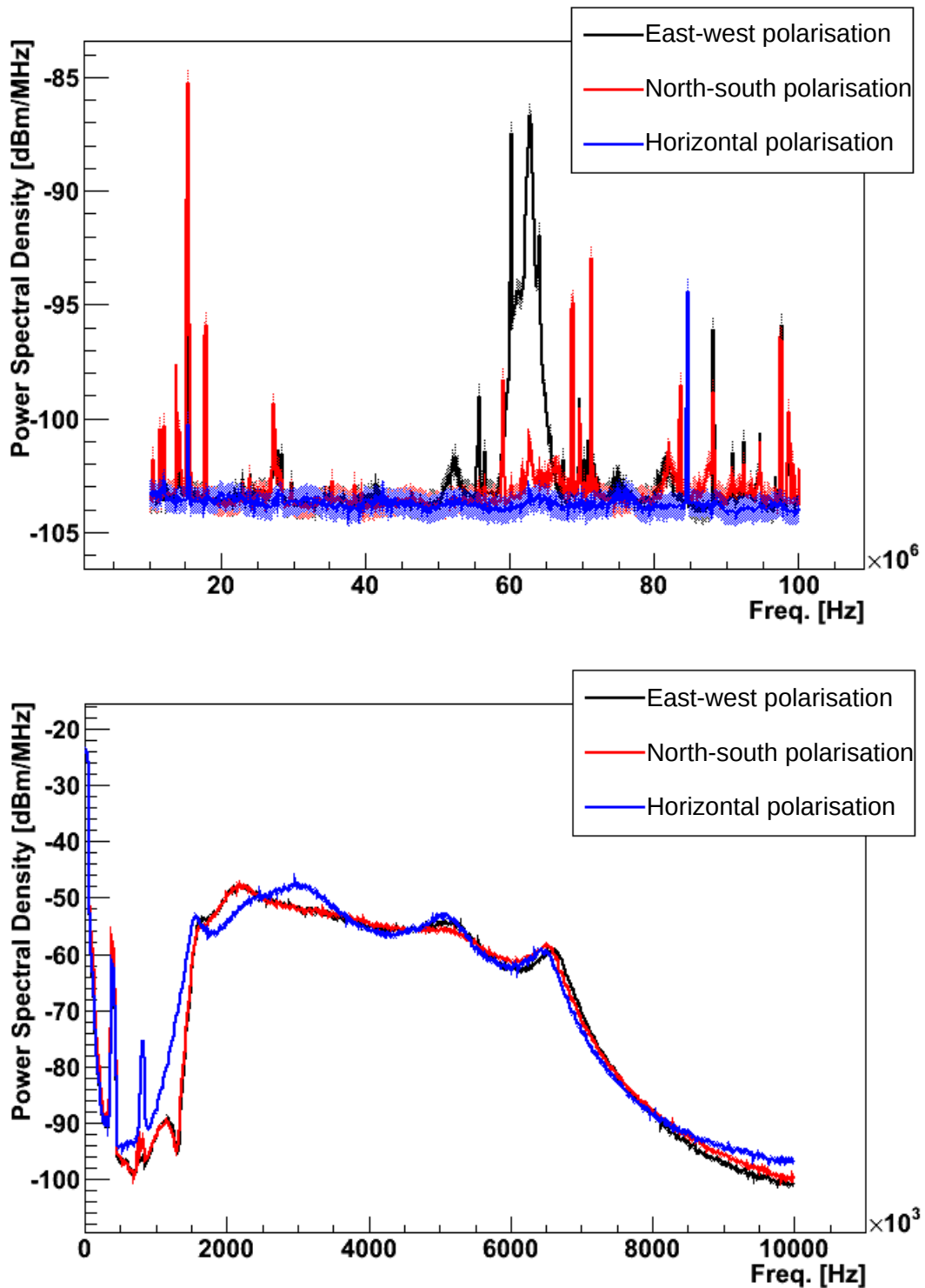


Figure 5.12.: The spectrum of the station 87 (tripole station) on the upper part and the spectrum of station 107 (low-frequency station) on the lower part [92]. In black the east-west, in red the north-south and in blue the horizontal polarisation are drawn.

5. Preparatory Studies

First events including the prototype stations like the event shown in figure 5.13 have been detected by AERA. The trace of the Butterfly station number 66 is shown on the right corner of the figure. The pulse can be seen at 1000 ns. The trace of the AERA station number 87 belongs to one tripole station. The pulse can also be seen at around 1000 ns, but there is more noise and the peak is broader. The reason for this is the missing antenna calibration and the broad peaks in the frequency spectra. The pulse in the trace of station 107 shows no clear peak, because an antenna pattern was not available the time the reconstruction was performed.

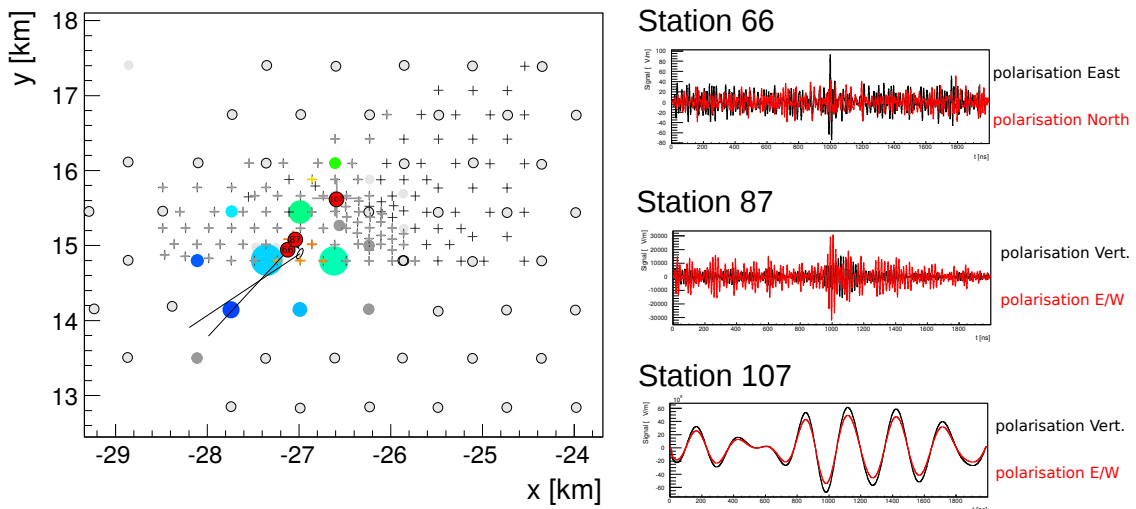


Figure 5.13.: The AERA array is shown on the left and the traces of the stations are shown on the right. AERA event measured in station number 66 (Butterfly station), station number 87 (tripole station) and station number 107 (low-frequency station). The prototype stations are marked with red circles and station numbers in the array plot.

The isolation problem of the tripole stations could not be solved in several repair campaigns and no further attempts were made to improve the reconstruction of the data taken by the tripole stations. Future plans are to exchange the tripole antennas with short aperiodic loaded loop antennas (SALLA), like the ones used in Tunka-Rex, to test the robustness of the SALLA towards the noise conditions at the Auger site.

The noise background for the low-frequency station was analysed in [93]. The low-frequency station had no obvious hardware defects after deployment and the frequency spectra (lower plot of figure 5.12) looked like expected from laboratory measurements. The strong suppression of the noise during night in the below 10 MHz range (see figure 5.14) could not be confirmed with the low-frequency sta-

tion at the Auger site. The measured suppression factor is between 1.4 and 2.7 [93] instead of the expected factors from 10 to 10^8 . No correlation between the shower parameters radio amplitude, energy and the distance to the core could be derived and therefore no physics analysis could be performed.

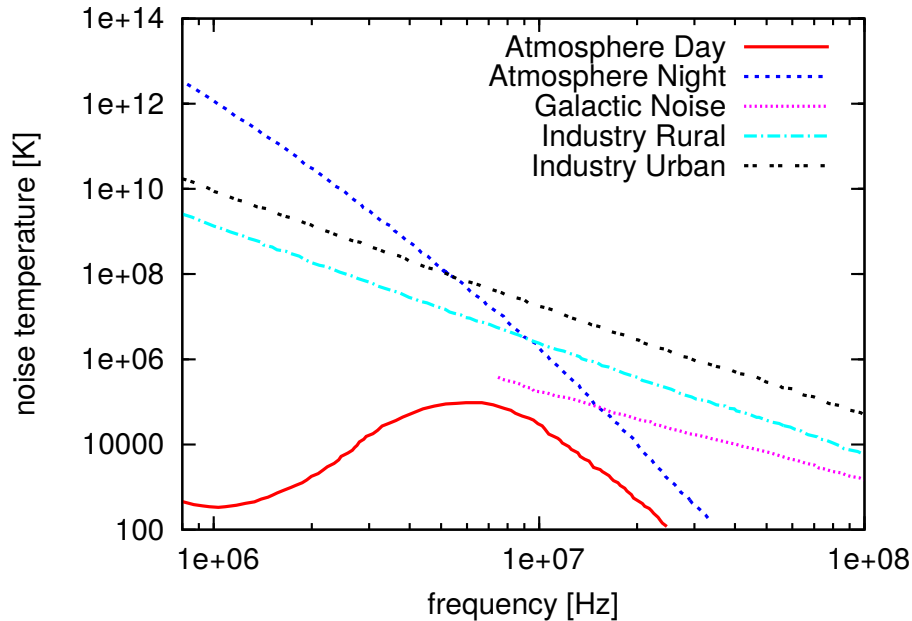


Figure 5.14.: Minimum world-wide background noise temperatures according to CCIR report 670 [94].

The experimental investigation of the measurement of the horizontal polarisation component of the radio signal was not successful at the Auger site, therefore an improvement of the reconstruction could not be shown. In parallel standard measurements with AERA have shown that a detection and reconstruction of horizontal air showers is possible with two polarisations (see chapter 6 to 8). Therefore, this path of investigations was stopped. The deployment and commissioning of the low-frequency station was successful, but the predicted suppression factor could not be confirmed with the measurement at the Auger site. In the course of this installation campaign the software of the read out of the AERA electronics was adapted and it is now possible to readout three instead of two channels. This will make AERA more flexible towards future requirements.

6. Reconstructed Data Sample and Data Selection

The AERA data used in this work is reconstructed from all externally triggered events taken by the AERA data acquisition from January 1, 2012 to August 15, 2015. Stations with internal trigger are not considered, because for them another reconstruction chain is required and they are not optimised for horizontal air showers. At the beginning of this time period the array consisted of 24 LPDA stations only. One year later 100 Butterfly stations were added and in 2014 25 additional Butterfly stations with a spacing up to 750 m between the stations were deployed. Thus, the data set comprises different set-ups of AERA regarding antenna types and spacing of stations. As the physics is independent of the AERA stage the data set is treated as a whole. The different phases of AERA are given in section 3.4. RdObserver [95] is the standard AERA reconstruction pipeline. RdObserver is based on the SD Infill reconstruction. The reconstructed SD core and direction are used as initial values for the radio reconstruction. However, the SD Infill reconstruction is valid up to zenith angles of 55° only. In the course of this work the RdObserver was extended for horizontal events. The so-called RdHASObserver is valid in the zenith angle range of 62° to 80° . The RdHASObserver is based on the SD HAS reconstruction, the reconstruction pipeline for horizontal air showers for SD. The performance of the RdObserver is explained in section 6.1 and those of the RdHASObserver in section 6.2. In section 6.3 simulations of the observed events generated with CoREAS are discussed and in section 6.4 the horizontal polarisation component of the electric field of the reconstructed data is evaluated.

6.1. RdObserver

The RdObserver has been developed to reconstruct AERA data. It is the standard reconstruction for vertical events. In order to compare the reconstructed vertical events with the reconstructed horizontal events the RdObserver is applied to the complete AERA data sample. The RdObserver is based on the SD Infill (SD tanks of 750 m spacing) reconstruction. The reconstruction pipeline is described in section 4.1. Taking all externally triggered AERA events, applying the SD Infill reconstruction and then the RdObserver v1r3 (version 1, revision 3) gives the following output:

6. Reconstructed Data Sample and Data Selection

- 6721 events from 2012/01/01 to 2015/08/15
- 4 events observed by more than 50 AERA stations
- 13 events with SD energy greater than 10 EeV
- 535 events observed also by FD (no FD cuts applied)

SD Infill quality cuts [96] have to be applied to guarantee a valid core, direction and energy reconstruction. A summary of the cuts is shown in table 6.1. The cut on the zenith angle reduces the data sample to vertical events. Applying all cuts results in 3670 high quality events with zenith angles up to 55° .

To be able to reconstruct a direction with AERA three radio stations are required. The difference of the reconstructed direction of SD and AERA should be smaller than 20° in order to suppress noise pulses and the signal-to-noise (SNR) ratio should be larger than 10. These three cuts are applied during the reconstruction of AERA data before applying the quality cuts of SD.

Cut	Value	Description	Events dropped
maxZenithSD	55°	maximum zenith angle	1567
T5Trigger	2	minimum T5 flag - Quality trigger	1682
T4Trigger	2	minimum T4 flag - Physics trigger	535
minRecLevel	3	has LDF fit	0
All events			6721
Selected events			3670

Table 6.1.: Summary of the SD Infill cuts applied on the RdObserver data set of 6721 events. Each cut is performed separately. Applying all cuts results in 3670 selected RdObserver events.

The SD Infill energy distribution of the selected event is shown in figure 6.1. The mean value is 3×10^{17} eV. The event with the lowest energy which passes all cuts has an SD energy of 2×10^{16} eV. The reconstruction efficiency of the SD Infill array is 100% for events with energies above 3×10^{17} eV [58]. The full efficiency of SD will be important for the reconstruction of simulations of measured events. The sky plot of the selected events can be seen in the left panel of figure 6.2. The electric field strength is proportional to $\sin(\alpha)$, the sine of the geomagnetic angle α . A north-south asymmetry can be seen in the right plot of figure 6.2. Fewer events coming from north are detected, because events with arrival direction vertical to the magnetic field are preferred. Figure 6.3 shows the number of stations for several zenith angle bins. Each point corresponds to one of the 3670 events. In red the profile plot is drawn. For an increased zenith angle it is expected to have a higher

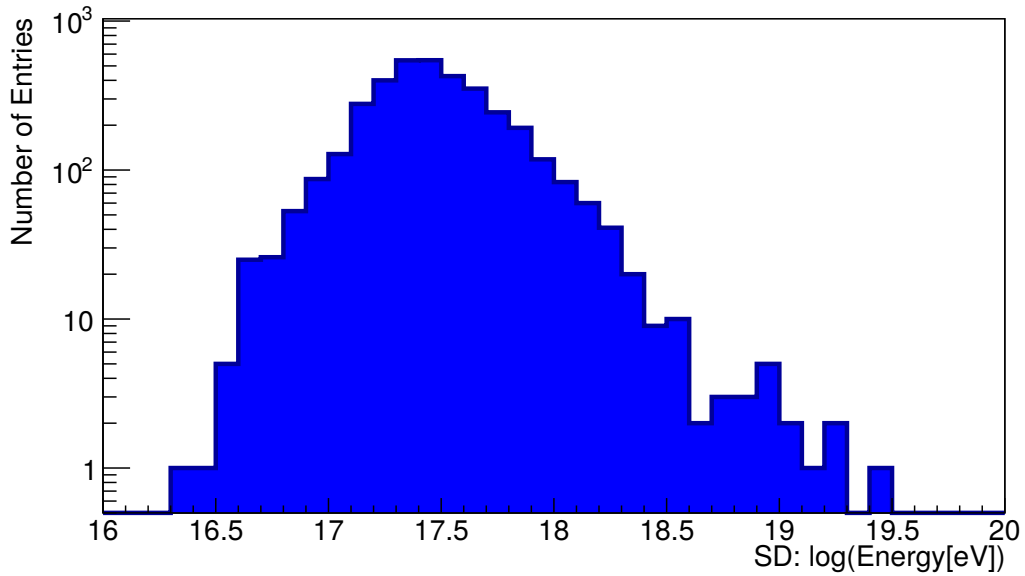


Figure 6.1.: SD Infill energy distribution of the 3670 selected RdObserver events with less than 55° . The mean value is 3×10^{17} eV.

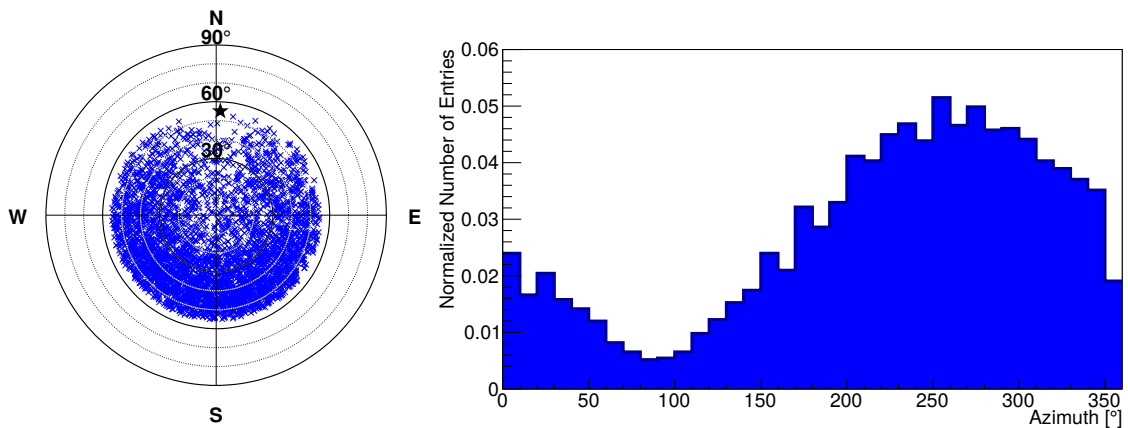


Figure 6.2.: On the left the sky plot of the selected 3670 RdObserver events is shown. The circles show the zenith angle and the angle starting from east (anticlockwise) the azimuth angle. An azimuth angle of 90° corresponds to north. The cardinal directions are marked with N, E, S and W. The direction of the magnetic field is marked with a star. On the right the azimuth angle distribution is shown. The sine shape is visible and the minimum is at $\approx 90^\circ$ azimuth angle, which corresponds to the north direction.

station multiplicity due to the larger footprint of the shower (see section 2.4). The highest value for 55° of zenith angle has a maximum of 34 stations and a mean value of 7 stations per event.

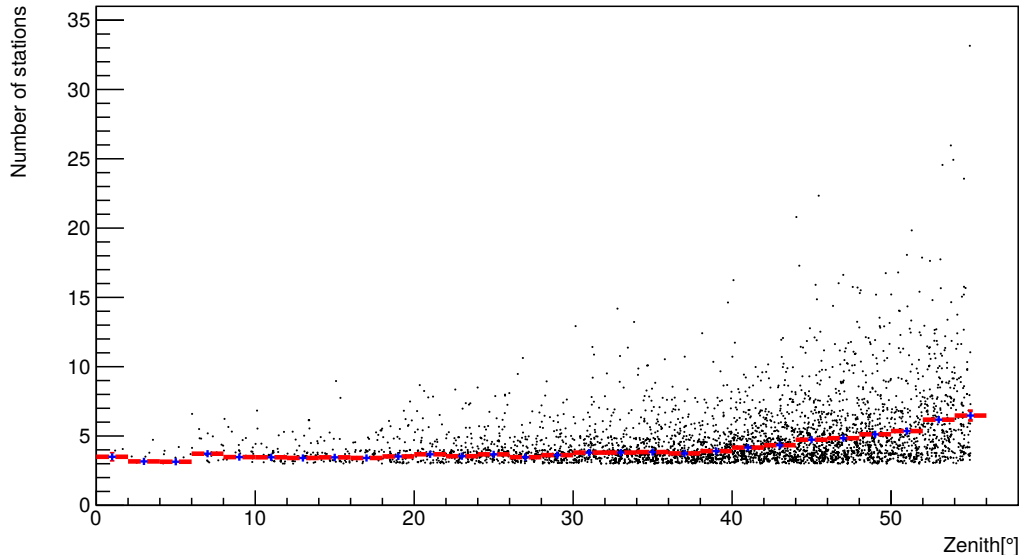


Figure 6.3.: Station multiplicity of the selected 3670 RdObserver events. A minimum of three AERA stations is required for the RdObserver. In red the profile plot is drawn. The station multiplicity rises with zenith angle due to the larger radio footprint of horizontal events compared to vertical ones.

The energy reconstructed by SD and the core reconstructed by SD have some uncertainties. In figure 6.4 on the left the relative uncertainty of the SD energy of the selected events is shown and on the right the area of the uncertainty ellipse of the SD shower core position is shown. The uncertainty ellipse corresponds to one standard deviation of the SD core uncertainty. An SD reconstruction for events with zenith angles larger than 55° has never been validated for the SD Infill. A horizontal event measured by AERA-153 and reconstructed by the RdObserver, can be seen in figure 6.5. The event was reconstructed with the SD Infill array. The SD tanks outside the SD Infill array are not considered for this reconstruction, although the SD tanks outside the SD Infill array should also have signals above trigger threshold because of the large shower footprint. Therefore, a radio reconstruction based on the SD standard HAS reconstruction, the RdHASObserver, was developed to improve the reconstruction of horizontal air showers.

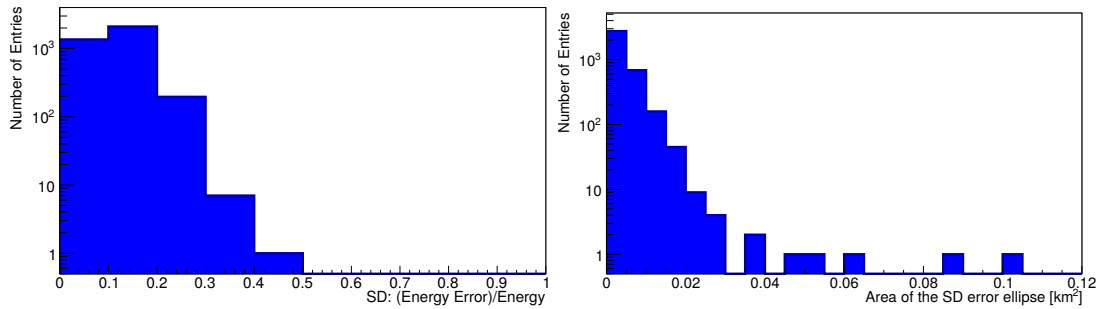


Figure 6.4.: On the left the uncertainty of the energy determined by SD is drawn. The mean value of the relative uncertainty of the SD energy is 11%. On the right the area of the SD core uncertainty ellipse of the selected 3670 RdObserver events is drawn. The mean value is 0.0042 km².

6.2. RdHASObserver

In course of this work the RdHASObserver has been developed to reconstruct horizontal AERA data. The sequence of the reconstruction steps of the RdHASObserver can be found in appendix A.1. As input the parameters of the SD HAS reconstruction (SD tanks of 1500 m spacing) are used. Concerning the SD Infill only every second SD infill tank is considered for this reconstruction, so that the spacing of SD tanks is also 1500 m for the area of the SD Infill. A description of the SD HAS reconstruction can be found in [45]. Applying the RdHASObserver to the AERA data set gives the following output:

- 866 events from 2012/01/01 to 2015/08/15
- 21 events observed by more than 50 AERA stations
- 17 events with SD energy greater than 10 EeV
- 45 events observed also by FD (no FD cuts applied)

The number of events is smaller than for the RdObserver due to the smaller zenith angle range and due to the larger SD grid size of 1500 m instead of 750 m for the SD Infill array. Therefore, more events observed by more than 50 AERA stations and more events with SD energy greater than 10 EeV are reconstructed than for the RdObserver. FD has an uptime of $\approx 13\%$ due to the detector requirements of moonless nights [60]. Therefore, the number of FD events in the RdHASObserver sample is accordingly smaller too. To obtain events with valid SD core, direction and energy reconstruction, the SD HAS quality cuts of table 6.2 have to be applied. 427 RdHASObserver events pass all quality cuts.

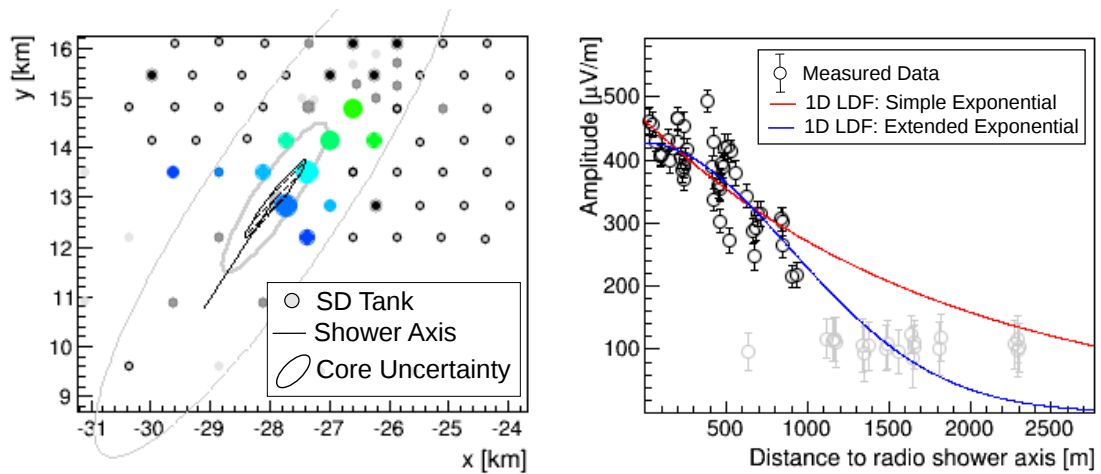


Figure 6.5.: Event measured with the AERA-153 experiment. Reconstructed with RdObserver version v1r3. 44 AERA stations passed the SNR cut, zenith angle 78° , SD energy 1.3 EeV. On the left the SD event array signal is shown. Each circle marks one SD tank. The coloured SD tanks are above signal threshold and are considered for the geometrical fit of the shower parameters. The size of the circles mark the signal strength and the colour code indicates the arrival time of the shower. The direction of the shower is marked with a line and the core uncertainties are drawn as uncertainty ellipses around the core position. The hashed area represents one standard deviation of the core uncertainty. On the right the radio lateral distribution function is shown. Each station above signal threshold is drawn as one black circle with error bars. The stations in gray are below signal threshold and are not considered for the fit of the lateral distribution function. In red an exponential and in blue an extended exponential function are drawn. The mathematical description of the functions can be found in section 4.3.

Again, the minimum of three AERA stations, the difference of less than 20° in the reconstructed direction of SD and AERA and the SNR larger than 10 is required during the reconstruction of AERA data. This is applied before applying the SD HAS quality cuts.

Cut	Value	Description	Events dropped
minZenithSD	62°	minimum zenith angle	222
maxZenithSD	80°	maximum zenith angle	93
minCandidateStations	4	minimum candidate stations	192
T5Trigger	3	minimum T5 flag - Quality trigger	81
T4Trigger	2	minimum T4 flag - Physics trigger	8
minRecLevel	3	has LDF fit	0
All events			866
Selected events			427

Table 6.2.: Summary of the SD HAS cuts applied to the RdHASObserver data set of 866 events. Each cut is done separately. Applying all cuts results in 427 selected events.

The SD energy distribution of the selected events can be seen in figure 6.6. The mean value is 1×10^{18} eV. The reconstruction efficiency of the SD array is 100% for events with an energy above 4×10^{18} eV for horizontal showers [96]. This energy is significantly higher than for the SD Infill. The sky plot (6.7, left figure) and the azimuthal distribution (6.7, right figure) show similar characteristics to the RdObserver selection, but less dominant reduction of events coming from the north. The station multiplicity (figure 6.8) rises up to 70 stations per event and its mean value is between 10 and 20 for each zenith angle bin. Thus, the RdHASObserver makes the reconstruction of events with higher energies and larger footprints possible.

Due to the different SD reconstruction the uncertainties on the SD energy and SD core are larger. In the left figure of 6.9 the relative uncertainty on the SD energy is shown. The mean value of the relative SD energy uncertainty of selected RdHASObserver events is 34%, compared to 11% of the RdObserver. On the right figure of 6.9 the area of the SD core uncertainty ellipse is shown. The mean value is 0.48 km^2 , compared to 0.0042 km^2 of the RdObserver.

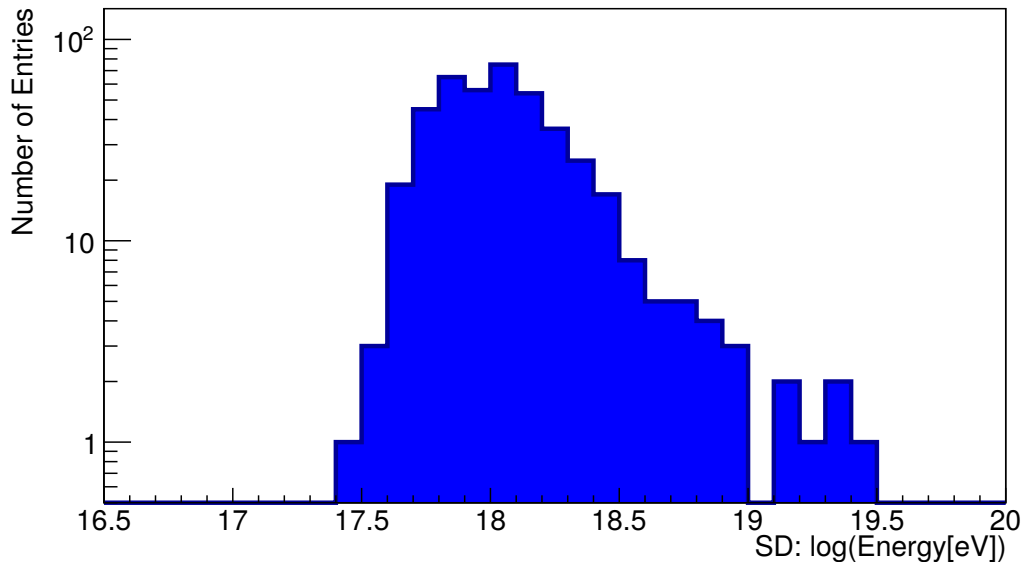


Figure 6.6.: SD energy distribution of the 427 selected RdHASObserver events. The mean value is 1×10^{18} eV.

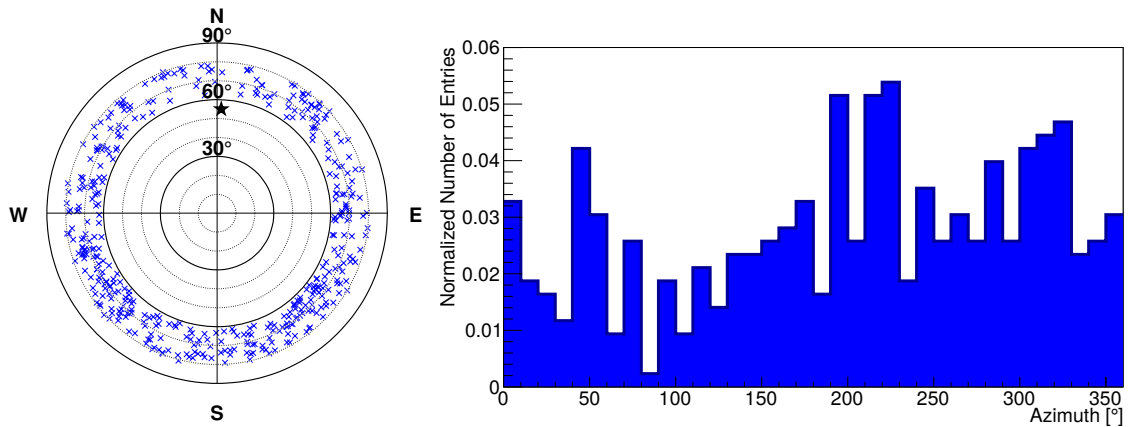


Figure 6.7.: On the left the sky plot of the selected events is drawn. The circles show the zenith angle and the angle starting from east (anticlockwise) the azimuth angle. The cardinal directions are marked with N, E, S and W. The direction of the magnetic field is marked with a star. On the right the azimuth angle with the sine shape is shown. The minimum is at 90° azimuth angle, which corresponds to the north direction.

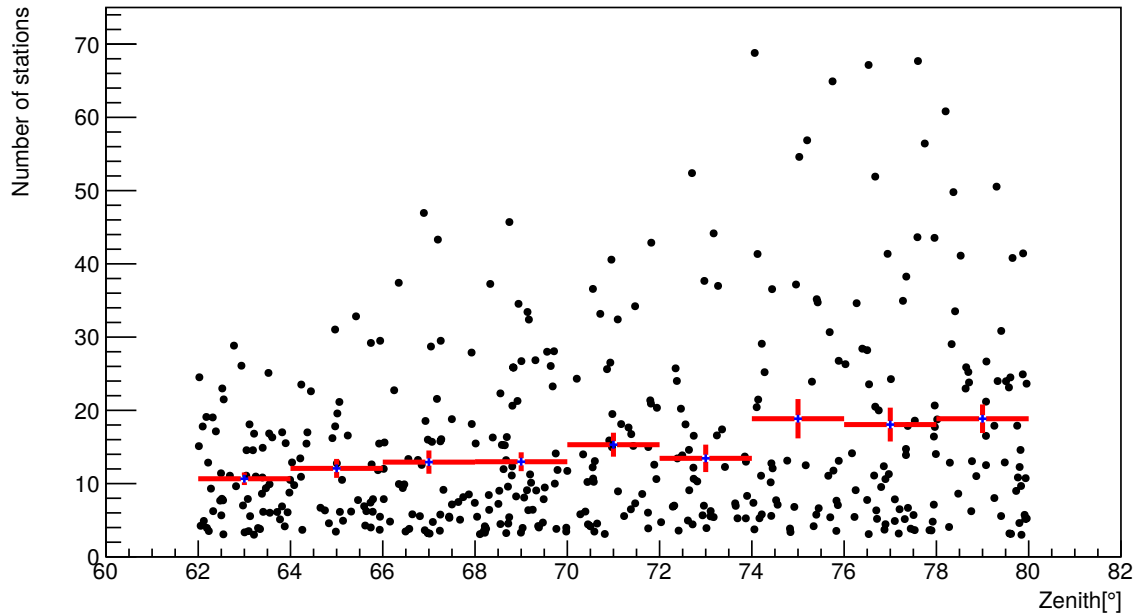


Figure 6.8.: Station multiplicity distribution of the selected 427 RdHASObserver events. A minimum of three AERA stations is required for the RdHASObserver. In red the profile plot is drawn. The station multiplicity rises with zenith angle due to the larger radio footprint.

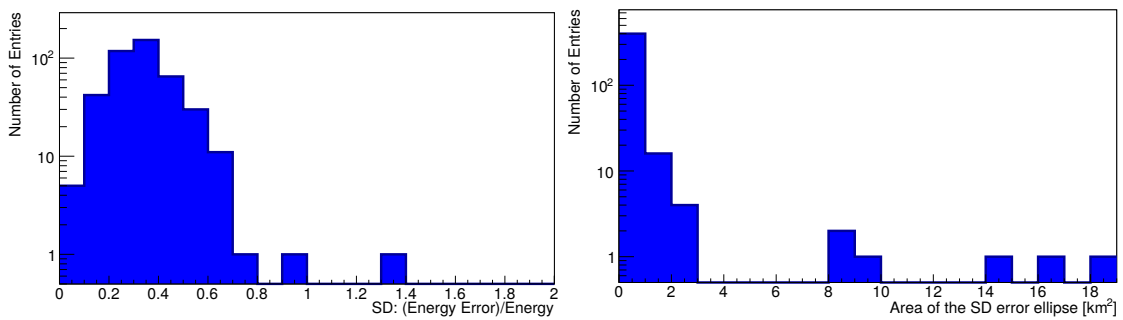


Figure 6.9.: On the left the relative uncertainty in SD energy is drawn. The mean value is 0.34. On the the right the area of the SD core uncertainty ellipse of the selected RdHASObserver events is drawn. The mean value of the area of the SD core uncertainty ellipse is 0.48 km². It has outliers at larger than 8 km².

The T3 trigger [97] processes the external triggers of AERA. It is optimized to reduce noise pulses. An event is only recorded if the distance of the SD core to the closest triggered AERA station is smaller than 5 km. This cut is too strict for horizontal air showers and can bias the recorded AERA data set, which can be seen in figure 6.10. It shows the distance to the closest AERA station to the SD core. The highest data point is at 4.4 km and events with distances larger than 5 km are not stored by the data acquisition. In the future this value should be adapted in order to unbiased the data acquisition regarding horizontal air showers recorded by AERA.

This is a proof for the large footprint of the radio signal and the first time radio showers with this large distance distance to the core are detected by a radio array.

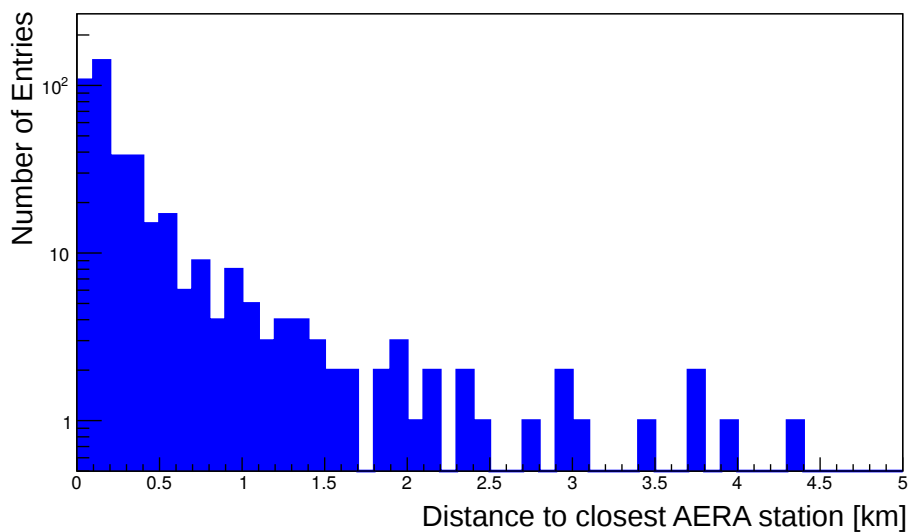


Figure 6.10.: Distance of the closest AERA station to the SD core. The maximal distance allowed by the AERA data acquisition is 5 km.

6.3. CoREAS Simulations

In course of this work CoREAS simulations were generated resembling the RdHA-SObserver reconstruction of measured data assuming once proton, once iron and twice electron neutrinos as primary particles of the extensive air showers. Due to the small cross section of neutrinos an interaction height for neutrinos has to be chosen in CORSIKA. The vertical interaction height has been fixed to 5 km and 12.345 km for the neutrino showers. The SD reconstruction of the measured RdHASObserver events is used to set the simulation parameters of the shower core, the direction and the energy. The simulated events are reconstructed with the

RdHASSimulationObserver in Offline. The sequence of reconstruction steps can be found in the appendix A.2. During the reconstruction the full AERA detector simulation is performed and realistic noise is added to the AERA trace. What happens if noise is added to a trace can be seen in figures 6.11 and 6.12.

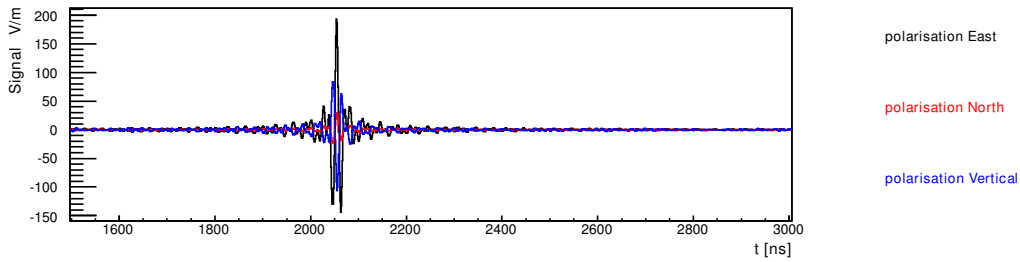


Figure 6.11.: AERA trace of a simulated event. No noise is added and the pulse can be seen at 2050 ns.

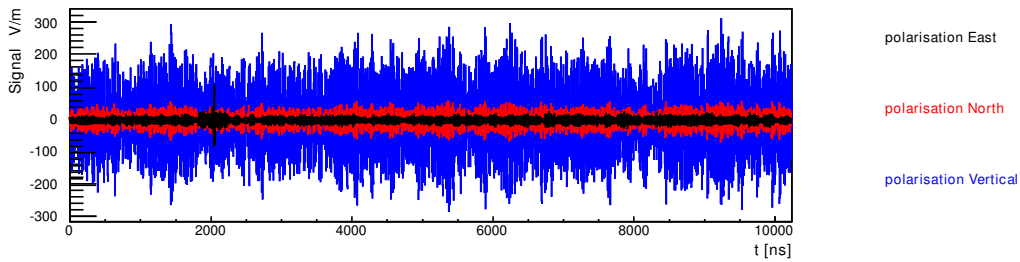


Figure 6.12.: AERA trace of the simulated event above with noise added. The pulse can still be seen at 2050 ns, but the peak position is harder to determine.

An overview of the reconstructed events can be found in table 6.3. Adding noise to a simulation reduces the number of reconstructed simulated events slightly, because not all of the AERA stations pass the SNR cut of 10 and if the required minimum of three stations is not fulfilled the simulated event is not reconstructed. The number of AERA stations is reduced in the reconstructed simulated event sample. This can be seen in the following multiplicity plots.

6. Reconstructed Data Sample and Data Selection

Simulations	proton	iron	neutrino: height 5 km w/o SD quality cuts	neutrino: height 12.345 km w/o SD quality cuts
w/o noise	427	427	466	866
w/ noise	415	415	409	840
w/ SD + w/o noise	83	127	177	59

Table 6.3.: Overview of the reconstructed simulated events. The SD reconstruction of the shower core, the direction and the energy of the measured RdHASObserver events is used as an input for the simulations.

The station multiplicity of the simulated proton showers without noise added to the simulation is shown in figure 6.13 and with noise added in figure 6.14. Adding noise and applying a cut on the SNR of 10 reduces the station multiplicity. The mean multiplicity of the simulated events with proton primary with noise added is higher than for data, because they are performed for an ideal detector where all existing stations participate in all events. For the measured data some stations were not working during data acquisition and therefore no data from these stations are available. In figure 6.15 the radio signal amplitude of each station is plotted against the SNR for all simulated events with proton primary with noise added. Note that the selection of antennas in the simulation is determined by the SNR and not by the predicted detection threshold of $\approx 2 \mu\text{V}/\text{m}/\text{MHz}$, which means $100 \mu\text{V}/\text{m}$ for AERA, predicted by simulations of radio showers with energies of about 10^{18} eV showers [51]. Some simulated events are not reconstructed after adding the SD reconstruction in the reconstruction pipeline, because the SD HAS simulation reconstruction does not reconstruct events with too low energy.

The energy threshold of full efficiency of the SD HAS reconstruction is 4×10^{18} eV. The simulated events which could not be reconstructed after adding the SD reconstruction have a Monte Carlo simulated energy below this value, which can be seen in figure 6.16.

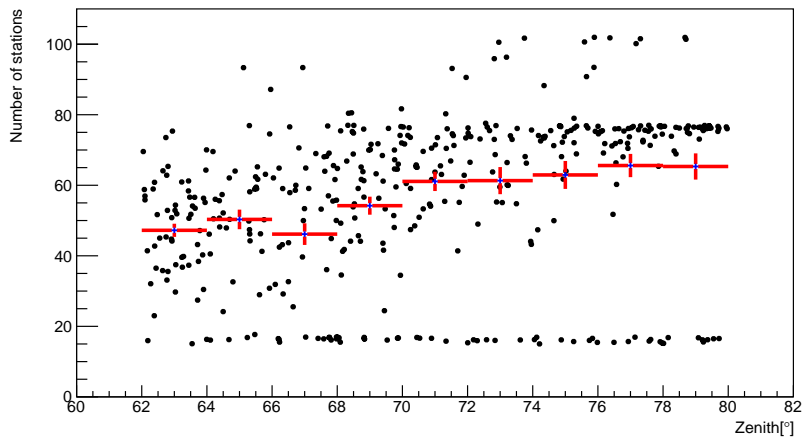


Figure 6.13.: Station multiplicity for simulated events with proton primary. No noise is added to the simulated events. The profile plot is drawn in red. In AERA-24 the maximal number of radio stations is 17. This explains the accumulation at around 15 stations. In AERA-124 the maximal number of radio stations is 77. This explains the second accumulation at around 75 stations. The dataset of AERA-153 used in this thesis covers only half a year of data taking with a lot of gaps in the uptime of AERA. The maximum of AERA stations is 102 for AERA-153. Therefore there are few data points with more than 80 stations. The remaining stations are self-triggered and have an alternative data acquisition and could not be merged with the externally triggered data at the time this thesis was written.

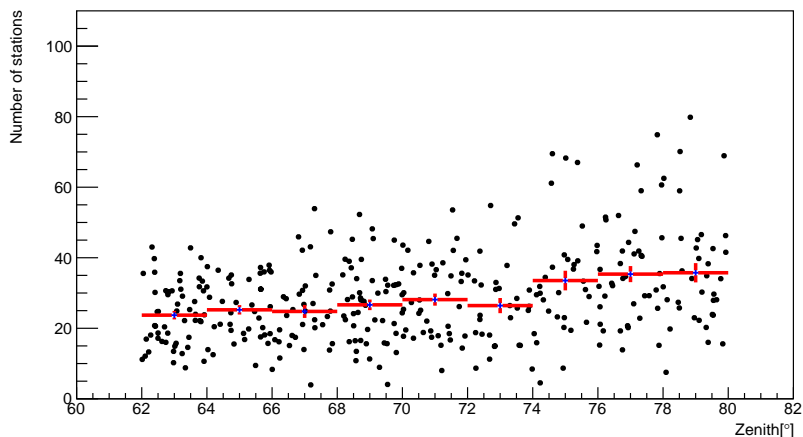


Figure 6.14.: Station multiplicity of simulated events with proton primary with noise added. The profile plot is drawn in red. The distribution resembles the distribution of the measured RdHASObserver events (see figure 6.8), but with higher mean multiplicity. In the simulations all existing stations were simulated, not only the ones functioning at the time the event was detected.

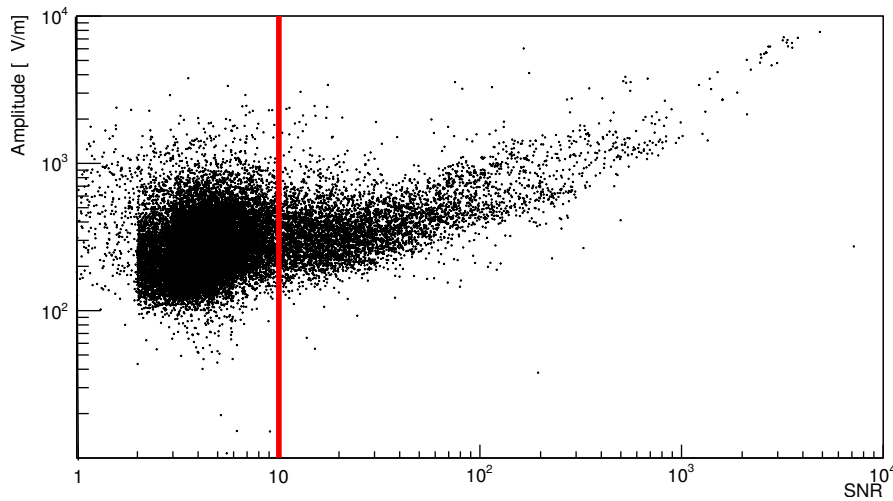


Figure 6.15.: SNR vs. amplitude of radio signal for simulated events with proton primaries. In red the SNR cut of 10 is drawn.

6.4. The Horizontal Polarisation Component

For the RdHASObserver reconstruction the magnitude of the north-south and east-west component of the electric field is used to determine the peak position of the radio pulse and the amplitude. The calculated horizontal component has large fluctuations due to the uncertainty of the antenna pattern for horizontal events and due to the higher noise background. In order to test if measuring the horizontal component of the electric field improves the reconstruction four prototype stations were built and installed on the AERA field in the course of this work. These are described in section 5.2.

The mean noise of the north-south, the east-west and the horizontal component of the selected RdHASObserver events are shown in figure 6.17. The mean of the mean noise of the east-west component is $35 \mu\text{V/m}$, of the north-south component is $32 \mu\text{V/m}$ and the horizontal component is $125 \mu\text{V/m}$. The horizontal component has outliers for some events. This shows that the calculated noise level in the horizontal component is really larger than in the north-south or east-west component. The selected measured RdHASObserver events and the simulated events with proton, iron and neutrino primaries will be used in the chapter 7 and 8.

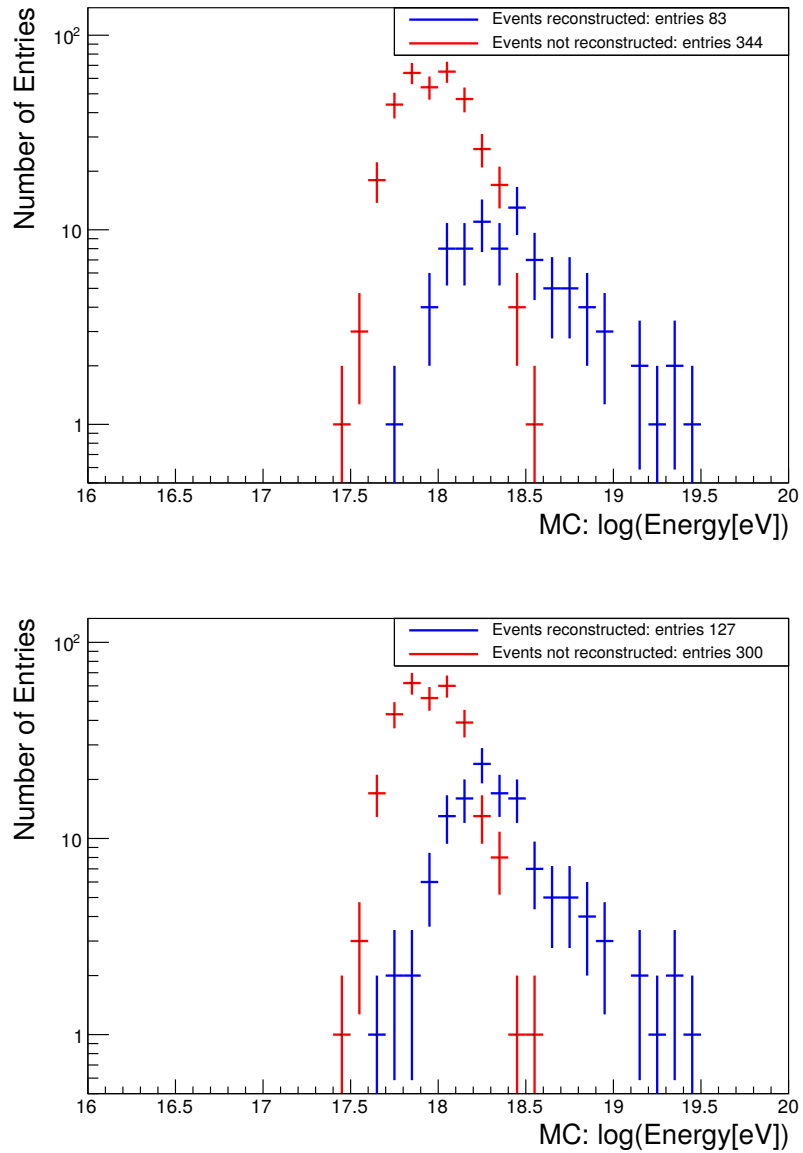


Figure 6.16.: Reconstruction of simulated events with proton (upper plot) and iron (lower plot) primaries. After adding the SD reconstruction 344 simulated events with proton primary and 300 simulated events with iron primary could not be reconstructed. These events have energies below the full efficiency energy for the SD HAS reconstruction.

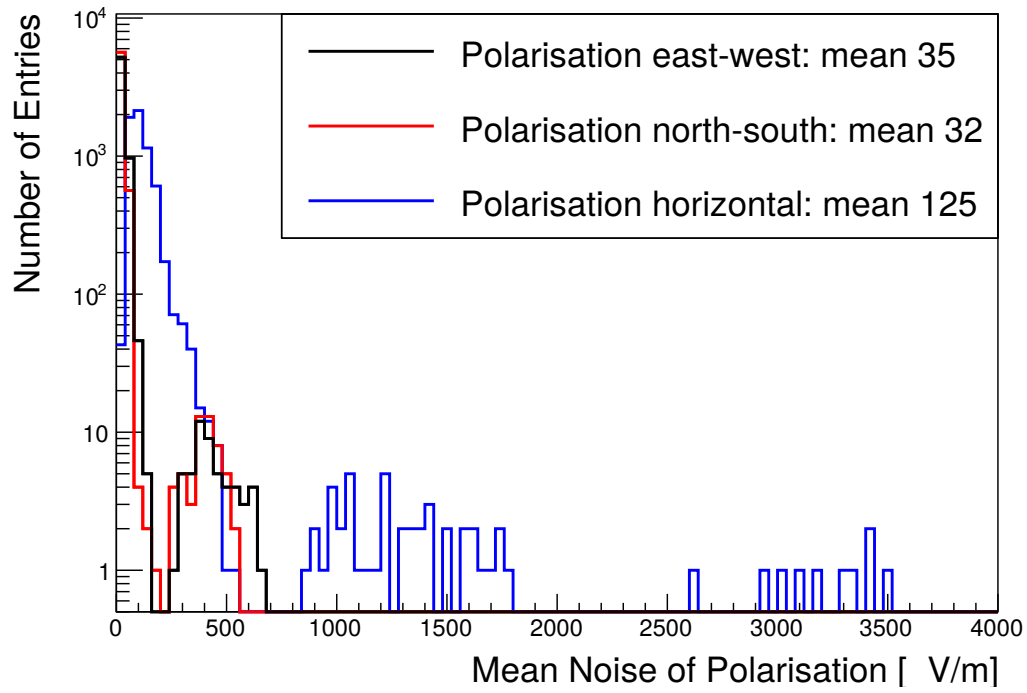


Figure 6.17.: Mean noise of the north-south, the east-west and the horizontal component of the electric field of the selected RdHASObserver events.

7. Analysis of Horizontal Air Showers Detected by AERA

The potential of horizontal air showers to contribute to the composition determination of cosmic rays due to the measurement of the electromagnetic component by radio has been discussed in section 2.4. The analysis of the AERA data sample (see chapter 6) and some particular characteristics of horizontal air showers will be described in this chapter. In the following sections the radio footprint of air showers, multi station events, high energy events, events with zenith angles larger than 80° , a comparison of measured and simulated radio amplitudes, the detection threshold for horizontal air showers, and AERA events measured at full efficiency of SD will be discussed.

7.1. Shower Footprint

In figure 2.11 footprints of simulated CoREAS showers with the same energy and azimuth angle but different zenith angles are shown. The energy of the simulated proton showers is 10^{18} eV. For the following consideration, from the data sample of the RdObserver four events with approximately the same energy and azimuth angle are selected. This will guarantee that the strength of the radio emission will only depend on the zenith angle and not on the energy or the azimuth angle. An overview of the four events is shown in table 7.1. Figure 7.1 shows the four events with increasing zenith angle. While the third and fourth event are not in the standard RdObserver data sample because of less than 55° zenith angle, these events are particularly interesting due to the high station multiplicity.

As can be seen, the number of stations increases with zenith angle and the lateral distribution function (LDF) gets more complex. The third and fourth event reveal that a second spatial dimension needs to be considered to describe the LDF with a fit function. The station multiplicity plots of the RdObserver (figure 6.3) and the RdHASObserver (figure 6.8) validate the same behaviour of increasing footprint with zenith angle.

	zenith angle [°]	azimuth angle [°]	energy [eV]	number of stations
1.	24.9	322.3	1.0×10^{18}	7
2.	40.5	313.5	8.2×10^{18}	11
3.	65.4	305.9	1.1×10^{18}	25
4.	75.3	309.3	2.5×10^{18}	51

Table 7.1.: Four RdObserver events selected with approximately the same energy around 10^{18} eV and azimuth angle of approximately 310° . The zenith angle increases from 24.9° to 75.3° , and so does the number of firing stations, from 7 to 51 stations.

The trigger cut of less than 5 km distance of the closest AERA station to the SD core limits the maximal distance to which air showers can be detected, like shown in figure 6.10. To increase the statistics for very high energy horizontal air showers detected by AERA it would be essential to increase this distance cut or make it zenith angle dependent. This proposal is currently discussed for a change of the trigger conditions of AERA.

7.2. Multi-Station Events

In this analysis, events with more than 50 AERA stations are called multi-station events. They allow a precise study of the shape of the radio LDF, because more data points are available. In the RdHASObserver dataset 21 multi-station events are contained. One example of such an event and the corresponding proton CoREAS simulation is shown in figure 7.2. The radio amplitudes obtained from the measured event and the simulation are of the same order and also the slope of the LDF shows good agreement between the CoREAS simulation and measured data. The maximal amplitude is approximately $800 \mu\text{V}/\text{m}$ for data and approximately $600 \mu\text{V}/\text{m}$ for the simulation. The shape of the LDF matches the simulated shower, except that in data there is a gap due to the five stations at the edge of the footprint not in operation during the measurement of this event. Surface plots of the radio amplitudes of the measured event and the corresponding proton CoREAS simulation are shown in figure 7.3. The colour scheme indicates the amplitude in $\mu\text{V}/\text{m}$ and the x -axis and y -axis are the coordinates on ground. The sharp fall off of the signal can be seen at the edge of the LDF and the valley, the Cherenkov cone is visible. The elliptical shape of the Cherenkov cone of the measured data can be reproduced with CoREAS simulations. The theoretical prediction of the horizontal LDF shape as shown in the theory introduction, especially in figure 2.12, can also be seen in measured data. This is a confirmation that CoREAS simulations are capable of reproducing the measured signal shape and amplitude of the radio emission of horizontal air showers.

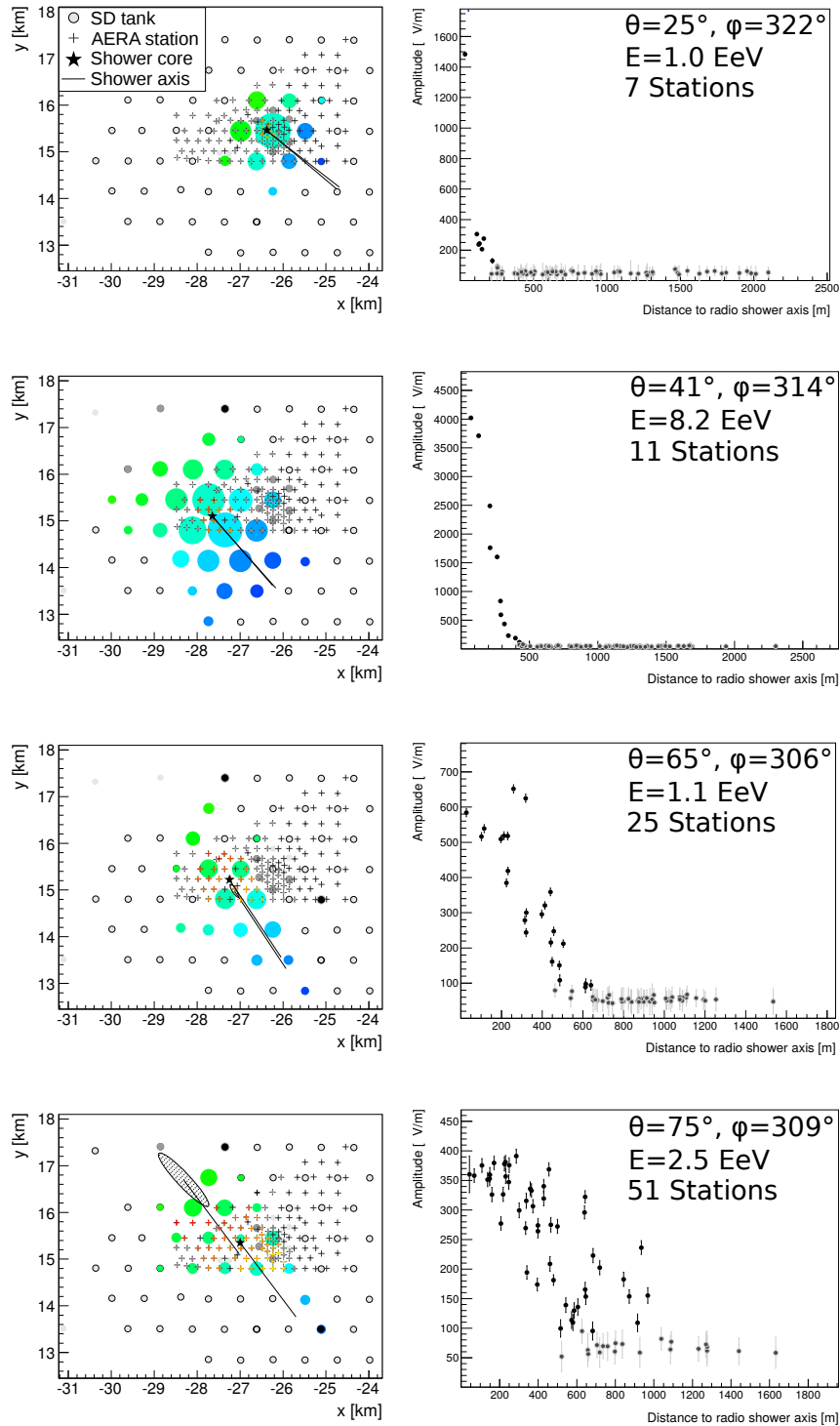


Figure 7.1.: Four events with characteristics described in table 7.1 with increasing zenith angle of the incoming shower from top to bottom. On the left the AERA array with the shower footprint and on the right the corresponding LDF is shown. The stations with signals above the SNR cut are drawn in black and the stations with signals below the SNR cut are drawn in grey.

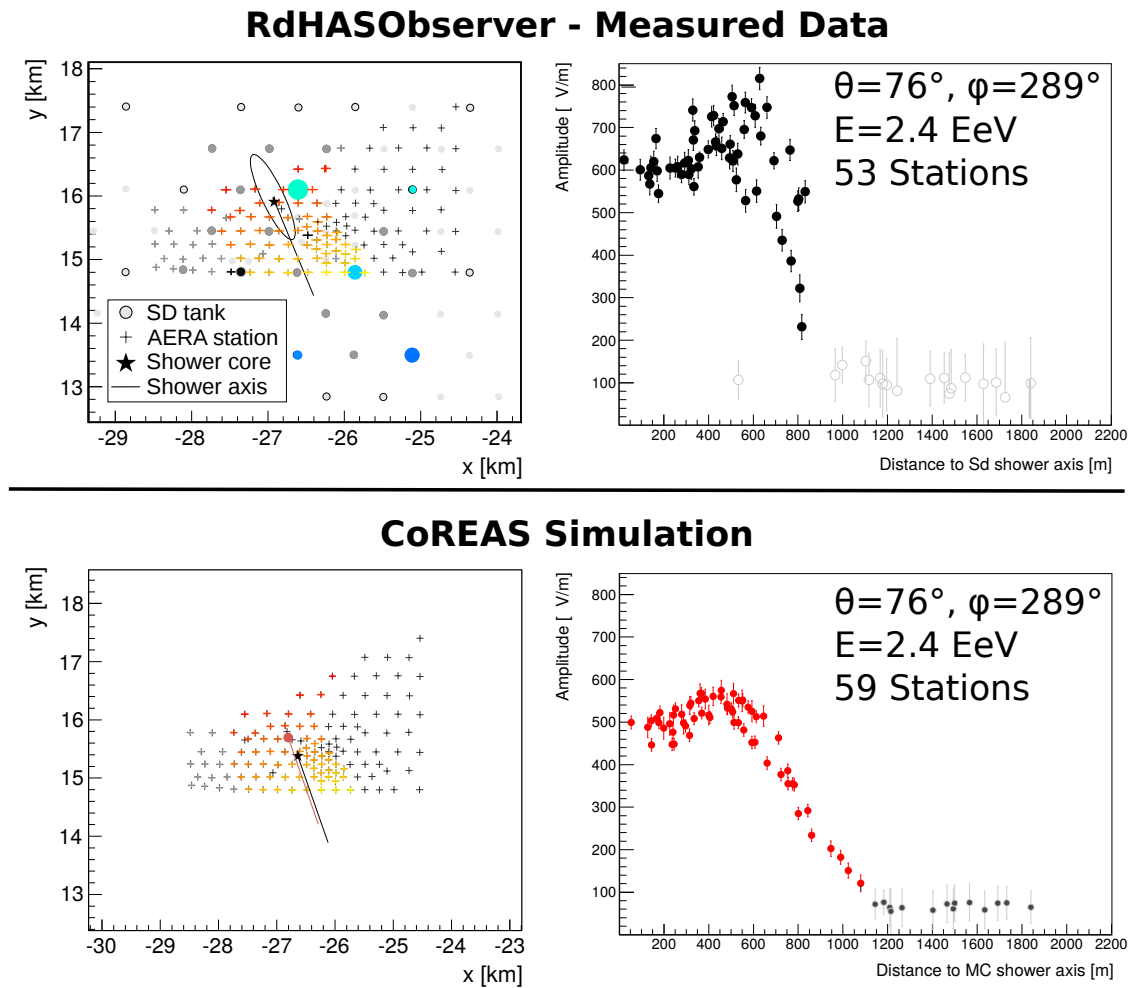
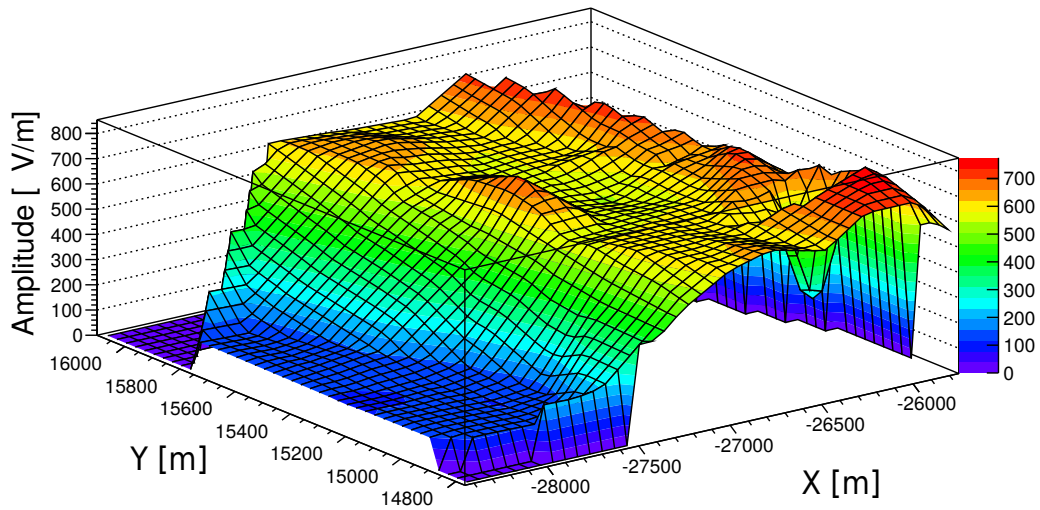


Figure 7.2.: In the upper part a measured event with 53 stations above the SNR cut, drawn in black in the LDF, is shown. The zenith angle is 76° and the energy is 2.4×10^{18} eV. The corresponding proton CoREAS simulation is shown in the lower part. For the simulation 59 stations above the SNR cut, drawn in red in the LDF, contribute to the LDF. The reconstruction of the simulation is performed without SD, so the SD tanks and the coloured circles, representing the signal measured by the tanks, are missing in the array plot. Five stations were not taking data during the measurement (black crosses in the array plot of the measured event) and one station is above the SNR cut in the simulation but not in the measured event. The CoREAS simulation is performed for an ideal AERA detector, where all the stations continuously take data.

RdHASObserver - Measured Data



CoREAS Simulation

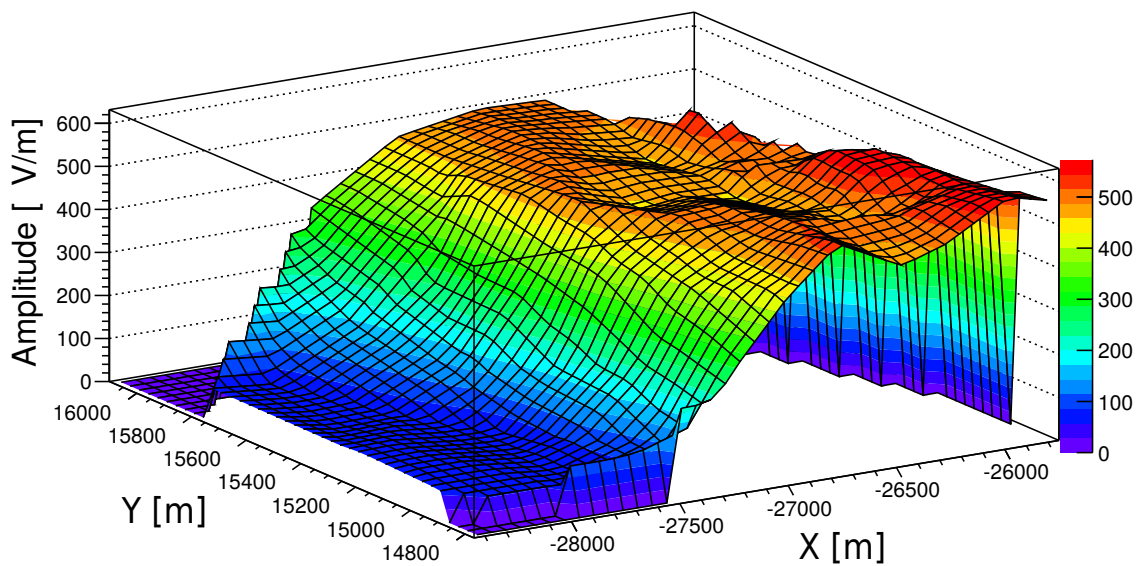


Figure 7.3.: Visualisation of the LDF of the measured event (upper plot) and the corresponding CoREAS simulation (lower plot) shown in figure 7.2. The colour scheme indicates the amplitude in $\mu\text{V}/\text{m}$ and the x -axis and y -axis are the coordinates on ground.

7.3. High-Energy Events

Events with energies greater than 10 EeV have high radio amplitudes and therefore the precision of the amplitude scale can be studied with high accuracy. Even if the core is not contained inside AERA, such events can still be detected and reconstructed. In the RdHASObserver dataset 17 events with energies greater than 10 EeV are contained. One example event is shown in figure 7.4.

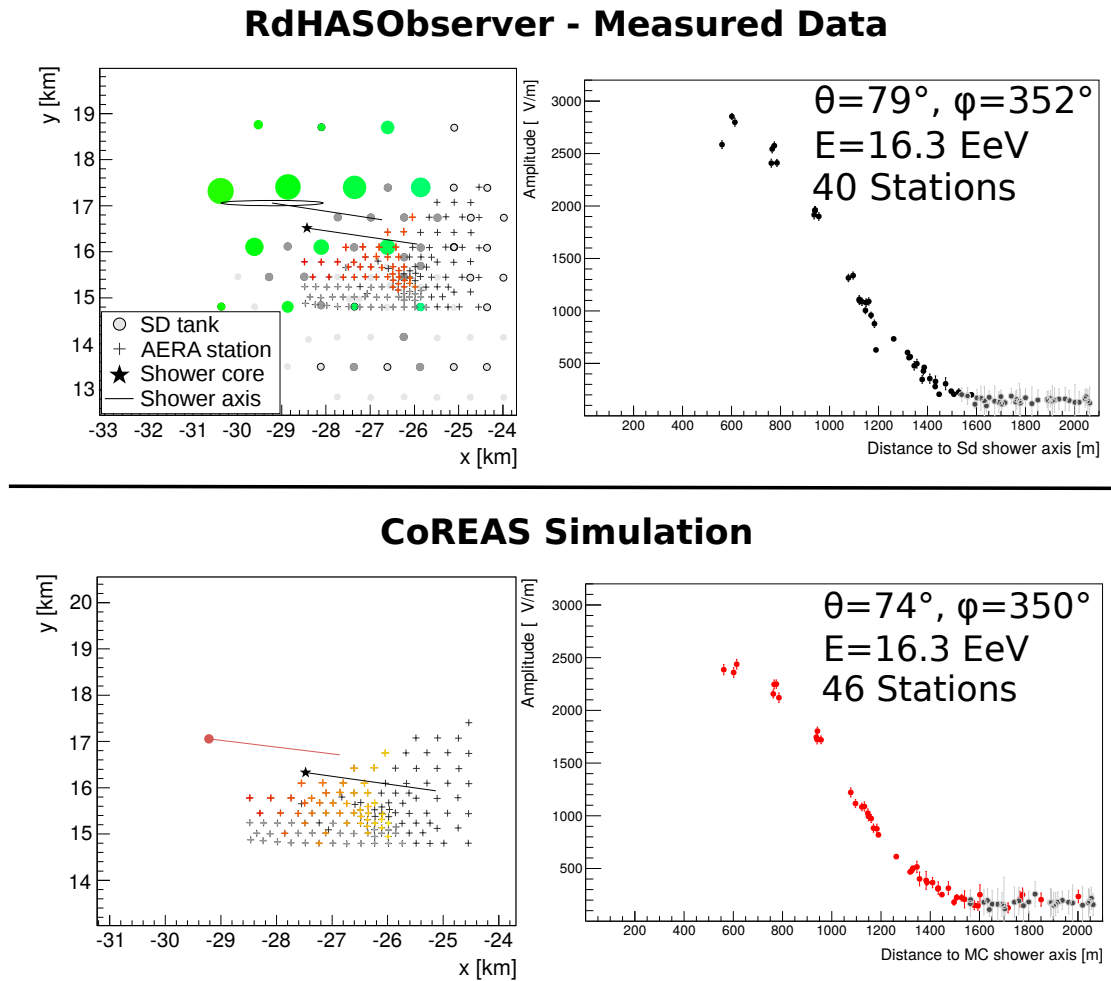


Figure 7.4.: Event with primary energy of 16.3 EeV, zenith angle 76° , azimuth angle 352° and 40 stations with significant signal. In the lower part the corresponding proton CoREAS simulation is shown. Compared to data, six additional stations are above the SNR cut. These additional stations are in the tail of the LDF. The stations above SNR cut are drawn in the LDF in black for measured data and in red for the CoREAS simulation.

For the high-energy events the trigger cut of less than 5 km distance of the closest AERA station to the SD core will reduce the number of events. This is because the high amplitude makes it possible to detect events even if the distance between the SD core and the AERA array is large. The AERA event with the highest energy measured in AERA is a horizontal event with 31.4 EeV and zenith angle of 68° . The event shown in figure 7.5 has even an energy of 56.8 EeV, but a zenith angle of 83° , which is removed by the SD HAS reconstruction quality cut on zenith angle. Never before such a high-energy event with 83° zenith angle could be detected and reconstructed in such detail with particle detectors stations plus 17 radio stations.

7.4. Events with Zenith Angle Larger than 80°

In the RdHASObserver data sample the SD HAS quality cut on the zenith angle of less than 80° reduces the number of events by 93, which is 22% of the final sample. However, the radio detection becomes more efficient with increasing zenith angle and the events above 80° have the highest station multiplicity. AERA is the only radio experiment which can detect events with such large zenith angles in a hybrid detector mode. A valid energy and core determination is needed from SD to be able to include such events in physics analysis for AERA. An example event is shown in figure 7.5. This event was measured with AERA-153, so stations with up to 750 m distance between each other are included. Impressive are the measured high amplitudes of more than $6000 \mu\text{V}/\text{m}$. The lower sensitivity threshold for AERA is roughly $100 \mu\text{V}/\text{m}$. Unfortunately, only 17 stations above SNR cut are contained in the measurement. The other stations were not taking data at that moment. In the simulation 78 stations above the SNR cut contribute to the LDF. The amplitude and the shape of the LDF can be reproduced by CoREAS simulations. The noise added in the simulation arises only in the stations below SNR cut. The antenna stations with 750 m spacing are all contained in the simulation.

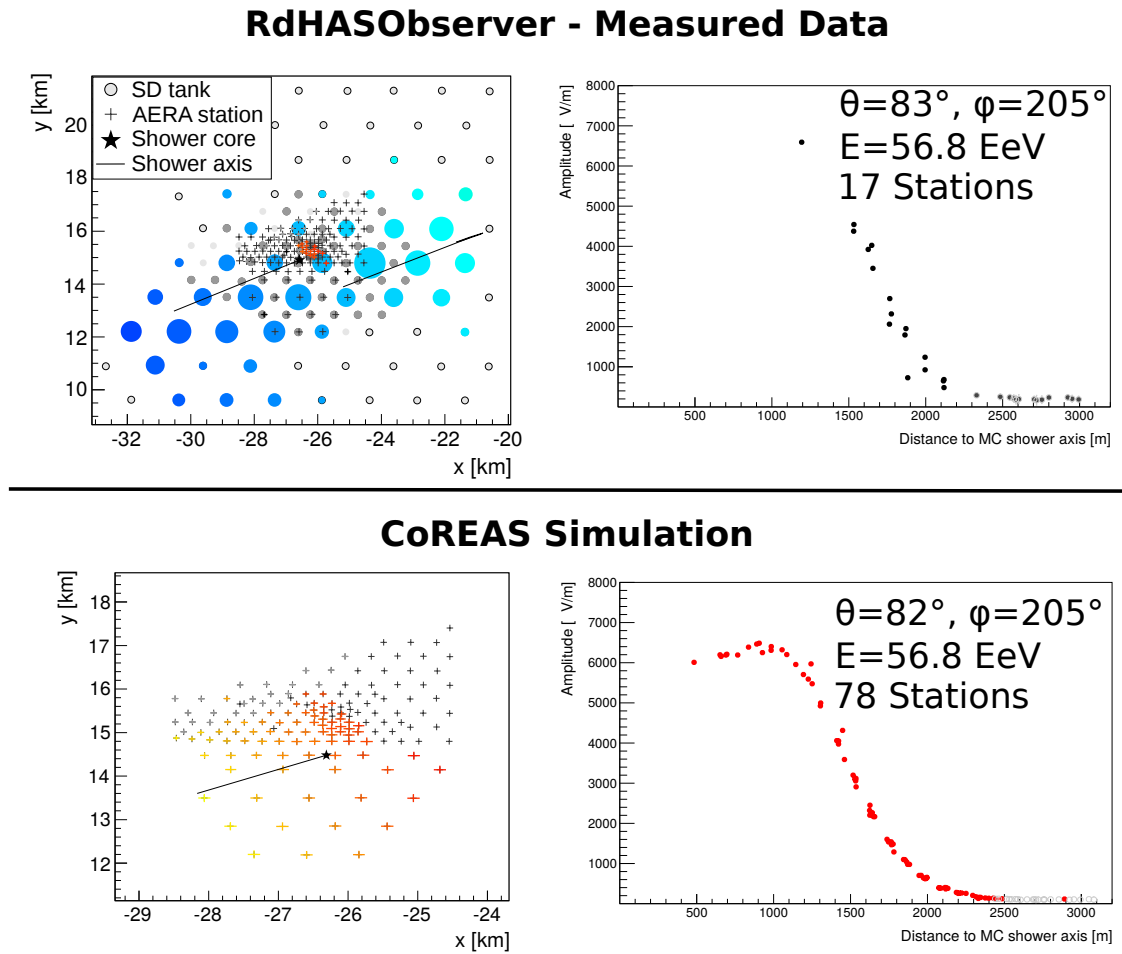


Figure 7.5.: Event with 56.8 EeV, zenith angle of 83° , azimuth angle of 205° with 17 stations included in the LDF (drawn in black) of the measured event. Amplitudes of larger than $6000 \mu\text{V/m}$ are measured due to the high energy of the shower. In the corresponding proton CoREAS simulation similar amplitudes are reconstructed. The LDF of the simulation contains 78 stations, drawn in red. All stations with 750 m distance are included. The stations in the upper right part of the array are self triggered and not sensitive to horizontal air showers. This event does not pass the SD HAS quality cut of less than 80° zenith angle.

7.5. Comparison of Measured and Simulated Amplitudes

To determine the energy of horizontal air showers it is essential to be able to reproduce the measured amplitudes in simulations. We have already seen in several examples that to first order this is the case. However, different sources of uncertainties have to be taken into account in the simulations like uncertainties on the core position, the energy, the primary mass, the shower maximum and the radio detector (antenna pattern, electric field conditions, etc.). This will be studied in more detail, exemplary in the following. All simulations are performed with CoREAS. Afterwards, the full AERA detector simulation is applied and realistic noise, extracted from data, is added. A description of the simulations is given in section 6.3.

7.5.1. Example Event with Core Shift

First, the amplitude dependence on the core position was investigated for the event of figure 7.6. The SD HAS reconstruction provides an uncertainty on the SD core estimation. According to this core estimation uncertainty, the core of the CoREAS simulations was shifted to the vertices of the SD core error ellipse. The simulations were performed with the initial reconstructed SD HAS energy. The four modified core positions and the initial core position are shown in figure 7.7. The corresponding LDFs are shown in red for proton primaries and in blue for iron primaries in figure 7.9. This shows that shifting the core to the vertices of the core error ellipse leaves the edge of the radio LDF almost unchanged. As a next step the core was shifted in x and y direction simultaneously, thus the SD core error ellipse of one σ is left. The core positions are shown in figure 7.8. The LDFs of the corresponding simulations are shown in red for proton primaries and in blue for iron primaries in figure 7.10. Again, the LDFs of the simulated events with proton and iron primaries have very similar shapes. The initial core estimation fits for the shown event and the discrepancies of the scale of the measured and simulated radio amplitude could not be resolved. The issue of shifting the core shifts the edge of the LDF, but not the scale of the amplitude. For reasons of long computation time this core shift analysis was not performed for all events, but it shows that wrongly reconstructed cores (which clearly can happen due to the low density and uniform distribution of the surviving muons in the particle component of HAS) from the SD reconstruction could be easily identified by measuring the radio LDF.

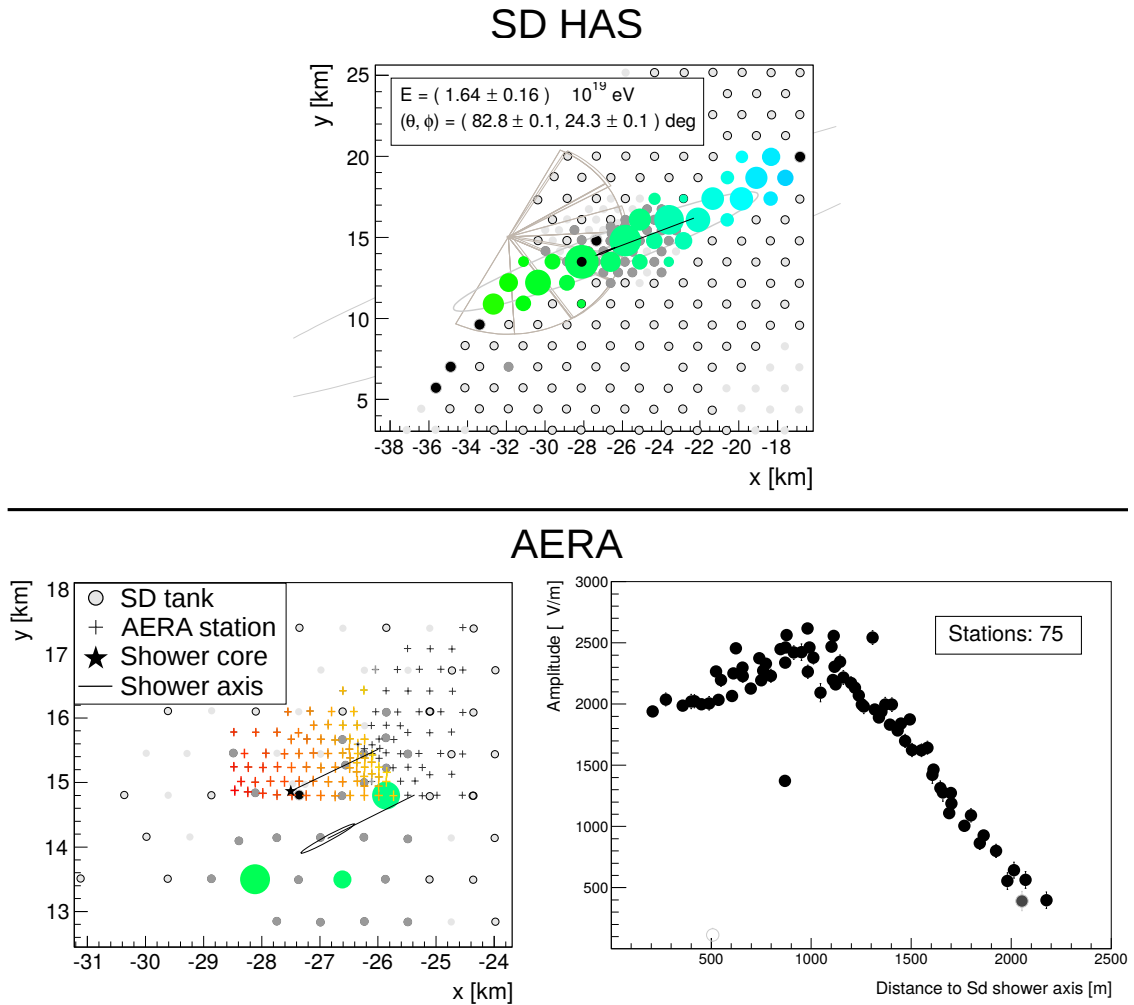


Figure 7.6.: Event example for core and energy shift. The upper part shows the SD array with the event and the reconstructed parameters of the SD HAS reconstruction. The energy of this event is $(1.64 \pm 0.16) \times 10^{19}$ eV and the zenith angle is 83° . The lower part shows the radio reconstruction with the AERA array, the radio LDF and the reconstructed RdHASObserver parameters. The number of AERA stations that participate in this event is 75. One AERA station is off the expected LDF shape. This station seems to be not working correctly, because it is not rejected and the following CoREAS simulations cannot reproduce the value. This event does not pass the standard SD HAS quality cut on the zenith angle of less than 80° .

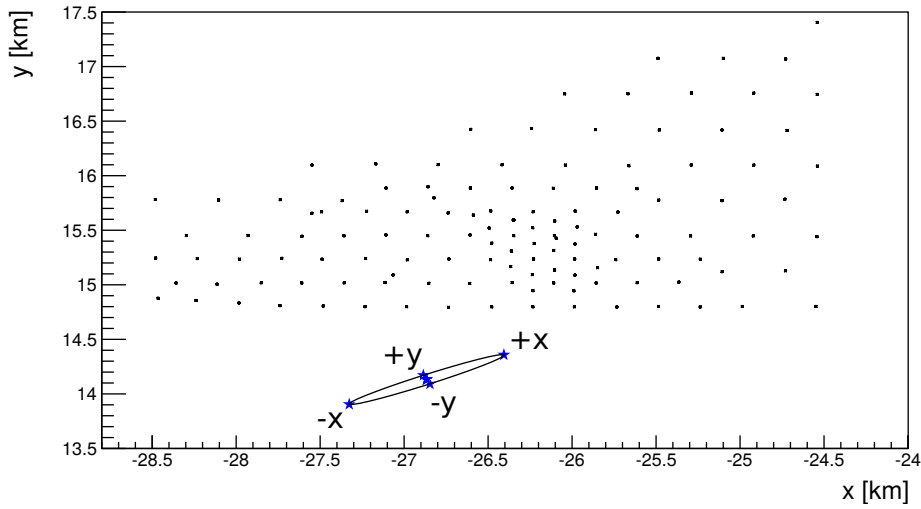


Figure 7.7.: Initial core position and four modified core positions in the vertices of the SD core uncertainty of one standard deviation. These positions are named as $\pm x$ and $\pm y$ and marked with blue stars. The corresponding LDFs are shown in figure 7.9.

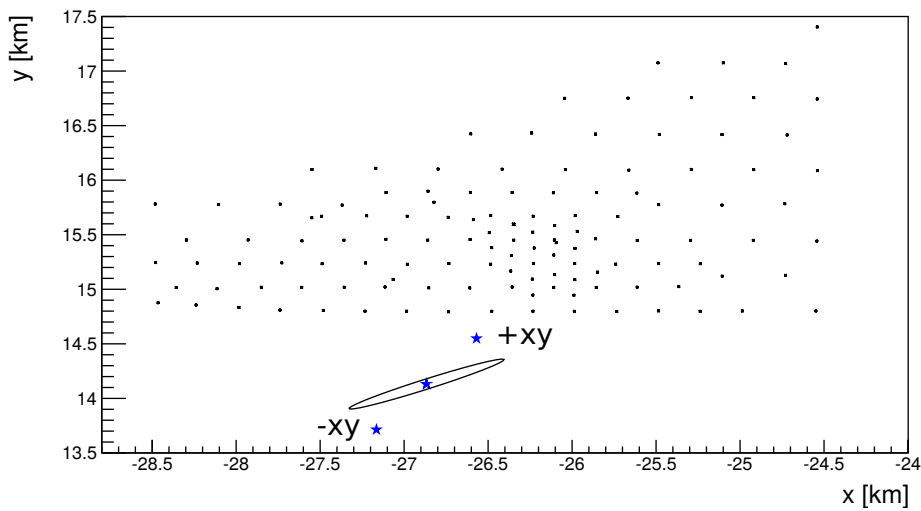


Figure 7.8.: Initial core position and two core positions outside of the SD core ellipse of one standard deviation. This positions are named as $\pm xy$ and marked with blue stars. The corresponding LDFs are shown in figure 7.10.

7. Analysis of Horizontal Air Showers Detected by AERA

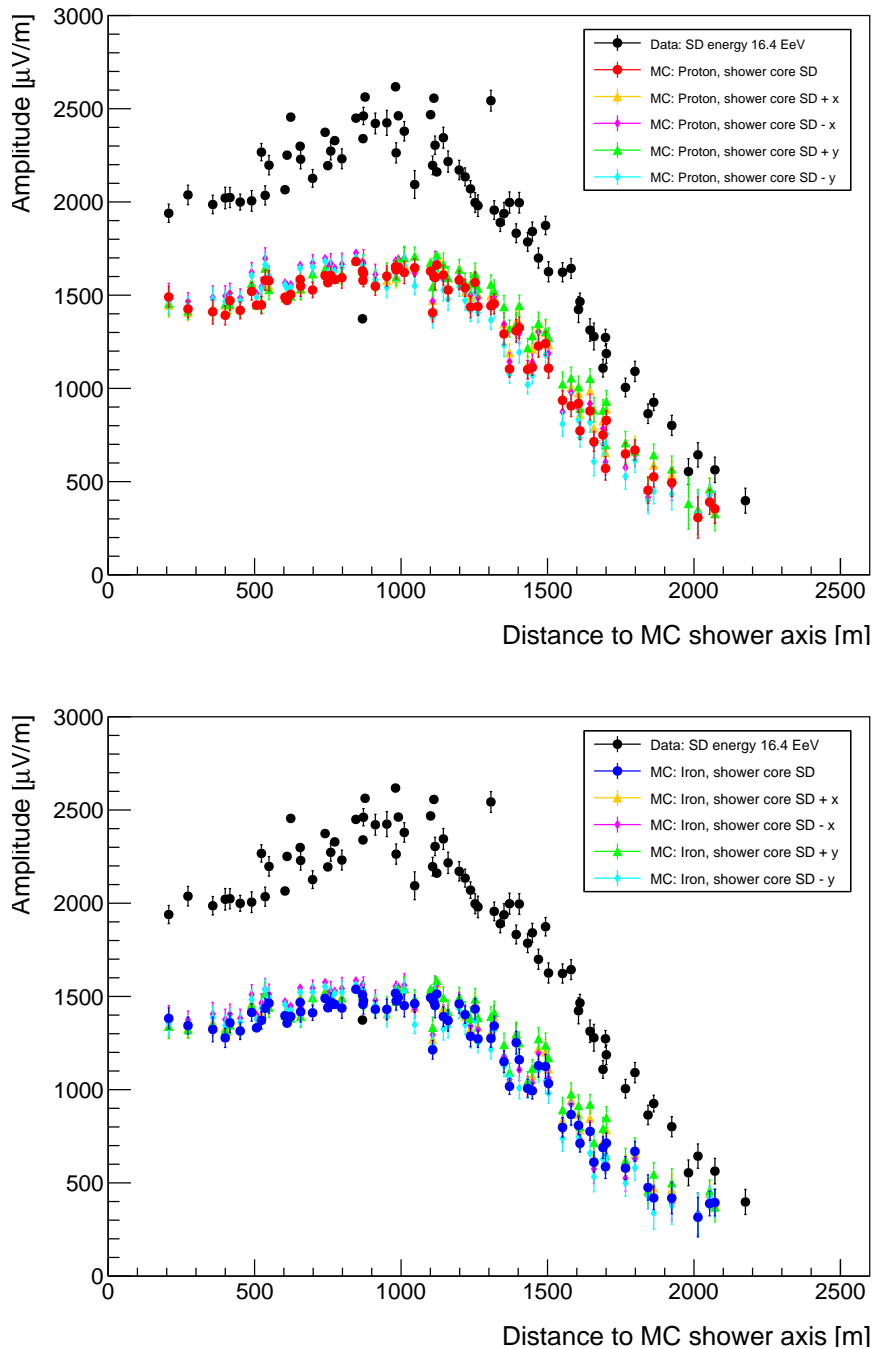


Figure 7.9.: The LDFs for the five simulated core positions and measured data. Measured data is drawn in black, the initial core position is drawn in red for proton primary in the upper plot and in blue for iron primary in the lower plot. The shift to the vertices of the core error ellipse are labelled with $\pm x$ and $\pm y$. The simulations of proton and iron primaries have the same shape within uncertainties and the shift to the vertices of the SD core error ellipse leaves the edge of the LDF almost unchanged.

7.5. Comparison of Measured and Simulated Amplitudes

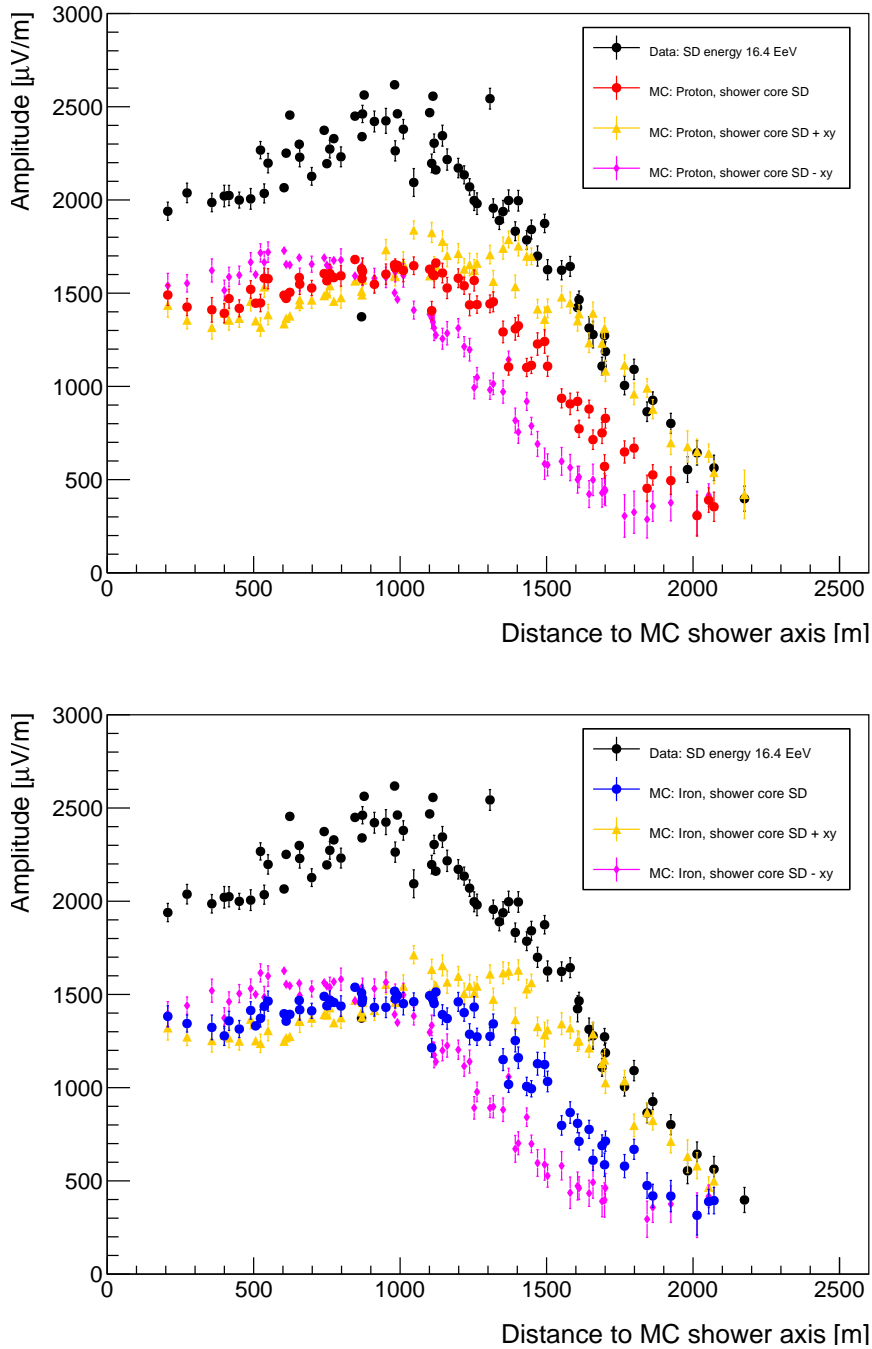


Figure 7.10.: The LDFs for the three simulated core positions and measured data. Measured data is drawn in black, the initial core position is drawn in red for the proton primary in the upper plot and in blue for the iron primary in the lower plot. The shift of the core is labelled with $\pm xy$. Shifting the SD core significantly with a shift larger than the SD core error ellipse, shifts the edge of the LDF. The simulations of proton and iron primaries have the similar shapes within uncertainties.

7.5.2. Example Events with Energy Shift

As a second step the effect of the true primary simulation energy on the simulated shower was analysed. Therefore, for three measured events simulations were performed with the simulated energy in $[E - 10 \cdot \sigma_E, E - 9 \cdot \sigma_E, \dots, E + 10 \cdot \sigma_E]$ with the reconstructed SD energy E and its uncertainty σ_E .

The event display of the event is shown in figure 7.6. The energy of this event is $(1.64 \pm 0.16) \times 10^{19}$ eV, the zenith angle is 83° and the station multiplicity is 75. It is measured with AERA-124 and it is interesting that high amplitudes can be measured at AERA stations up to a distance of 2 km from the shower axis. Figure 7.11 shows the simulated AERA LDFs for proton (upper part) and iron (lower part) primaries. The primary energy is varied in steps of σ_E of the SD reconstructed energy in the simulations. Proton and iron have a similar LDFs. This means it would be difficult to determine the composition of cosmic rays by the shape of the LDF. Increasing the primary energy increases the AERA amplitude. The LDF of the measured event is best described by the CoREAS simulation with an energy of $E + 4 \cdot \sigma_E$ for proton and $E + 5 \cdot \sigma_E$ for iron. This was determined by a χ^2 test. $E + 0 \cdot \sigma_E$ is excluded by the AERA LDF, if this is the only effect shifting the amplitude up and down.

The second event has an energy of $(1.94 \pm 0.51) \times 10^{18}$ eV, zenith angle of 76° and station multiplicity of 51. It is also measured with AERA-124. The event display can be seen in figure 7.12. This event was also detected by FD. The variation of primary energies in simulations are shown in figure 7.13 for proton and iron primaries. The slope of the LDF is not well described by the simulated events with proton and iron primaries. This gives an indication that the core position determined by SD is not sufficient to reproduce the measured amplitudes in simulated events for AERA. The measured event is best described by a CoREAS simulation with an energy of $E + 6 \cdot \sigma_E$ for proton and iron. This was determined by a χ^2 test.

The third example shows an event where the core is far outside of the AERA array and the SD Infill. Nonetheless, AERA measures high amplitudes. Figure 7.14 shows the event display. The event is also measured with AERA-124. The energy of this event is $(1.22 \pm 0.38) \times 10^{18}$ eV, the zenith angle is 80° and the station multiplicity is 16. Figure 7.15 shows the variation of energies in simulations for protons and iron. The measured event is best described by CoREAS simulations with an energy of $E + 9 \cdot \sigma_E$ for proton and $E + 7 \cdot \sigma_E$ for iron. This was determined by a χ^2 test.

7.5. Comparison of Measured and Simulated Amplitudes

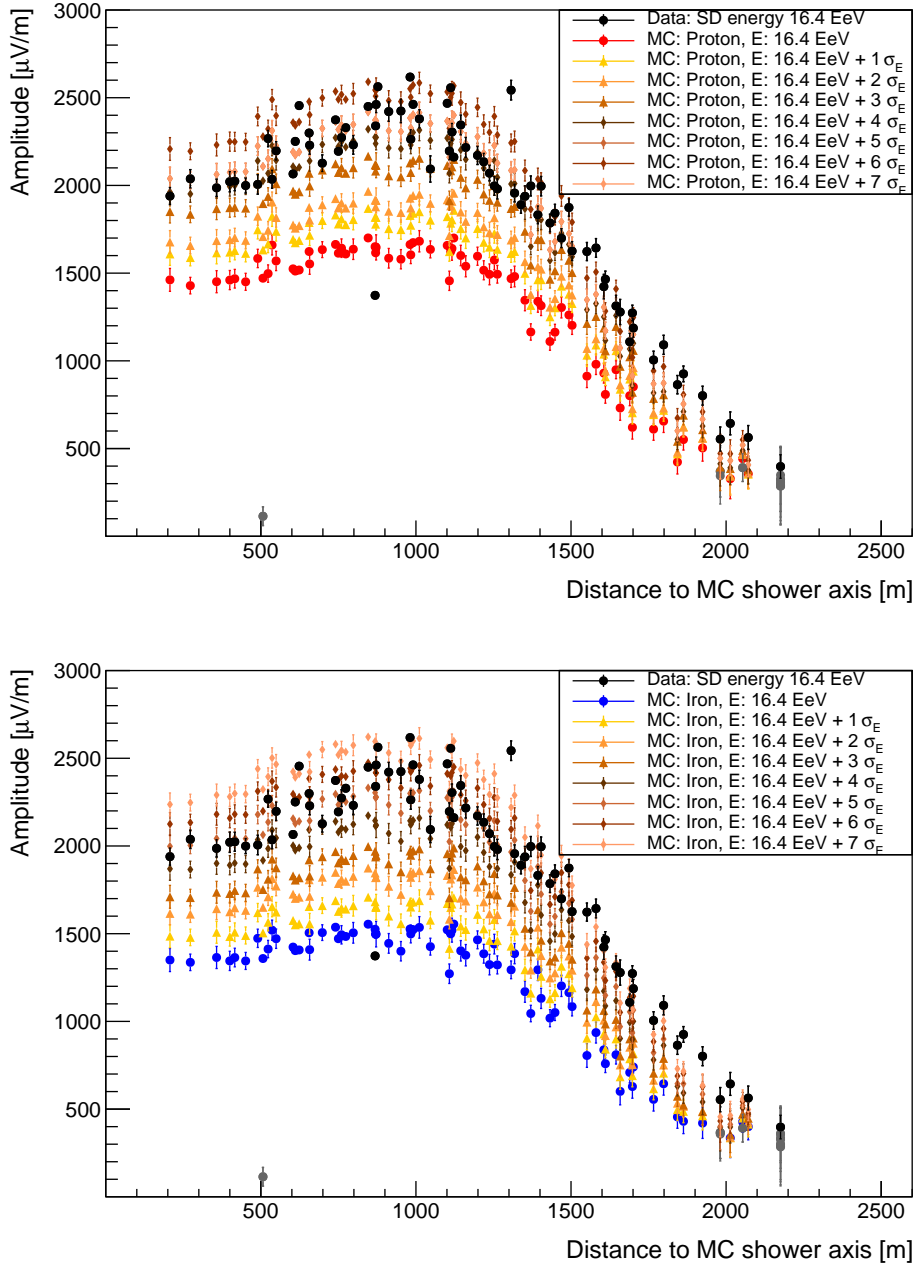


Figure 7.11.: Event example shown in figure 7.6 with varying simulated energies of the primary particle. The zenith angle is 83° . On top proton simulations and on the bottom iron simulations are shown. Measured data is drawn in black. The simulations with the reconstructed SD energies are drawn in red for proton and in blue for iron primaries. Realistic noise, extracted from measured data, is added to the simulations. The measured data is best described by a CoREAS simulation with an energy of $E + 4 \cdot \sigma_E$ for proton and $E + 5 \cdot \sigma_E$ for iron.

7. Analysis of Horizontal Air Showers Detected by AERA

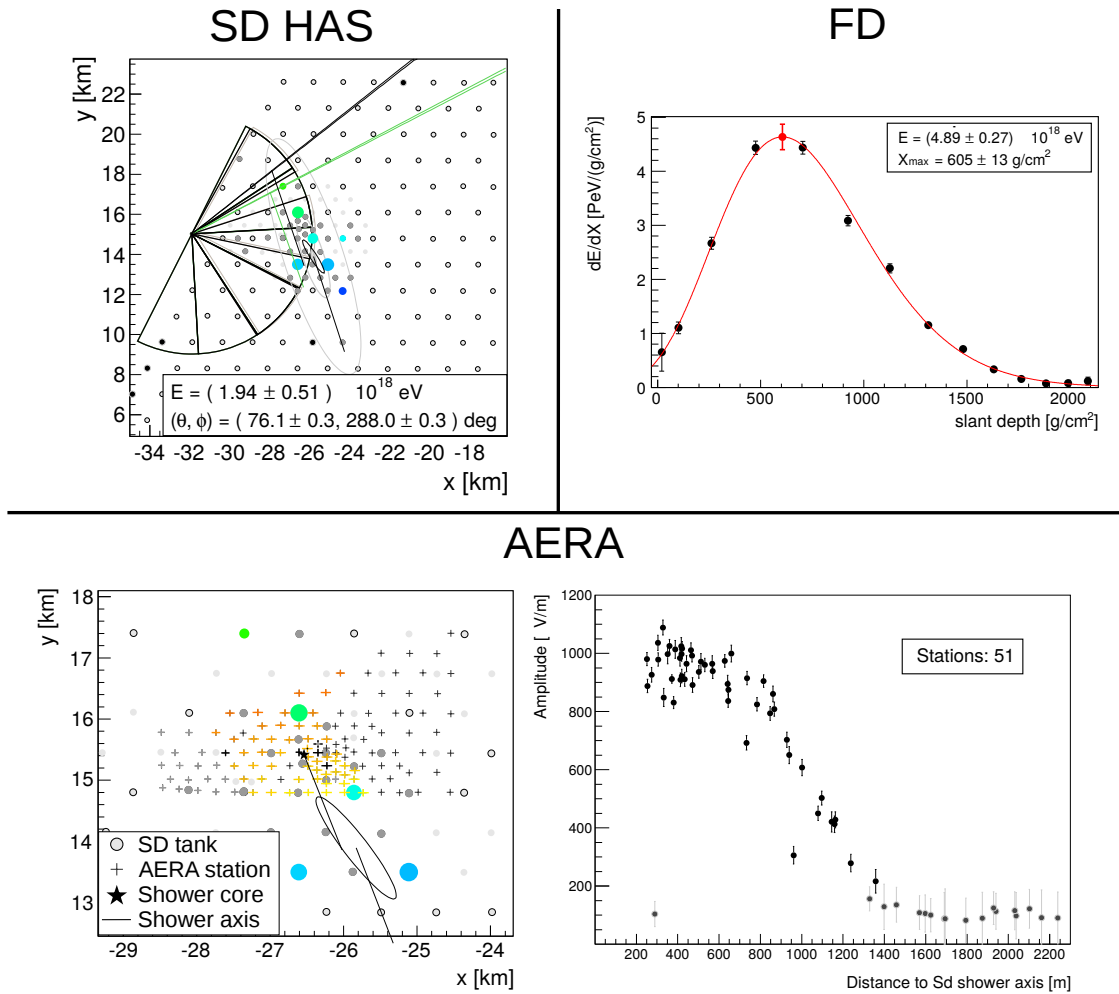


Figure 7.12.: Second example event. The upper left part shows the SD array and the reconstructed parameters of the SD HAS reconstruction. The energy of this event is $(1.94 \pm 0.51) \times 10^{18}$ eV and the zenith angle is 76° . The upper right part shows the FD longitudinal profile with the reconstructed parameters by FD. The lower part shows the radio reconstruction with the AERA array, the radio LDF and the reconstructed parameters by the RdHASObserver.

7.5. Comparison of Measured and Simulated Amplitudes

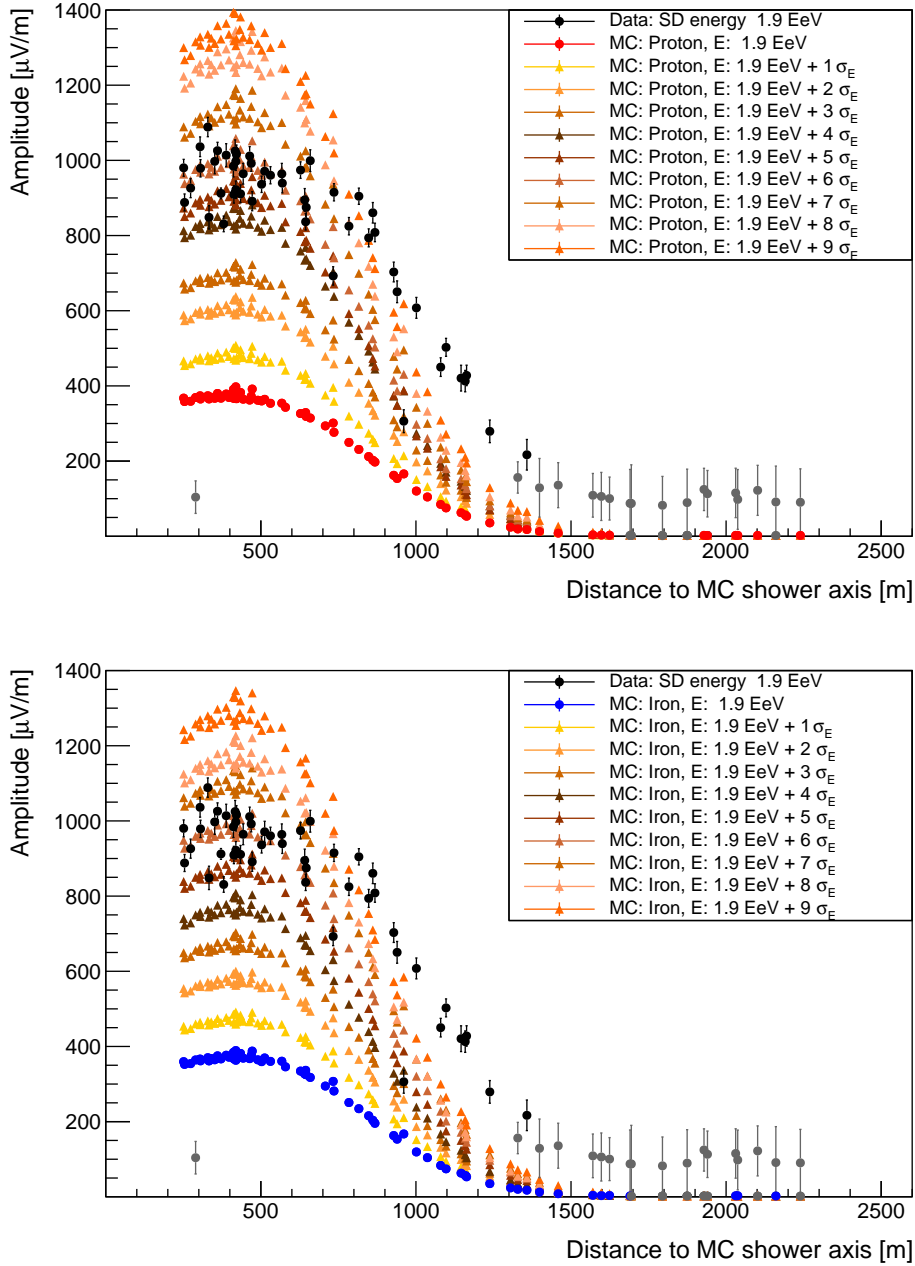


Figure 7.13.: Second example event with varying simulated energies of the primary particle. Proton simulations are shown on top and iron simulations on the bottom. For clarity reasons no noise was added to the simulations. Measured data is drawn in black. The simulations with the reconstructed energies are drawn in red for proton and in blue for iron primaries. The edge of the measured LDF is not well described by the simulation. The reason for this is the larger uncertainty on the SD core, which can be seen in figure 7.12. The measured data is best described by a CoREAS simulation with an energy of $E + 6 \cdot \sigma_E$ for proton and iron.

7. Analysis of Horizontal Air Showers Detected by AERA

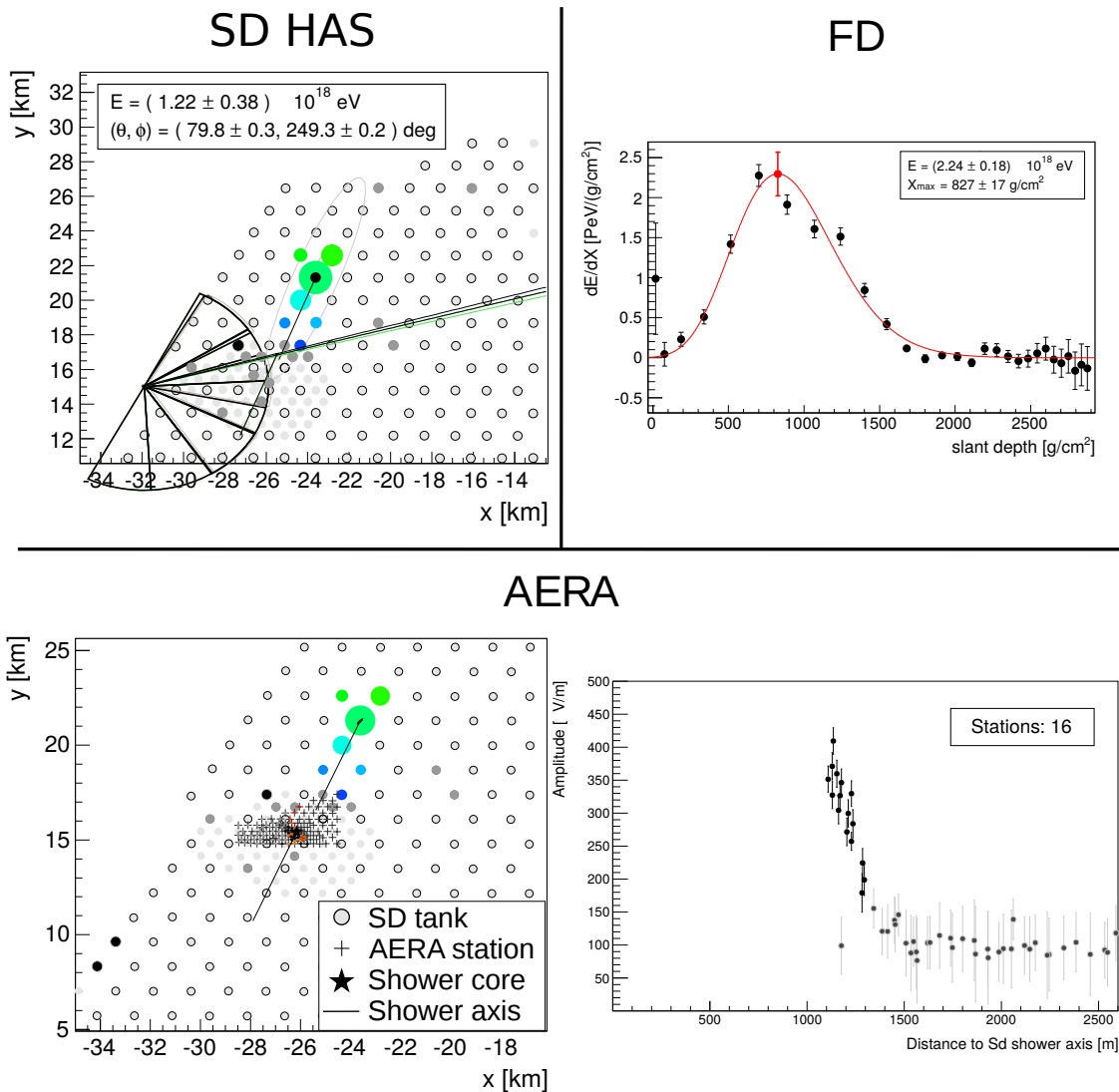


Figure 7.14.: Third example event. The upper left part shows the SD array and the reconstructed parameters of the SD HAS reconstruction. The energy of this event is $(1.22 \pm 0.38) \times 10^{18}$ eV and the zenith angle is 80° . The upper right part shows the FD longitudinal profile with the reconstructed parameters by FD. The lower part shows the radio reconstruction with the AERA array, the radio LDF and the reconstructed parameters by the RdHASObserver.

7.5. Comparison of Measured and Simulated Amplitudes

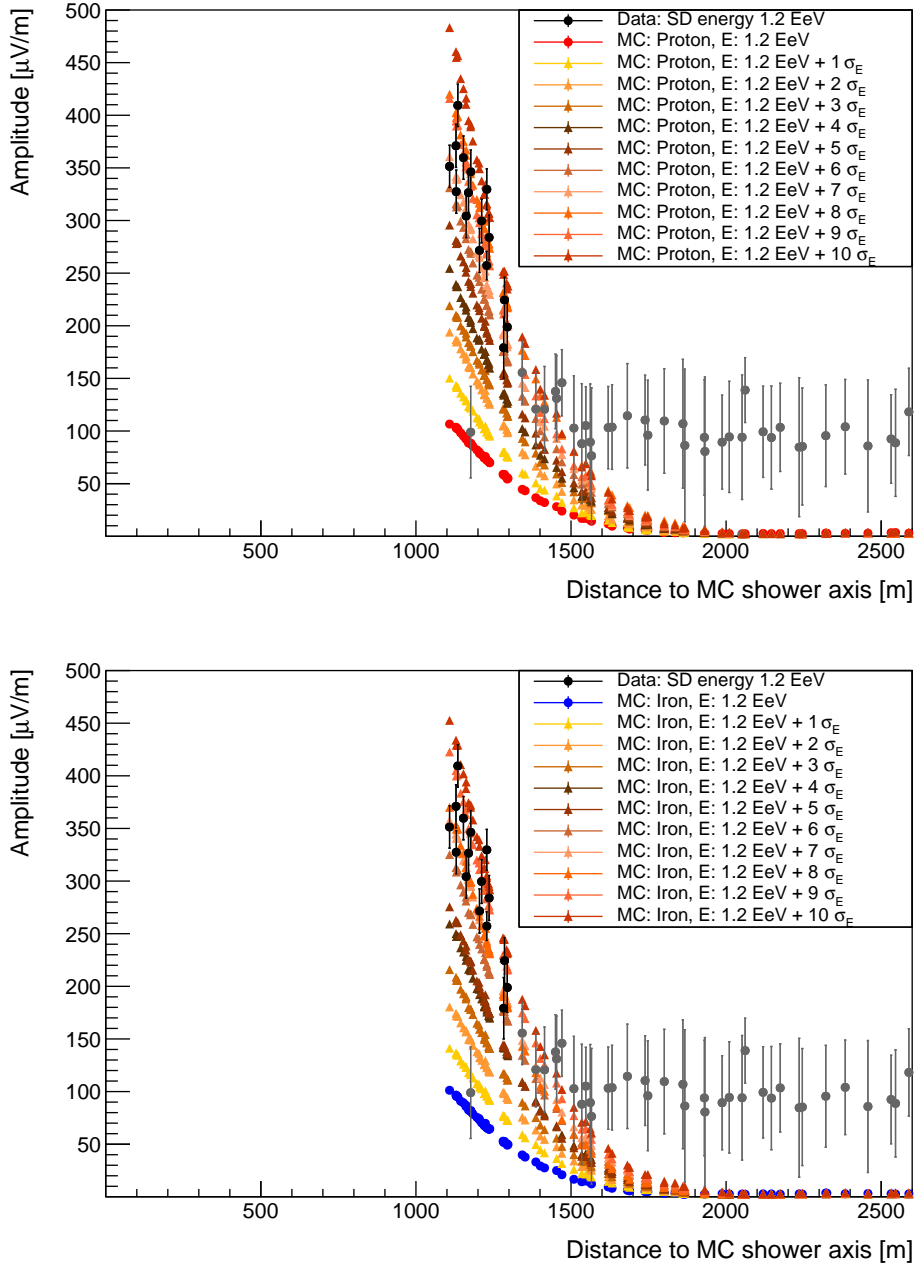


Figure 7.15.: Third example with varying simulated energies of the primary particle. Proton simulations are shown on top and iron simulations are shown on the bottom. For clarity reasons no noise was added to the simulations. The measured data is drawn in black. The simulations with the reconstructed energies are drawn in red for proton and in blue for iron. Measured data is best described for proton primaries by a CoREAS simulation with an energy of $E + 9 \cdot \sigma_E$ and for iron primaries with an energy of $E + 7 \cdot \sigma_E$. The SD core of the event is far outside AERA. Therefore, the first entry of the LDF is at 1100 m distance to the SD shower axis.

The three events show a discrepancy of 4 to 7 σ between the energy reconstructed by SD and the primary energy needed to reproduce the measured LDF by AERA. Whether there is a general systematic shift in measured and simulated radio amplitude is going to be shown in the following for the full RdHASObserver data sample. The amplitudes of the measured and simulated events are checked on a bias on the composition, the zenith angle, the energy, the core position relative to AERA and the antenna type. The idea is to clarify whether the energy determined by SD is too low, because fewer muons are measured by the SD tanks for horizontal air showers and are then missing in the simulations.

The SD energy estimator N19 is obtained by fitting a reference profile of the muon density to the recorded spatial pattern of SD signals [45]. This N19 parameter is then calibrated with FD measurements [47]. The determination of N19 is dependent on the hadronic model, because it is dependent on the number of muons. A correction factor of typically 20% is applied to N19 [98], because the electromagnetic component is not seen by SD for horizontal air showers. Radio measurements can provide an independent determination of the electromagnetic component and validate the correction factor for SD. In section 8.1 the radio energy estimator for horizontal air shower will be introduced. The energy determined by AERA can then be cross-checked with the energy determined by FD for the events detected by AERA, SD and FD. This will provide the possibility to examine the energy calibration of SD and FD.

Nevertheless, the observation of a disagreement of the amplitudes for all those high-energy, multi-station events is interesting and needs to be studied in more detail in the future.

7.5.3. Shower Composition

An important question is whether proton and iron induced horizontal air showers can be distinguished. This would show that horizontal air showers are sensitive to the composition of cosmic rays. To check whether assuming proton or iron primaries shows a bias in the simulated amplitudes the CoREAS simulations are compared to the measured RdHASObserver events. The comparison of measured and simulated amplitudes is shown for proton primaries in the upper plot of figure 7.16 and for iron primaries in the upper plot of figure 7.17. Each data point represents the amplitude given by one AERA station. Only stations above the SNR cut of 10 are considered. The relative difference is shown in the figures on the lower plots. The mean relative difference is a measure of the reconstruction bias and the RMS is a measure of the uncertainty of the variable. A relative difference compatible with zero would show that the data sample is unbiased from measured and simulated amplitude.

7.5. Comparison of Measured and Simulated Amplitudes

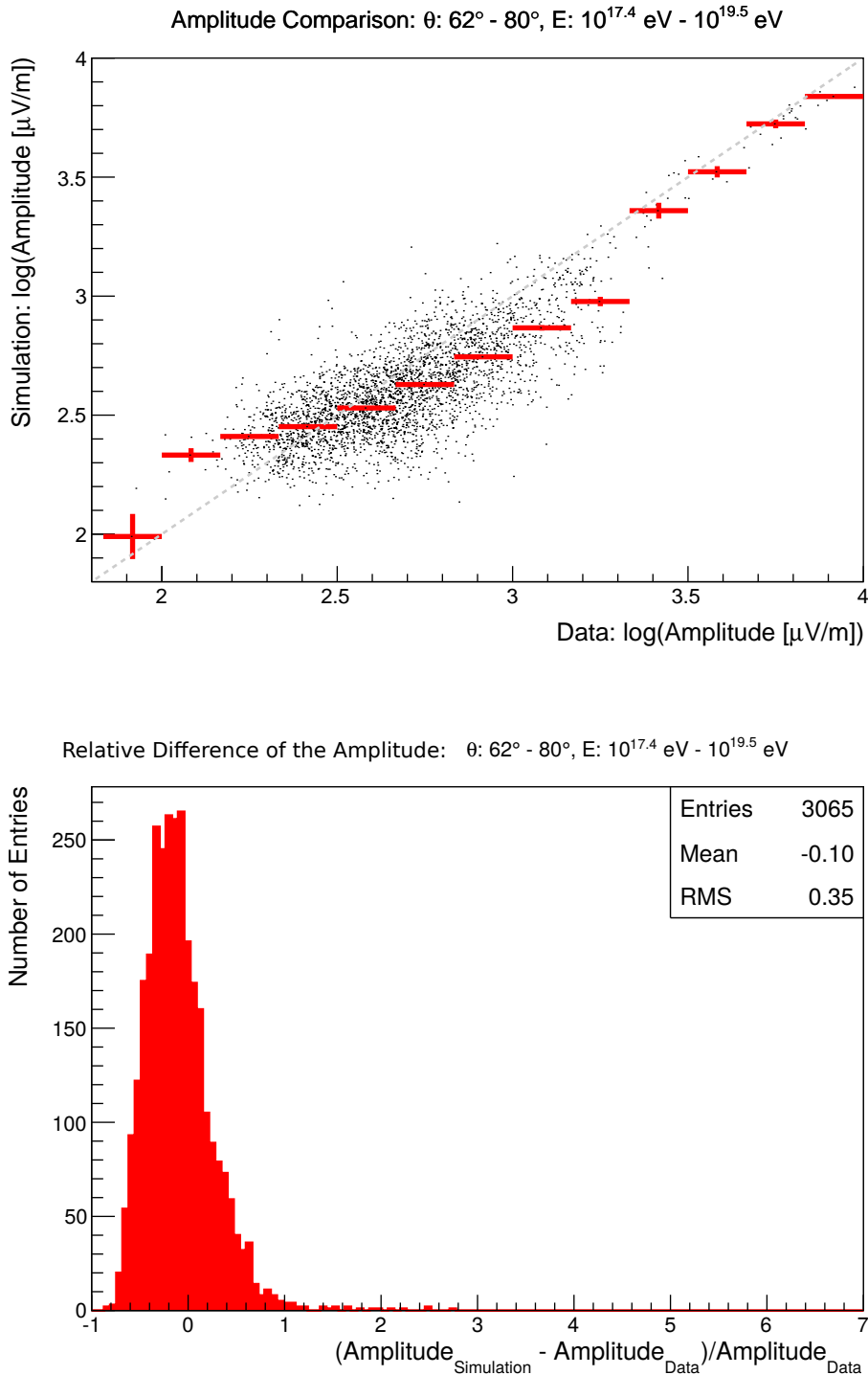


Figure 7.16.: A comparison of measured and simulated amplitude for proton primaries is shown in the upper plot. Each data point represents the amplitude given by one AERA station. In red the profile plot is drawn. The relative difference is shown in the lower plot.

7. Analysis of Horizontal Air Showers Detected by AERA

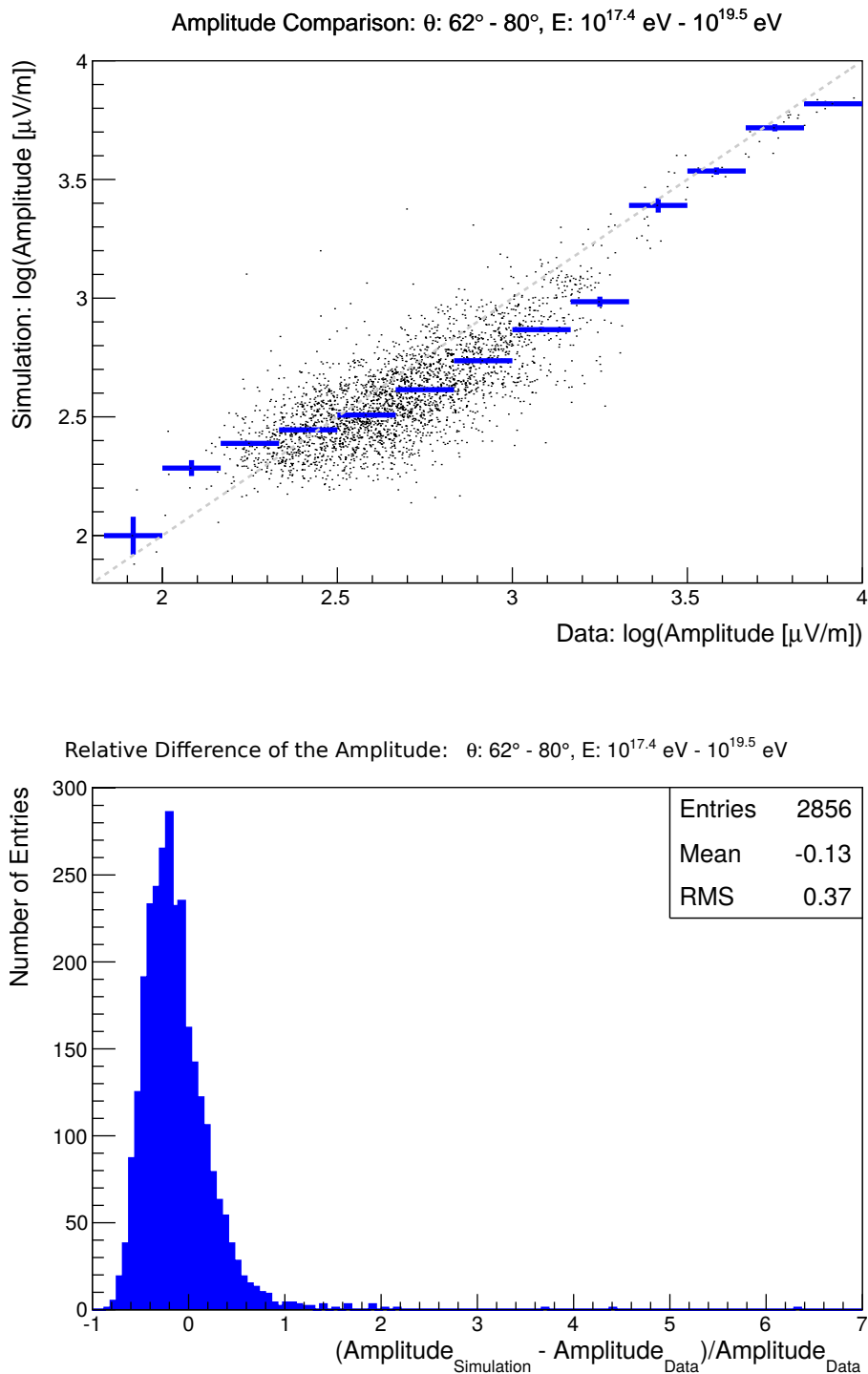


Figure 7.17.: A comparison of measured and simulated amplitude for iron primaries is shown in the upper plot. Each data point represents the amplitude given by one AERA station. In blue the profile plot is drawn. The relative difference is shown in the lower plot.

A significant systematic shift of measured and simulated amplitudes neither not be seen for proton nor for iron primaries. The mean value of the relative difference is -0.10 for proton primaries and -0.13 for iron primaries. The mean relative difference between measured and simulated events are of the same order and have the same sign.

The relative difference is bigger for iron than for proton primaries, but the distribution of the relative uncertainties is also broader. This could be a hint to a mixed composition. The mean relative difference of proton and iron primaries differ with a significance of 3.05σ . The measured amplitude is slightly higher than the simulated amplitude for proton and iron primaries but there are some outliers to higher simulated amplitudes. The RMS of 0.35 for proton primaries and 0.37 for iron primaries is comparable to the estimated total scale uncertainty of 28% [32] for vertical showers of AERA.

7.5.4. Zenith Angle

As shown in section 2.4 the zenith angle is an important parameter for horizontal air showers. Thus, a bias in the measured and simulated radio amplitude would influence the physics analysis describing the characteristics of horizontal air showers. To exclude a bias on the zenith angle, the measured and simulated amplitudes are compared in figure 7.18 for proton primaries and in figure 7.19 for iron primaries for three zenith angle bins. A summary of the amplitude comparison for three zenith angle bins can be seen in table 7.2.

Primary	Zenith angle bin	mean relative difference	RMS
Proton	62° to 68°	-0.11	0.40
Proton	68° to 74°	-0.07	0.32
Proton	74° to 80°	-0.11	0.32
Iron	62° to 68°	-0.13	0.42
Iron	68° to 74°	-0.10	0.34
Iron	74° to 80°	-0.14	0.34

Table 7.2.: Summary of the amplitude comparisons of measured and simulated events for the three zenith angle bins of proton and iron primaries.

The mean relative differences for proton primaries are smaller than for iron primaries. The distributions in the three zenith angle bins show similar behaviour and no zenith angle dependence is observed, because the significance of the comparison with proton primaries of the mean relative difference of the first and second bin is 2.45σ , the second and third bin is 2.86σ and the third and first bin is 0σ . The significance of the comparison with iron primaries of the mean relative difference of the first and second bin is 1.68σ , the second and third bin is 2.59σ and the

7. Analysis of Horizontal Air Showers Detected by AERA

third and first bin is 0.57σ . That is good for future investigations, because then the whole zenith angle range can be used linearly and without parametrisation of the zenith angle dependence.

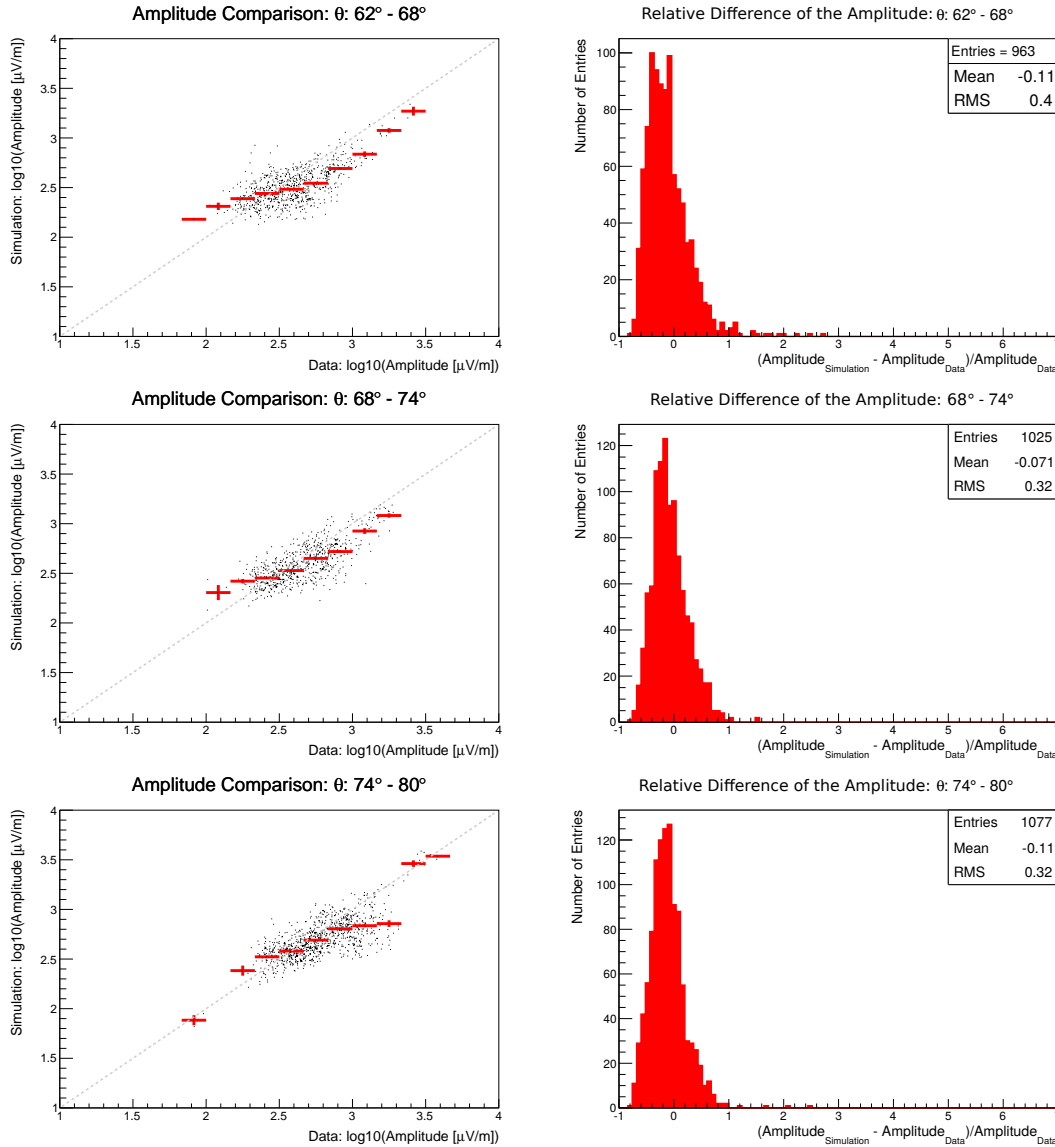


Figure 7.18.: Amplitude comparison of measured and simulated amplitudes for simulated events with proton primaries. The zenith angle range of 62° to 80° is divided into three zenith angle bins. On the left the measured amplitude and the simulated amplitude are drawn. On the right the relative difference of the amplitudes is shown. The number of entries is comparable and the mean of the distribution is compatible at the level of 2.86σ .

7.5. Comparison of Measured and Simulated Amplitudes

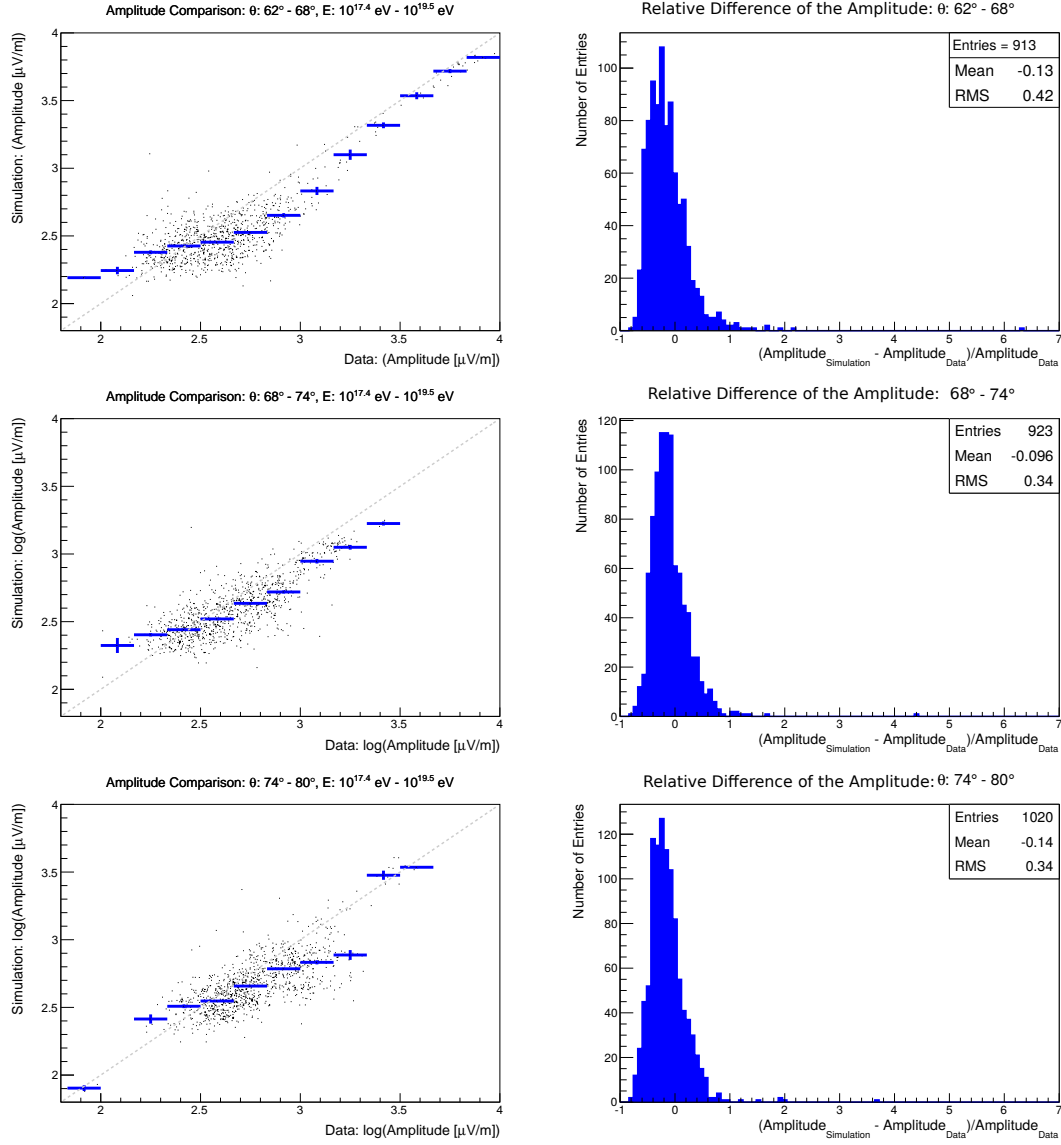


Figure 7.19.: Amplitude comparison of measured and simulated amplitudes for simulated events with iron primaries. The zenith angle range of 62° to 80° is divided into three zenith angle bins. On the left the measured amplitude and the simulated amplitude are drawn. On the right the relative difference of the amplitudes is shown. The number of entries is comparable and the mean of the distribution is compatible at the level of 2.59σ .

7.5.5. Energy

The radio amplitude is proportional to the primary energy, therefore the amplitude increases with the primary energy. The SD HAS reconstruction reaches full efficiency at 4×10^{18} eV. Thus, a bias on the energy should be excluded if only events with energies starting from $10^{17.4}$ eV will be used in physics analysis. The energy range of the measured RdHASObserver events is divided into three bins and the bias of the primary energy on the amplitude is investigated for measured events and simulated events with iron primaries. Figure 7.20 shows the comparison for the three energy bins for proton primaries and figure 7.21 shows the comparison for the three energy bins for iron primaries. A summary of the amplitude comparisons for the three energy bins can be seen in table 7.3.

Primary	Energy bin	mean relative difference	RMS
Proton	$10^{17.4}$ to $10^{18.1}$ eV	-0.06	0.36
Proton	$10^{18.1}$ to $10^{18.8}$ eV	-0.12	0.35
Proton	$10^{18.8}$ to $10^{19.5}$ eV	-0.12	0.22
Iron	$10^{17.4}$ to $10^{18.1}$ eV	-0.09	0.42
Iron	$10^{18.1}$ to $10^{18.8}$ eV	-0.15	0.35
Iron	$10^{18.8}$ to $10^{19.5}$ eV	-0.14	0.20

Table 7.3.: Summary of the amplitude comparisons of measured and simulated events for the three energy bins of proton and iron primaries.

The mean relative differences differ with a significance of 4.47σ for the first and second bin, with 0σ for the second and third bin and 3.04σ for the third and first bin for the comparison with proton primaries.

The mean relative differences values differ with a significance of 3.85σ for the first and second bin, with 0.56σ for the second and third bin and 2.57σ for the third and first bin for the comparison with iron primaries.

The mean relative uncertainties are smaller for simulated events with proton primaries. The relative difference is not energy-dependent. No parametrisation for the energy is needed, when considering further steps in the analysis.

7.5. Comparison of Measured and Simulated Amplitudes

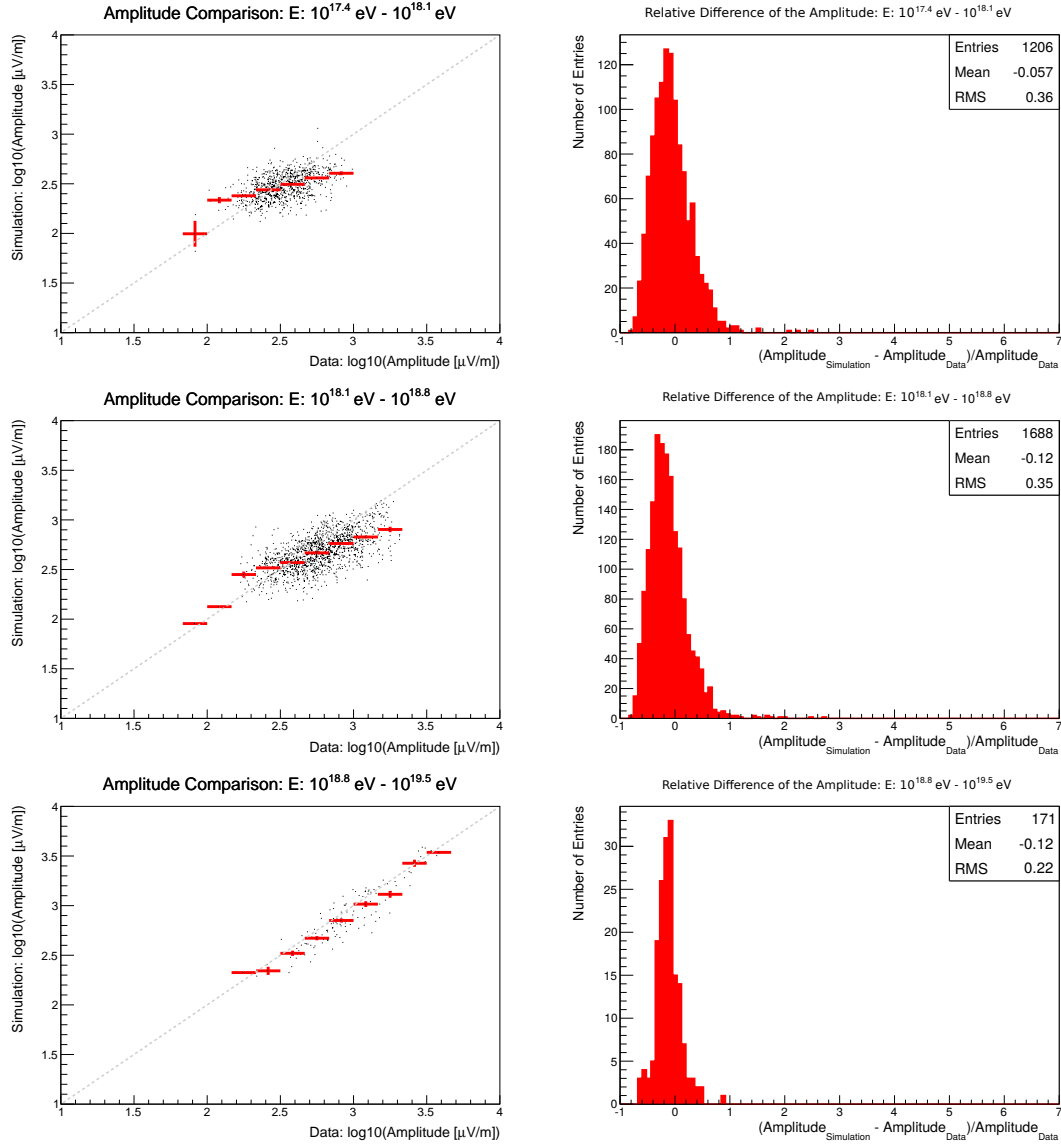


Figure 7.20.: Amplitude comparison of measured data and simulated events with proton primaries. The energy range of $10^{17.4}$ to $10^{19.5}$ eV is divided into three energy bins. On the left the measured amplitude and the amplitude of the simulation are drawn. On the right the relative difference of the comparison is shown. The number of entries differ for the three energy bins, because the flux of primary particles decreases with energy.

7. Analysis of Horizontal Air Showers Detected by AERA

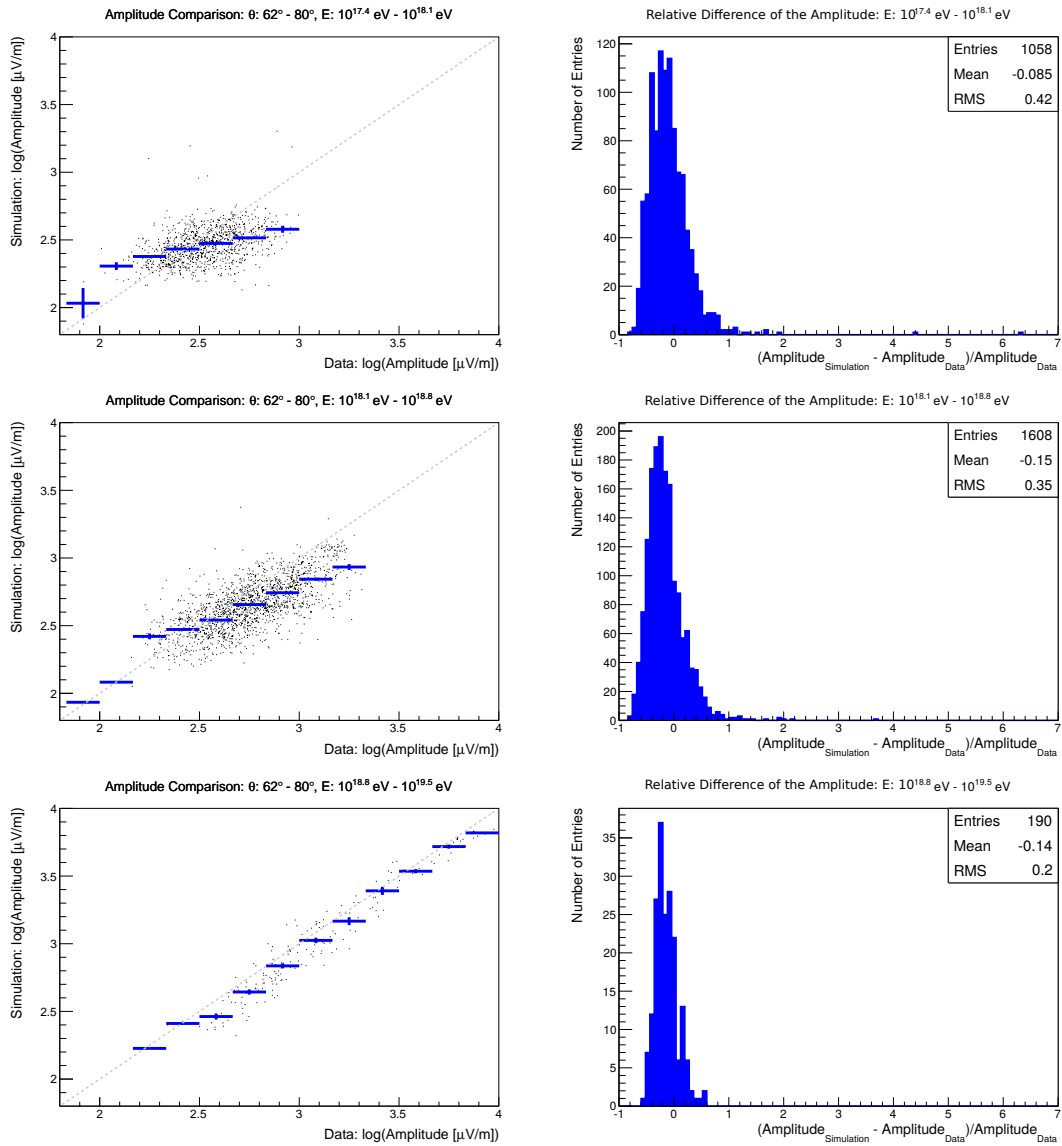


Figure 7.21.: Amplitude comparison of measured data and simulated events with iron primaries. The energy range of $10^{17.4}$ to $10^{19.5}$ eV is divided into three energy bins. On the left the measured amplitude and the amplitude of the simulation are drawn. On the right the relative difference of the comparisons is shown. The number of entries differ for the three energy bins, because the flux of primary particles decreases with energy.

7.5.6. Core Position Relative to AERA

It was checked whether the amplitude depends of the shower core position as reconstructed by relative to the AERA array, in particular the two cases where the SD core is inside or outside the AERA array. This comparison of measured data and simulated events with iron primaries is shown in figure 7.22. Here the three different stages of AERA are treated as a joint data sample and the AERA array was extended with time. Therefore, the number of entries due to the events with core inside the AERA array is smaller than the number of entries due to events with core outside the AERA array. The mean relative difference is -0.18 for events contained and -0.11 for events not contained. This mean values differ with a significance of 4.41σ . This means there is a bias of the amplitude for events contained and not contained in the AERA array. The profile plot for events contained in the AERA array shows a tendency to higher values of measured amplitudes in data for higher amplitudes. This is a effect which should be corrected for in future analyses.

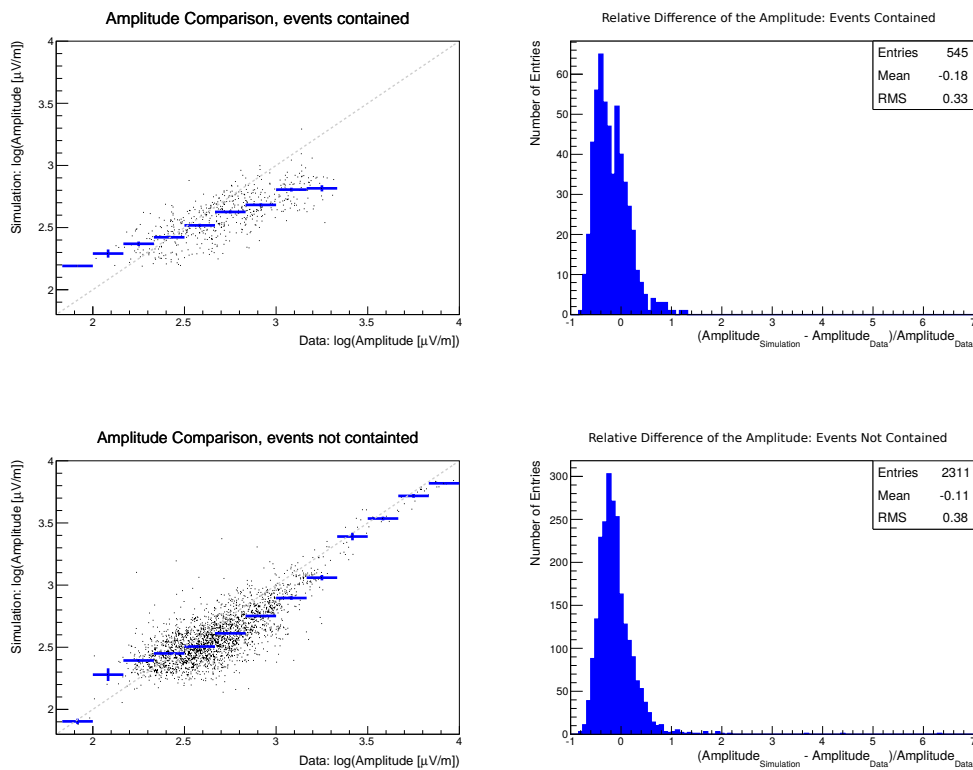


Figure 7.22.: Comparison of measured data and simulated events with iron primaries for events contained and not contained in the AERA array. On the left the amplitudes are drawn and on the right the relative difference is shown.

7.5.7. Antenna Type

The radio antenna for the AERA-24 stage are LPDAs, while in the following stages Butterfly antennas were deployed. For the technical description of the two antenna types see section 3.4. The antenna pattern of the LPDA and the Butterfly station have different directional uncertainties. To check whether the amplitude depends on the antenna type the measured amplitude is compared to the amplitude of simulated events with iron primaries in figure 7.23. The mean relative difference is -0.16 for the LPDA stations and -0.11 for the Butterfly stations. The number of entries is smaller for the LPDA station, because there are fewer LPDA stations deployed than Butterfly stations from AERA-124 on. For the LPDA, events with lower amplitude are measured and for amplitudes above $1000 \mu\text{V/m}$ the distribution is bent towards higher values for measured data. The mean relative difference differs with a significance of 2.99σ for LPDA and Butterfly station and does not indicate a dependence of the amplitude on the antenna type.

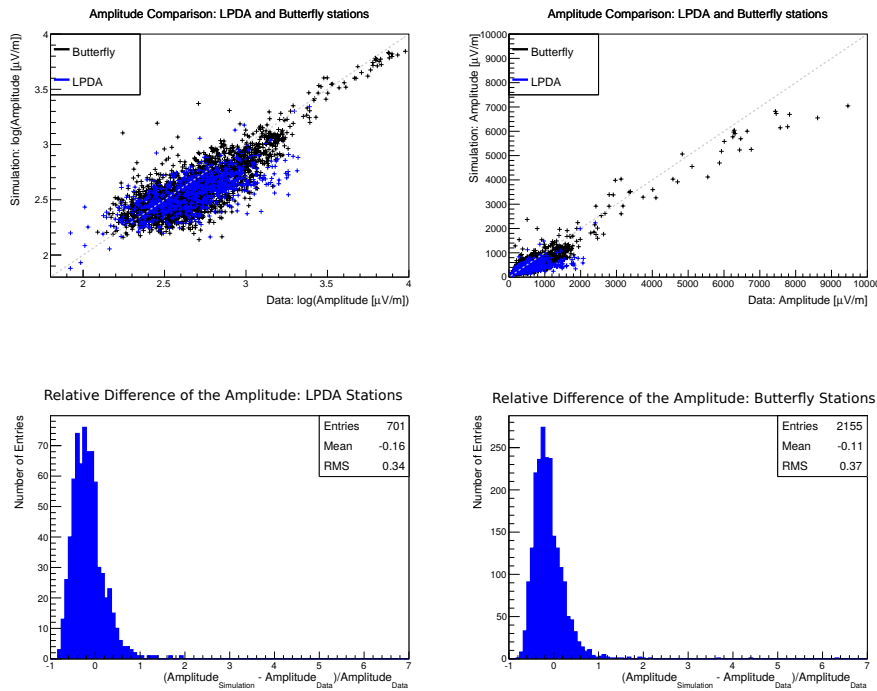


Figure 7.23.: Comparison of measured amplitude and amplitude of simulated events with iron primaries. In blue the LPDA stations and in black the Butterfly stations are drawn. On the upper left plot the axes are logarithmic and on the upper right plot the axes are linear. On the lower plots the relative difference for the LPDA and the Butterfly stations is shown.

7.5.8. Mean Lateral Distribution

The mean radio lateral distribution is a good observable to check for global shifts of the lateral distribution of measured data and simulated events. In a final comparison the mean lateral distribution of all the RdHASObserver events and the simulated events is shown in figure 7.24. The upper plot shows measured data and simulated events with proton primaries, drawn in red, and the lower plot shows measured data and simulated events with iron primaries, drawn in blue. For iron primaries the mean amplitude of measured data is higher than the amplitude of the simulated events up to a distance of 1000 m, afterwards the values are scattered. The amplitudes at small distances differ in the order of 20% for iron primaries. This should be studied further in the future. For proton primaries the mean lateral distribution no significant difference of data and simulation can be seen and no conclusion can be derived. The distributions are relatively flat at smaller distances and then rise for measured data and simulated events. The reason for this is that in the inner part of the lateral distribution the Cherenkov cone valley is visible, which leads to lower amplitudes in the lateral distribution. In figure 7.24 the average of this effect can be seen. Also interesting is that the mean amplitude at a distance of 2500 m from the shower axis of simulated events and measured data is still larger than $200 \mu\text{V}/\text{m}$ for measured data and simulations. The value at 600 m distance to the shower axis in measured data is significantly higher than the simulated events with proton and iron primaries due to outliers and low statistic in this range. No global shift of the lateral distribution can be seen comparing measured data with simulated events with proton and iron primaries.

7. Analysis of Horizontal Air Showers Detected by AERA

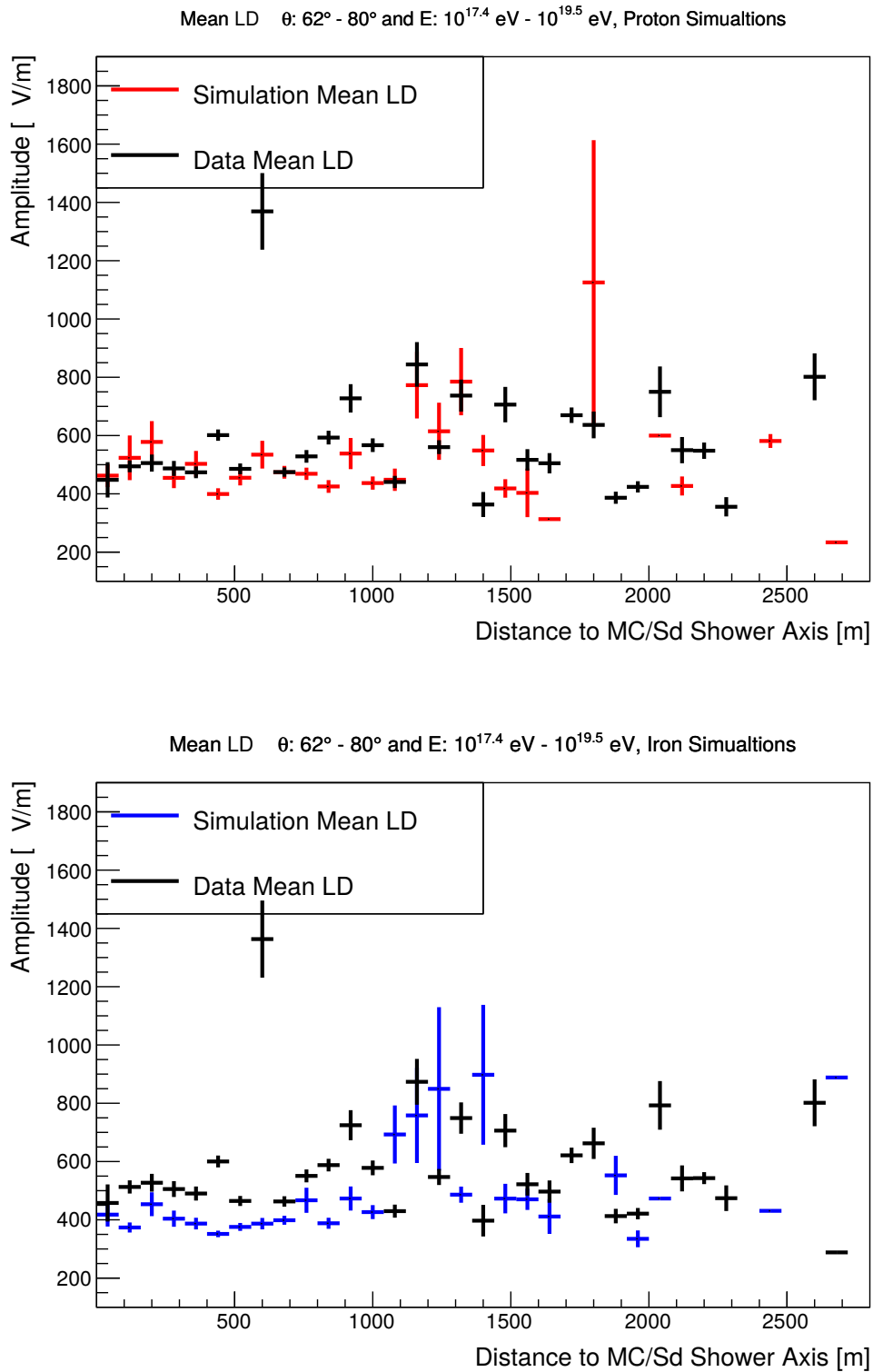


Figure 7.24.: Mean lateral distribution of the measured events and simulated events with proton primaries in the upper plot and simulated events with iron primaries in the lower plot. For each distance to the shower axis of simulated events and measured data bin the mean amplitude is shown.

7.6. Detection Thresholds of Horizontal Air Showers

It is difficult to define an amplitude detection threshold for horizontal air showers. In this chapter the RdHASObserver events were compared to CoREAS simulations. To define a threshold for horizontal air showers simulation studies with different primary energies and directions to cover the whole sky should be performed. Also alternative simulation codes should be investigated. The theoretical detection threshold of $100 \mu\text{V}/\text{m}$ per AERA station is a rough estimate. It was shown in figure 6.15 that the SNR cut of 10 applied in the reconstruction forces the amplitude automatically to larger than $100 \mu\text{V}/\text{m}$. To rely only on simulations for stating a detection threshold of horizontal air showers is also not a good advice, which can be seen in figure 7.25. Here a measured RdHASObserver event was simulated with CoREAS. The upper plot shows the simulation with a smooth LDF. Here a lot of stations with amplitudes above $100 \mu\text{V}/\text{m}$ are included in the LDF. In total 76 stations of AERA-124 contribute to this event. If realistic noise extracted from data of the same time period is added to the simulation, seen in the plot in the middle of the figure, the LDF looks less smooth and the error bars on the amplitude are visible. So at this time the noise condition on the AERA field was not optimal. The number of stations with an SNR above 10 drops to 65 stations. The lower plots shows the measured data. Here the number of stations above SNR cut is 11 and the error bars in the LDF indicate a noisy measurement for the Butterfly stations. All stations above the SNR cut are LPDA stations in this event. It seems like the LPDA is more robust against noisy conditions and the noise is underestimated for the Butterfly stations in this simulated event. Whether LPDA and Butterfly stations show different behaviour towards noise should be checked in future analyses. The stations which pass the SNR cut have amplitudes larger than $100 \mu\text{V}/\text{m}$ in data and the simulated event with noise added, but the number of stations above SNR cut are 11 for data and 65 for the simulated event. Thus, the detection threshold of around $100 \mu\text{V}/\text{m}$ is valid for data and simulations of horizontal air showers.

7. Analysis of Horizontal Air Showers Detected by AERA

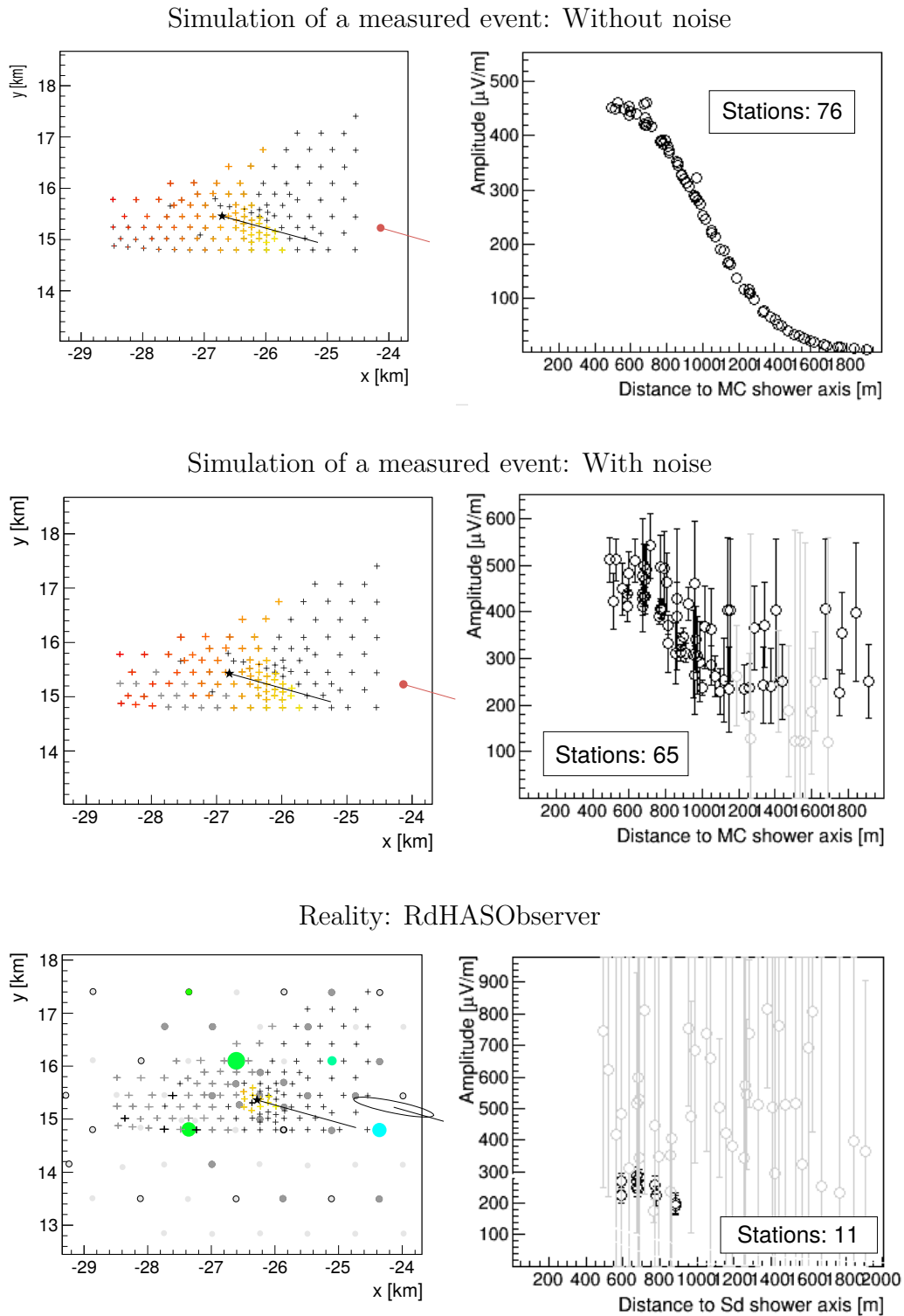


Figure 7.25.: Example event of a simulated RdHASObserver event, for which the LDF looks smooth if no noise is added (upper plot). If noise is added the fluctuations increase and there are error bars of the amplitudes visible (middle plot). The measured RdHASObserver event is shown in the lower plot. The Butterfly stations do not pass the SNR cut of 10 in measured data.

7.7. Efficiency Considerations

To give quantitative statements in a physics analysis the efficiency of horizontal air showers measured by SD should be considered. The energy where the SD HAS reconstruction is fully efficient is only at 4×10^{18} eV. If one would require SD energies larger than 4×10^{18} eV, then only 22 RdHASObserver events would remain of the 427 events in three and a half years of AERA data. This is not surprising taking into account the size of the AERA array and the fact that for horizontal air showers no SD Infill reconstruction is available. In an Auger publication on the SD HAS energy spectrum [47] 255 high quality events detected by the SD standard array and FD are evaluated in ten years of Auger data.

In this chapter, it has been shown that with events triggered by SD also at energies below 10^{18} interesting characteristics can be derived for horizontal air showers with radio. Hence, an SD HAS Infill reconstruction would increase the number of events usable for physics analysis. When providing predictions for the energy and composition determination of horizontal air showers, as described in the next chapter, the fact that events below the full efficiency of SD are used has to be kept in mind.

7.8. Summary

The exemplary event studies and considerations described in this chapter can be concluded in the following. Analysing horizontal air showers detected by AERA gave new insights in

- the large radio footprint of horizontal air showers. This is the first experimentally measurement which confirms the predictions of the size of the radio footprint for horizontal air showers.
- the size of the footprint rises with zenith angle and energy, so is the station multiplicity of AERA.
- the radio signals, which are detectable to large distances up to 5 km.
- the shape of the footprint. Characteristic is the plateau of the Cherenkov cone valley, the elliptic shape and the sharp cut-off on the edges of the LDF.
- the amplitude and the shape of the footprint. Both agree with CoREAS simulations.
- the composition independence of the LDF of the radio amplitudes. This means the LDF is a good energy estimator.

8. Physics with Horizontal Air Showers Detected by AERA

In this chapter a preliminary energy determination based on radio signals of horizontal air showers will be introduced. By correlating the energy determined by radio with information from the SD reconstruction a possible composition determination of the measured air showers will be given. In addition, the data sample of the RdHASObserver will be analysed with regard to a future large-scale array of radio detectors. Finally, the possible detection of neutrino-induced showers will be discussed.

8.1. Energy Estimation of Horizontal Air Showers

After the consistency checks described in section 7.5 of the measured amplitudes with those of simulated events the energy of these events is estimated. This is done using the method first described in [32]. Here, the radiation energy of horizontal air showers is determined by integrating the energy density over a two-dimensional amplitude lateral distribution function (LDF). Then, the radiation energy is compared to the energy determined by the SD horizontal air shower (HAS) reconstruction. This provides a calibration to estimate the primary energy by AERA and the result can be cross checked with FD and CoREAS simulations. Afterwards possible and necessary approaches to improve the energy estimator for horizontal air showers will be pointed out.

8.1.1. Radiation Energy of Horizontal Air Showers

The radiation energy of horizontal air showers is correlated with the amount of energy contained in the electromagnetic component of the air shower. The radiation energy is obtained by fitting a two-dimensional LDF and performing an integration over the footprint of the energy density. In this chapter the LDF is determined by the total power over the distance and not by the amplitude of the radio signal over the distance, as in the chapters before. The two-dimensional LDF used was first proposed and tested for the LOFAR experiment [87]. The total power of the

integrated radio signal P is described at each point (x, y) in the shower plane by

$$P(x, y) = A_+ \cdot \exp\left(-\frac{(x - X_+)^2 + (y - Y_+)^2}{\sigma_+^2}\right) - A_- \cdot \exp\left(-\frac{(x - X_-)^2 + (y - Y_-)^2}{\sigma_-^2}\right) + O. \quad (8.1)$$

The shower plane is spanned by the vectors $\vec{v} \times \vec{B}$ and $\vec{v} \times (\vec{v} \times \vec{B})$. A_+ and A_- are the scaling parameters, X_+ , X_- , Y_+ and Y_- the location parameters, σ_+ and σ_- are the shape parameters and O is an offset parameter. This results in nine parameters for the LDF fit. For the AERA experiment the parametrisation was modified, because the station multiplicity is lower than at LOFAR. The number of parameters is reduced with the help of simulation studies described in [99] and summarized in [100]. The reduced two-dimensional LDF in the $\vec{v} \times \vec{B}$ vs. $\vec{v} \times (\vec{v} \times \vec{B})$ shower plane is described by

$$u(\vec{r}) = A \cdot \exp\left(\frac{-(\vec{r} + C_1 \vec{e}_{\vec{v} \times \vec{B}} - \vec{r}_{\text{core}})^2}{\sigma^2}\right) - A \cdot C_0 \cdot \exp\left(\frac{-(\vec{r} + C_2 \vec{e}_{\vec{v} \times \vec{B}} - \vec{r}_{\text{core}})^2}{C_3^2 \exp(2C_4 \sigma)}\right). \quad (8.2)$$

The parameters C_0 , C_1 , C_2 , C_3 and C_4 are fixed from simulation studies and the respective values can be found in table 8.1. \vec{r} is the location parameter, $\vec{e}_{\vec{v} \times \vec{B}}$ is the location parameter in the $\vec{v} \times \vec{B}$ direction and \vec{r}_{core} is the position of the core. The new free parameters are the amplitude A , the width σ and the position of the core \vec{r}_{core} .

Zenith angle	C_0	C_1	C_2	C_3	C_4
0° - 10°	0.41	8.0 ± 0.3	-21.2 ± 0.4	16.25	0.0079
10° - 20°	0.41	10.0 ± 0.4	-23.1 ± 0.4	16.25	0.0079
20° - 30°	0.41	12.0 ± 0.3	-25.5 ± 0.3	16.25	0.0079
30° - 40°	0.41	20.0 ± 0.4	-32.0 ± 0.6	16.25	0.0079
40° - 50°	0.46	25.1 ± 0.9	-34.5 ± 0.7	16.25	0.0079
50° - 60°	0.71	27.3 ± 1.0	-9.8 ± 1.5	16.25	0.0079

Table 8.1.: Parameters of the two-dimensional LDF fit function (equation 8.2) of for AERA measured events. These parameters are fixed by a simulation study [100].

With this parametrisation it is possible to determine the radiation energy. Following [100] the energy estimator S_{radio} is the spatial integral of the lateral distribution function and will deliver the amount of radio emission from the primary

cosmic ray

$$S_{radio} = \frac{1}{\sin^2 \alpha} \int_{\mathbb{R}^2} u(\vec{r}) d^2 \vec{r} = \frac{A\pi}{\sin^2 \alpha} (\sigma^2 - C_0 C_3^2 \exp(2C_4 \sigma)). \quad (8.3)$$

This parametrisation was developed for vertical showers from 0° to 60° and has to be improved for horizontal air showers. In a final step the parameters of the zenith

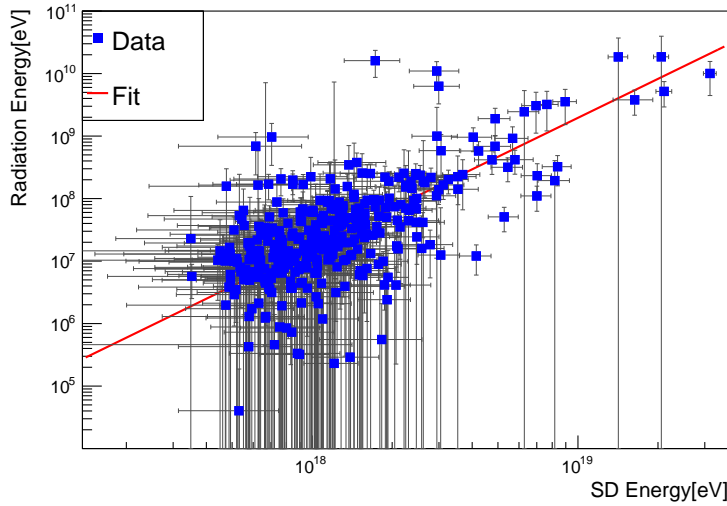


Figure 8.1.: Preliminary energy estimator for horizontal air showers applied to the RdHASObserver dataset. The correlation efficient is 0.64. The energy estimator is determined for 390 of the 427 measured events. For the remaining 37 events the two-dimensional LDF fit does not converge. The energy estimator for horizontal air showers and the two-dimensional LDF fit function are not optimised for horizontal air showers.

angle bin from 50° to 60° of table 8.1 are used to determine the radiation energy for the RdHASObserver data sample. The simulation study for the parameter range of 62° to 80° zenith angle is not available. Hence, as a first attempt if the method works also for HAS, the parametrization from 50° to 60° was used. In chapter 7 we have seen that this will not lead to a very strong effect, as the zenith angle does not bias the amplitude. The result can be seen in figure 8.1. The energy determined by SD and the radiation energy determined by AERA have a correlation coefficient of 0.64. The uncertainty of the SD energy is the uncertainty of the SD HAS reconstruction. The uncertainty of the radiation energy are larger, because the fitting function was not optimised for horizontal air showers. The parametrization from 50° to 60° was used. The uncertainty of the radiation energy above the full efficiency of the SD trigger (energy determined by SD $> 4 \times 10^{18}$ eV) are of

the same order as the energy determined by SD. The uncertainty of the radiation energy is the propagated uncertainty of the fit of the LDF quadratically added to the total shower-to-shower uncertainty of 12.8%, plus the total systematic absolute scale uncertainty of 28% [32]. The shower-to-shower uncertainty is composed of the temperature dependence of the gain of 8% and the uncertainty on the angular dependence of the antenna response pattern of 10%. The total absolute scale uncertainty is the uncertainty on the absolute scale of antenna response pattern of 25% and the uncertainty of the analogue signal chain of 12%. The fit sketched in figure 8.1 provides an energy calibration according to [32]. The fit function is

$$S_{radio} = A \cdot 10^{17} \text{eV} \cdot \left(\frac{E_{SD}}{10^{18} \text{eV}} \right)^B \quad (8.4)$$

with the fit parameters A and B and the SD Energy E_{SD} . The fit quality is reasonable despite the large scatter of data points. The fit results in $A = 1.67 \pm 0.15$ and $B = 2.07 \pm 0.06$. Within the uncertainties the exponent B of the fit is the same as for vertical showers of AERA-24 ($A = 1.58 \pm 0.07$ and $B = 1.98 \pm 0.04$) [32].

This radio HAS energy estimator is preliminary and not optimised for horizontal air showers. Possible sources of the large scatter of data points, the large spread and the outliers could be that the two-dimensional LDF fit function does not describe the measured amplitudes very well. The reason for this could be the parameters of the LDF fit function, which are for a different parameter range (zenith angle of 50° to 60° instead of 62° to 80°). Another reason could be that the method was developed originally for vertical showers of AERA-24, which contained only LPDA stations with a distance of 125 m. For vertical events recorded with AERA-24 the SD core is very close to the AERA array or contained in the AERA array, because the footprint of vertical showers is usually smaller than the footprint of horizontal air showers. It has to be checked whether the energy estimation works for events too, in which the SD core is not contained in the AERA array. Additionally, the SD core estimation for the SD HAS reconstruction has larger uncertainties than the SD Infill core reconstruction (see chapter 6). An insufficient core estimation could also influence the energy estimator. This will be discussed in the following.

Antenna Type

The energy estimator was developed for vertical events of AERA-24. In this stage AERA consisted only of LPDA stations. To test whether the energy estimator can be improved only events of AERA-24 are displayed in figure 8.2. The energy determined by SD and the radiation energy determined by AERA have a correlation coefficient of 0.38. In figure 8.3 events of AERA-124 and AERA-153 are drawn. Here the AERA array consists of LPDA and Butterfly stations. The correlation coefficient is 0.25. No clear improvement can be seen in using only LPDA stations,

8.1. Energy Estimation of Horizontal Air Showers

because figure 8.2 has a lot of outliers. The reason for this could be that the SD core precision for horizontal air showers is not sufficient and worse compared to vertical showers. The mean area of the uncertainty ellipse of the core determined by SD is 0.48 km^2 for horizontal air showers, compared to 0.0042 km^2 for vertical showers for the data samples.

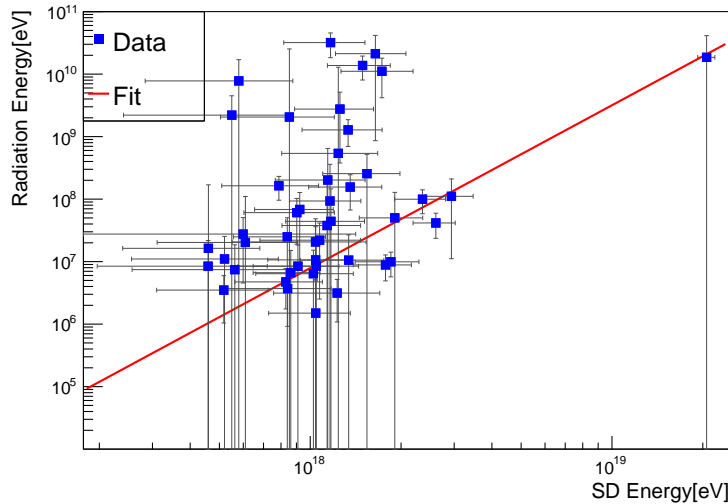


Figure 8.2.: Radiation energy versus SD HAS energy for AERA-24 events. The correlation coefficient is 0.38.

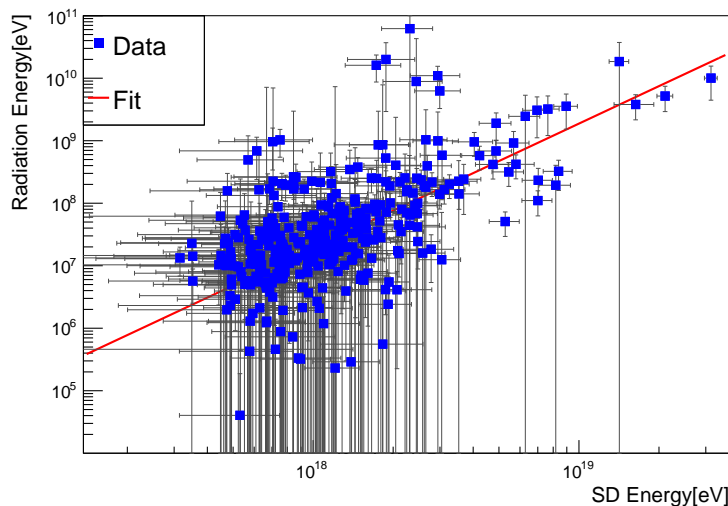


Figure 8.3.: Radiation energy versus SD HAS energy for AERA-124 and AERA-153 events. The correlation coefficient is 0.25.

Floating Parameter Fit

Another test is to let the parameters C_0 , C_1 , C_2 , C_3 and C_4 float freely in the two-dimensional LDF fit. The parameters are normally fixed by simulation studies for AERA events and the values can be found in table 8.1. The parameters C_3 and C_4 are averaged over the zenith angle range from 0° to 60° , but a zenith angle dependence for horizontal air showers cannot be excluded and therefore the parameters are also free in the floating parameter fit. In the previous radiation energy determinations the values of the zenith angle bin from 50° to 60° have been used. Now nine instead of four parameters are fitted with the two-dimensional LDF. For only 85 of the 427 RdHASObserver events the radiation energy could be determined with a floating parameter fit. For the remaining 342 events the fit does not converge. The radiation energy versus the SD HAS energy of these 85 events can be found in figure 8.4. The energy determined by SD and the radiation energy determined by AERA have a correlation coefficient of 0.42 for the floating parameter fit and is worse than the fit with the parameters defined for the 50° to 60° zenith angle bin. Leaving all nine parameters free does not improve the energy determination and reduced the number of events for which the energy can be determined. The fit often does not work with the function 8.4. Therefore a similar simulation study as described in [99] should be performed for the zenith angle range of 62° to 80° to improve the energy estimator for horizontal air showers, which was not possible in the frame of this thesis. Another reason could be that the calibration and reconstruction of AERA, in particular the Butterfly antenna stations, need to be further improved.

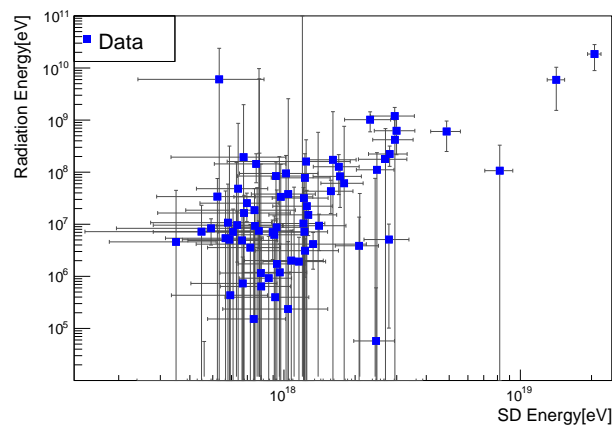


Figure 8.4.: Radiation energy versus SD HAS energy with floating LDF fit parameters fit. The correlation coefficient is 0.42.

8.1.2. Primary Energy

Comparison of the Radio Energy with the Surface Detector Energy

Fitting the radiation energy and SD energy distribution allows to estimate the radio energy when the fit function 8.4 is solved for E_{SD} . The radio HAS energy, named RD energy in the following, compared to the SD HAS energy with a Gaussian fit to the relative difference can be seen in figure 8.5. With an ideal energy reconstruction method the events would all lie on the 1:1 correlation line and the mean value of the relative difference and the sigma would be zero. The relative difference distribution has a tail to the right to higher RD energies. To neglect the outliers a Gaussian fit is applied. One issue is that the same data sample is used for the calibration and energy determination due to the small sample size and the large systematic uncertainties. The performance of the method could be over-estimated compared to an independent sample.

This energy estimator has a width of the relative difference of 48%, which is worse than the width of the relative difference of 29% for vertical events of AERA-24 [32]. The reasons for the large relative difference could be the non-optimised fit function or method, the larger uncertainties of the SD reconstruction (SD standard array instead of SD Infill) or the different spacing and antenna types of AERA-124 and AERA-153. Additional cuts on the radio reconstruction are applied for the vertical event selection, which also have to be adapted for horizontal air showers. Some investigations follow to narrow down the causes of the worse energy resolution.

To exclude a zenith angle dependence the events were divided into three zenith angle bins. Figure 8.6 shows the correlation of RD and SD energies in the three zenith angle bins with their relative differences and a Gaussian fit. The width of the relative difference is 62% for the first bin ($\theta : 62^\circ - 68^\circ$), 42% for the second bin ($\theta : 68^\circ - 74^\circ$) and 45% for the third bin ($\theta : 74^\circ - 80^\circ$). The mean relative differences of the Gaussian fits are all compatible with zero. No significant zenith angle dependence of the energy estimator can be seen.

To exclude a dependence of the energy estimator on the core position relative to AERA, i.e. whether the SD core is contained or not contained in the AERA array, the plots of figure 8.7 were generated. Here, the events with the SD core contained in the AERA array show a width of the relative difference of 47% and all outliers with relative difference larger than 600% can be found in the events in which the SD core is not contained in the AERA array. For these events the width of the relative difference is 49%. The significance of the shift in the mean value of the Gaussian fits for events contained and not contained in the AERA array is 0.47σ . To narrow the spread of the energy estimator for horizontal air showers and to reduce the number of outliers another optimisation of the LDF is needed to include also events with SD core not contained in the AERA array. The calibration of the Butterfly station would improve spread and is work in progress.

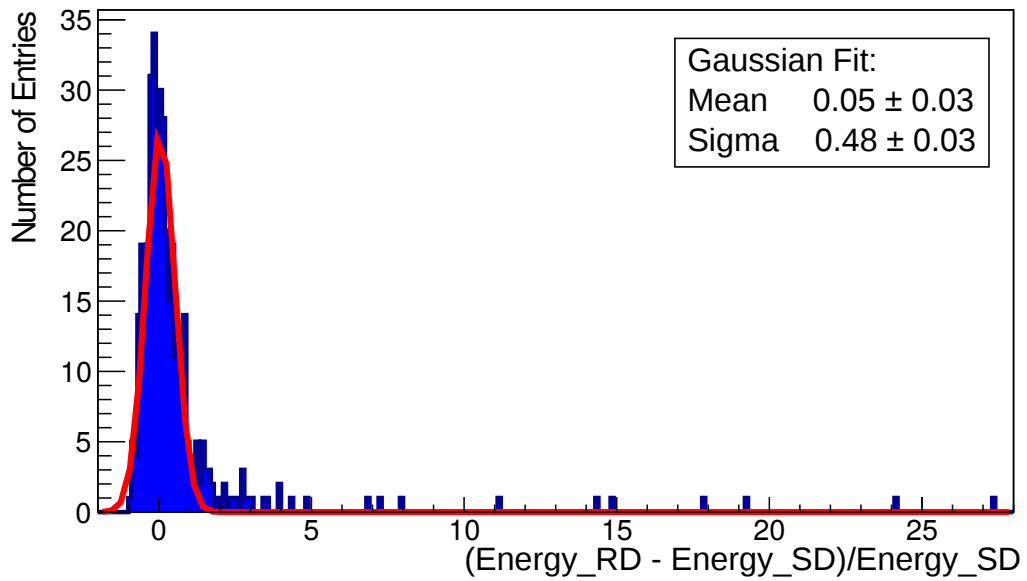
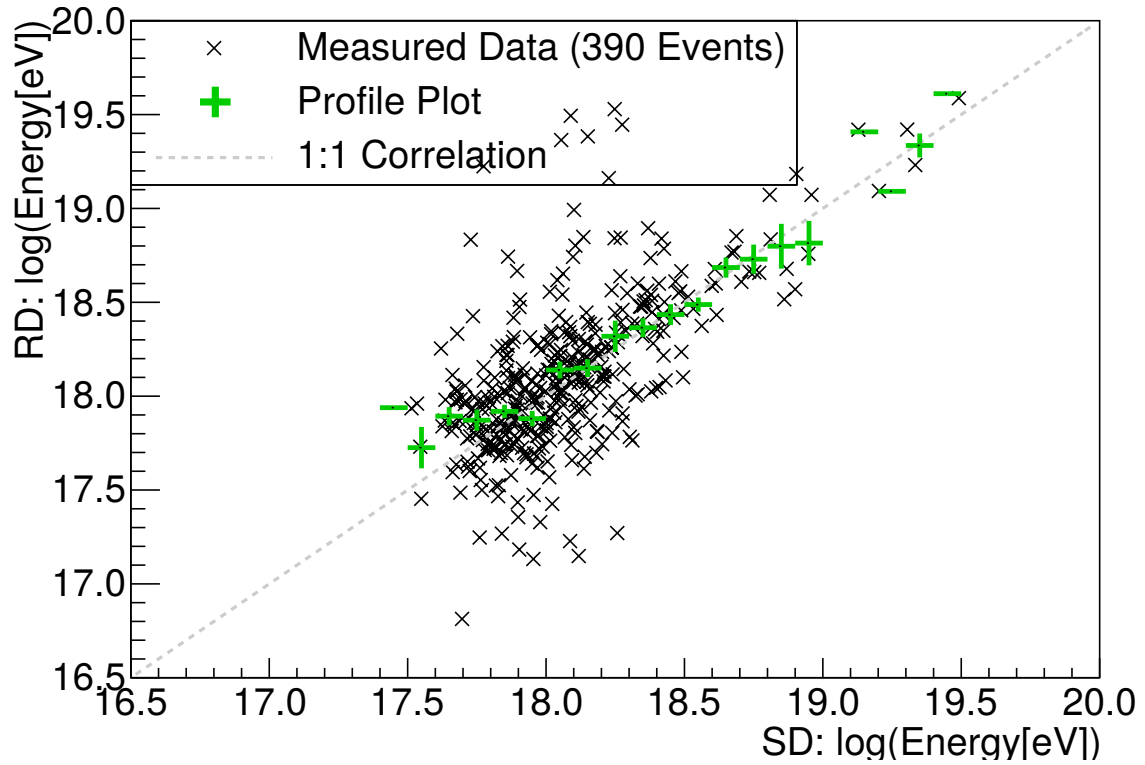


Figure 8.5.: RD HAS energy versus SD HAS energy in the upper plot. The events are drawn with black crosses and the profile plot is drawn in green. The relative uncertainty with a Gaussian fit is shown in the lower plot. The sigma of the Gaussian fit is 0.48 and the mean is 0.05.

8.1. Energy Estimation of Horizontal Air Showers

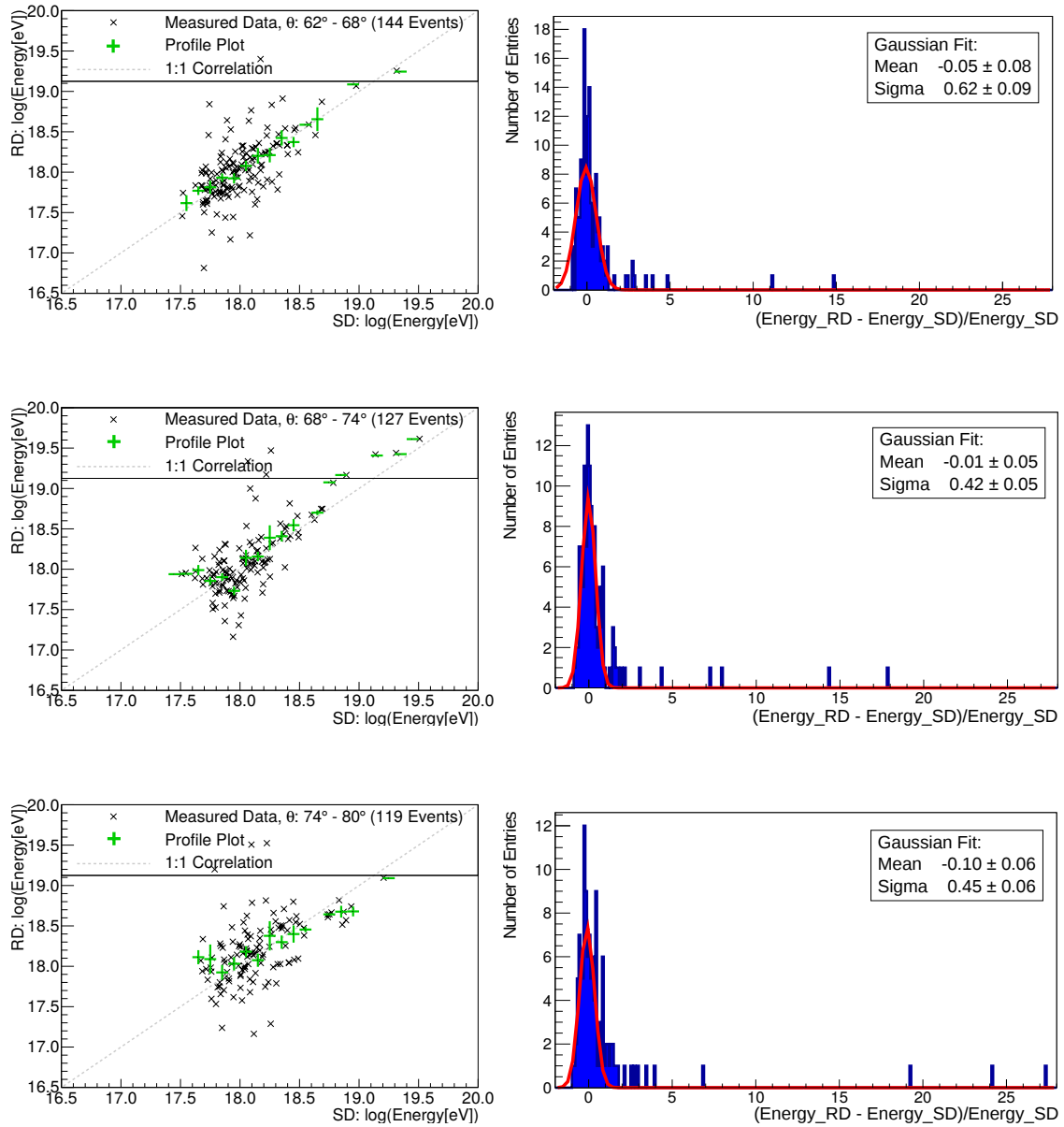


Figure 8.6.: The left plots show the RD HAS energy versus SD HAS energy divided into three zenith angle bins. The black crosses mark the events and the profile plots are drawn in green. The right plots show the relative difference with Gaussian fits of the correlation plots on the left.

The uncertainty of the angular dependence of antenna response pattern is of the order of 10% for vertical events but higher for horizontal air showers and has to be quantified. The event selection of horizontal air showers also needs to be optimised in future studies.

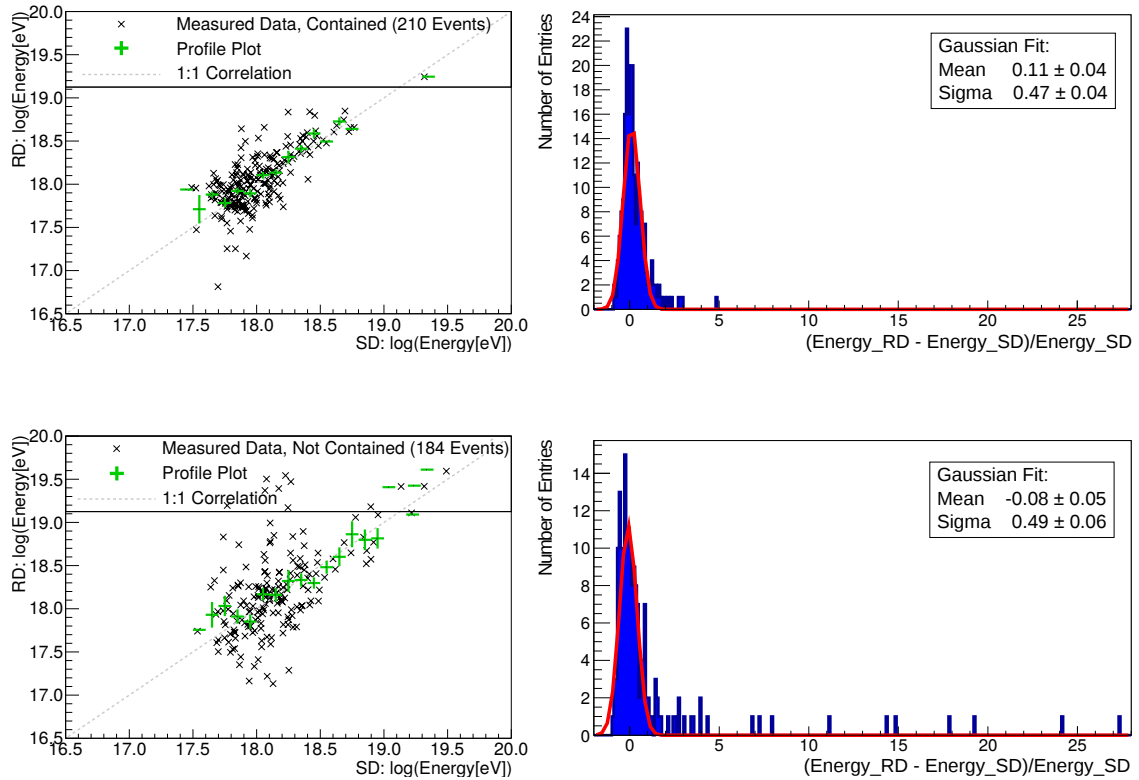


Figure 8.7.: The upper plots show the events for which the SD core falls inside the AERA array, and the lower plots shows the events for which the core is outside the array. The left plots show the RD HAS energy versus the SD HAS energy and the right plots the relative difference of the selection with Gaussian fits.

Comparison of the Radio Energy with the Fluorescence Detector Energy

The RD HAS energy can also be compared to the energy determined by FD. This will serve as a cross-check for the SD HAS energy determination, which is derived by fitting a function to the SD HAS energy estimator N19 versus the FD energy distribution [46]. Events above 4×10^{18} eV are considered for this energy determination. Considering the SD HAS full efficiency would cut the RdHASObserver event sample to 22 events. For details see the discussion in section 7.7. Of these 22 events only two RdHASObserver events are also detected by FD.

In the full RdHASObserver data sample 19 events are detected with FD and SD.

For 17 of them the radio energy could be determined. Figure 8.8 shows the RD energy versus the FD energy with the relative difference. In this selection no FD cuts are applied. The width of the distribution is of the same order as the RD HAS and SD HAS comparison.

Figure 8.9 shows the SD HAS energy versus the FD energy for the events which are also detected by AERA. Here, also no FD cuts are applied. It is not possible to decide from these two comparisons whether SD or AERA determine the cosmic ray energy with smaller relative difference with respect to FD.

The number of events detected also by FD is that small, because FD has an uptime of only $\sim 13\%$ [46]. To derive reliable statements more statistics is needed. This can be achieved by taking AERA data for a longer time period, extending the AERA array or implementing an SD HAS Infill reconstruction. For the SD-FD energy spectrum a dataset of 255 high quality events, detected in ten years of the Auger array is used [47].

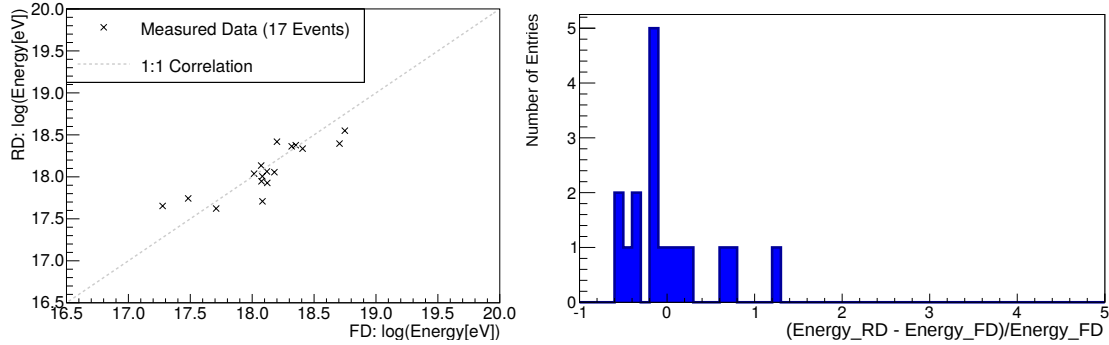


Figure 8.8.: The left plot shows the RD HAS energy versus the FD energy of the events also detected by SD. Data is marked with black crosses. The right plot shows the relative difference.

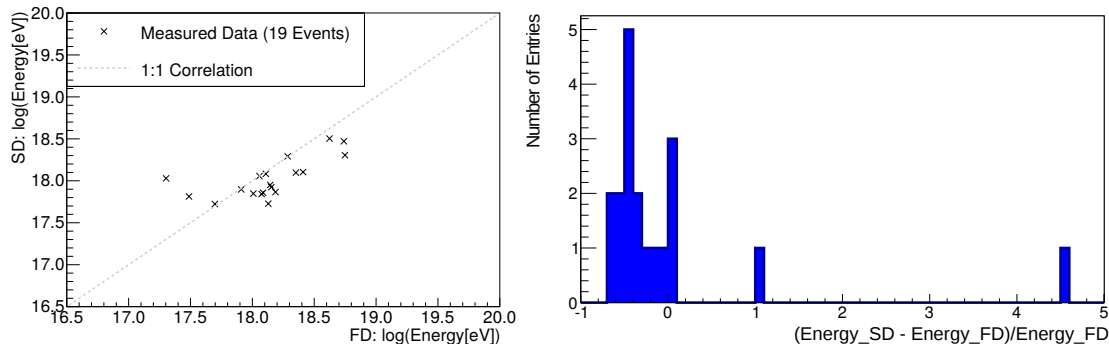


Figure 8.9.: The left plot shows the SD HAS energy versus the FD energy of the events also detected by AERA. Data is marked with black crosses. The right plot shows the relative difference.

Comparison of the Radio Energy with CoREAS Simulations

To test the energy estimator for horizontal air showers the RD HAS energy of the simulated events is compared to the MC input energy for simulated events with proton and iron primaries. The upper left plot of figure 8.10 shows the comparison for simulations of proton-induced showers and the lower left plot shows the comparison for simulations of iron-induced showers. The right plots show the relative difference with Gaussian fits.

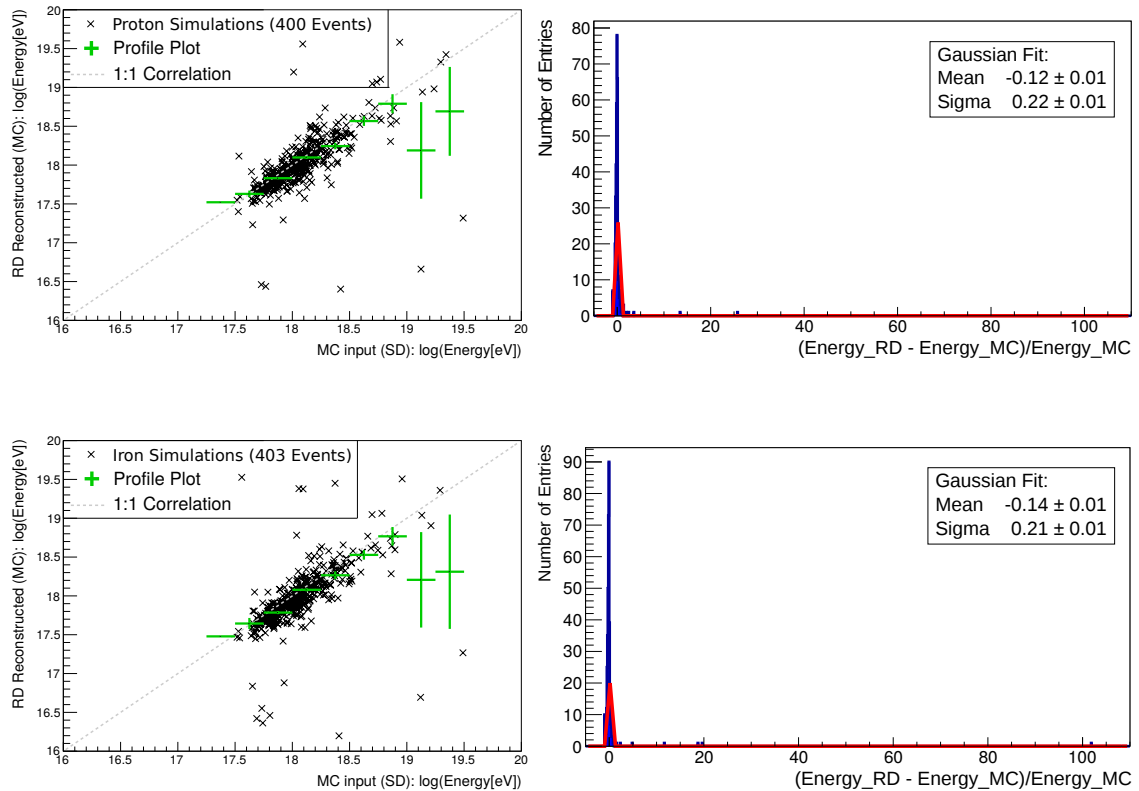


Figure 8.10.: On the upper plots the reconstruction of proton simulations and on the lower plots the reconstruction of iron simulations are shown. The left plots show the reconstructed RD HAS energy of the simulated RdHASObserver events versus the MC input energy. The right plots show the relative difference with Gaussian fits.

Unfortunately, the distributions of simulated events with proton and iron primaries have some outliers to higher and lower reconstructed energies. In the simulation the energy estimator can be determined for 400 simulated events with proton primaries and 403 simulated events with iron primaries. The width of the Gaussian fit to the relative difference for simulated events with proton primaries is 22% and for simulated events with iron primaries 21%. This provides the best mean

difference which can be achieved by using the preliminary energy estimator for horizontal air showers. In summary, the good resolution shows that the preliminary energy determination works indeed with respect to these resolutions.

There are alternative ways to determine the cosmic ray energy by radio measurements. For the LOPES experiment the LDF is fitted and the amplitude at a reference value of 100 m distance to the shower axis is used and this amplitude is cross calibrated with the energy determined by KASCADE [101]. The relative difference of the energy determination of LOPES is 13% on CoREAS simulations and 20-25% on individual measured events (including the uncertainty of the host experiment KASCADE). The Tunka-Rex energy estimation works by fitting the radio LDF and taking the amplitude at a reference value of 120 m and cross calibrating this amplitude to the energy determined by Tunka-133 [76]. The precision of the Tunka-Rex energy determination is comparable to the Tunka-133 energy determination of 15%. These reference values of 100 m and 120 m have been chosen empirically. For vertical showers of AERA this has been tried with a reference value of 110 m. A better result has been achieved by integrating the energy density of a two-dimensional LDF, which led to the publication [32]. For LOPES and Tunka-Rex the distance between the stations is smaller compared to AERA (see section 2.3.2) and therefore the density of the stations is higher and leads to a better resolution if the core is contained.

For horizontal air showers the lateral distribution is too complex to choose one reference value. The distance of the closest AERA station to the SD axis can be up to 5 km (see figure 6.10). Depending of the zenith angle the Cherenkov cone valley is visible and therefore it would be hard to decide which value should be used.

A further method to determine the energy of horizontal air showers could be to interpolate the data points the lateral distribution linearly, because the number of stations is sufficient for horizontal air showers or to determine the plateau of the LDF and fit the plateau itself or to fit the slope of the LDF. Testing these alternatives was not possible in the frame of this work. However, the introduced preliminary energy estimator of horizontal air showers can be the basis for further improvements of the energy estimator for horizontal air showers by radio.

8.2. Composition Determination of Horizontal Air Showers

CoREAS simulations indicate that a proton shower has a different radio footprint than an iron shower. This can be seen in figure 8.11. CoREAS simulations were performed for a vertical proton and iron shower with energy of 10^{17} eV at the LOPES site [102]. The asymmetry and the different slope of the LDF can be seen. The source of this difference is the different generic distance to the shower maximum for proton and iron primaries from the antenna. However, for horizontal air showers this difference is smeared compared to the absolute distance from the antenna. Therefore, larger uncertainties and less sensitivity is expected. The first

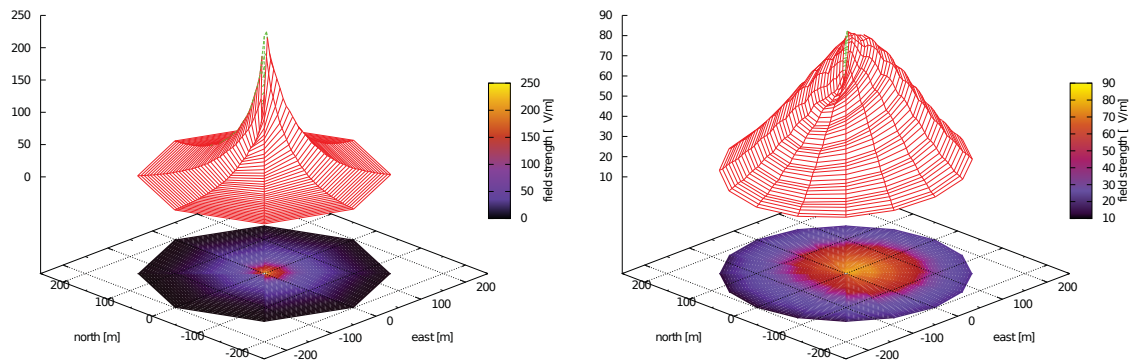


Figure 8.11.: Lateral amplitude distributions of proton (left plot) and iron (right plot) generated CoREAS simulations of vertical showers of 10^{17} eV for the LOPES site [102].

attempt to determine the composition with a radio detector were performed with the LOPES experiment [101]. The determination method was called slope method. Simulated events with proton and iron primaries have different LDF slopes in radio. With this method the uncertainty of X_{\max} , the depth of shower maximum, is ± 50 g/cm² on CoREAS simulations and ± 90 g/cm² on measured data of LOPES can be achieved. The X_{\max} parameter is sensitive to the shower development.

The detection threshold for AERA is about $100 \mu\text{V/m}$, so that the iron shower of figure 8.11 would not be detected by AERA. The footprint of the proton shower would have had a diameter of 100 m. The distance between the AERA stations depends on the AERA stage and is between 125 m and 750 m. For a direction reconstruction a minimum of three stations is required, hence the proton shower of figure 8.11 would also not be reconstructed because due to the distance of the antennas the requirement of three stations would not be fulfilled. Showers with higher energy and larger zenith angle are more suitable for the composition determination with AERA.

One of the current attempts to determine the composition with AERA is by the determination of X_{\max} with CoREAS simulation studies by matching the shape of the measured lateral distribution with a two-dimensional LDF fitted to the simulations [103]. This works by performing lots of simulations with proton and iron primaries resembling one measured event. Figure 8.12 shows one measured RdObserver event with a best suited two-dimensional LDF regarding X_{\max} determination on the left and the χ^2/ndf versus X_{\max} distribution of simulated events with proton and iron primaries on the right. The X_{\max} value with the minimal reduced χ^2 values provides the X_{\max} determined by AERA. The X_{\max} value can then be cross checked with events also detected by FD. With this method an uncertainty of $\pm 34 \text{ g/cm}^2$ on measured RdObserver events can be achieved [100].

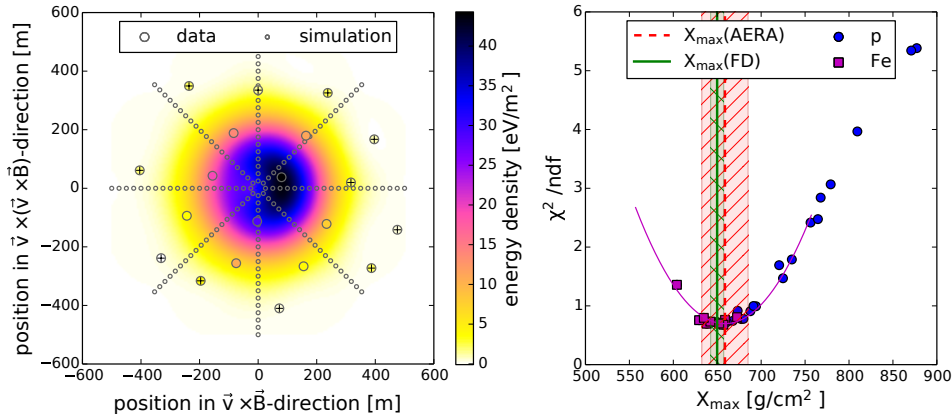


Figure 8.12.: On the left a two-dimensional LDF can be seen for measured data and the best simulated event according to the minimal χ^2/ndf of the right plot. On the right the χ^2/ndf versus X_{\max} distribution of the simulated events can be seen. The X_{\max} determined by FD is shown in green with its uncertainties [103].

The X_{\max} method does not work for horizontal air showers because the information on X_{\max} is lost during the long distance the shower has to travel. Simulated events with proton and iron primaries have very similar shape. In figure 8.13 the amplitudes of simulated events with iron primaries versus simulated events with proton primaries of the measured RdHASObserver events are compared. The profile distribution of the upper plot shows good agreement between the two sets and in the lower plot it is shown that the relative difference is of the order of 1%. This is on the one hand good, because it means that the footprint of the shower is a good energy estimator for horizontal air showers, because it is independent of the primary mass, but on the other hand it will be difficult to determine the composition by the radio LDF of horizontal air showers alone.

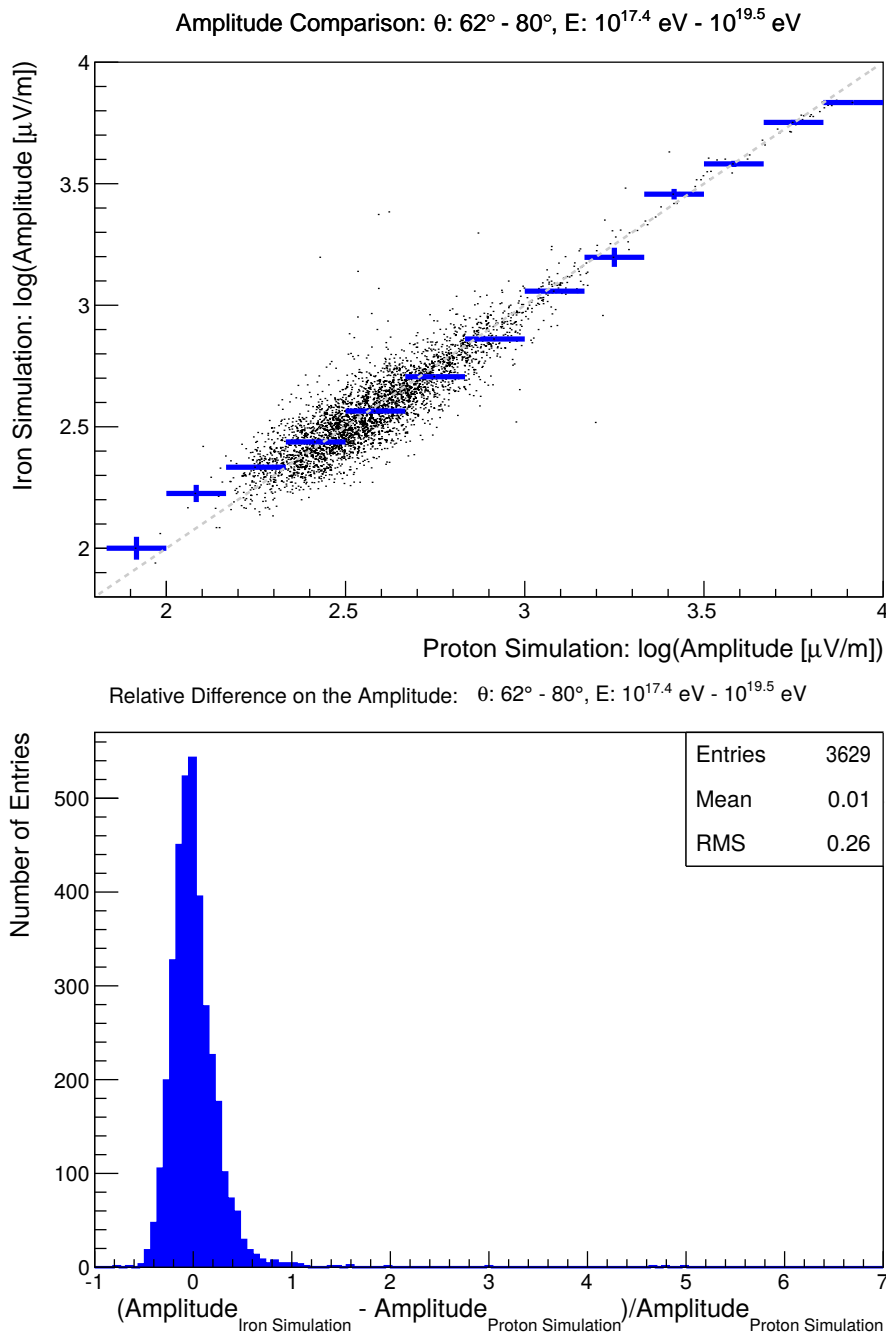


Figure 8.13.: Comparison of simulated events with iron and proton primaries. The input for the simulations are the measured RdHASObserver events. In the upper plot the amplitude of the stations participating in the simulated events with iron primaries versus the amplitude of the stations participating in the simulated events with proton primaries are drawn in black. The number of entries is larger than for the data - simulation comparison, because in the simulation - simulation comparison an ideal detector is assumed, where all stations participate in an event. The profile plot is shown in blue. In the lower plot the relative difference of the comparison is shown. The mean value is 0.01.

The shape of the LDF is different for proton-induced and iron-induced showers, but with the station distance of AERA the two-dimensional LDF fit described in 8.1 is not the best suited tool to distinguish between proton and iron showers for horizontal air showers. To determine the composition only by using the radio LDF a higher precision would be needed for horizontal air showers. This could be achieved with the future SKA experiment, which will be able to perform even tomography of the radio emission of extensive air showers [104] due to the huge number of antennas participating per event.

However, in hybrid mode, i.e. with help of SD the composition can be determined with AERA. In a CoREAS simulation study of horizontal air showers [105] it was shown that for simulations with fixed shower geometry and energy the degeneracy of the primary mass can be broken. In figure 8.14 the electric field at 400 m distance to the shower axis and the energy estimator N19 of SD are compared. At the time the simulation study was performed no energy estimator for horizontal air showers was available. The data sample contains 163 simulated events with proton primaries and 65 simulated events with iron primaries with an energy of 10^{19} eV, a zenith angle of 70° and the shower direction E. The AERA stations are arranged in a grid of 750 m spacing and for SD the standard grid of 1500 m is used.

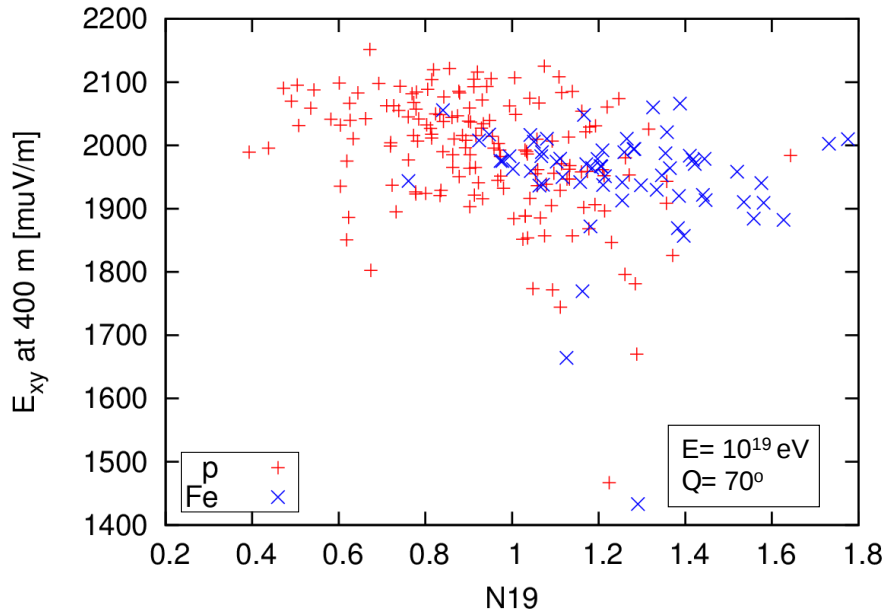


Figure 8.14.: Comparison of the radio amplitude of the XY-component of the electric field at 400 m distance to the shower axis and the energy estimator N19 of SD. The simulation sample consists of 163 proton and 65 iron showers with an energy of 10^{19} eV, a zenith angle of 70° , and the shower direction east [105].

With projecting N19 in the electric field bin 1900 $\mu\text{V}/\text{m}$ to 2100 $\mu\text{V}/\text{m}$ proton and iron showers can be distinguished. The energy of the shower is then determined by AERA and the composition can then be determined by the energy estimator N19 of SD, because it depends on the number of muons produced in the air shower. The merit factor provides a separation power of primary i and j by

$$f_{MF} = \frac{|\langle S_i \rangle - \langle S_j \rangle|}{\sqrt{\sigma(S_i)^2 + \sigma(S_j)^2}} \quad [9]. \quad (8.5)$$

Merit factors of 1.5 or higher allow a comfortable separation of the tested primaries [9]. The value of the merit factor is 1.1 for the simulation study of horizontal air showers described in [105], which is reasonable for a successful separation. This is comparable which simulation studies for the current plans for the upgrade of the SD detectors of Auger [9], given a merit factor of 1.31 of proton and iron for showers of 10 EeV. The plan of the upgrade of the Pierre Auger Observatory is to attach the SD tanks with scintillators on top of the tanks. The N19 distribution of the simulation study can be seen in figure 8.15. This merit factor can be achieved with an ideal energy resolution and known geometry of the air shower.

Merit factor for fixed (ideal) energy

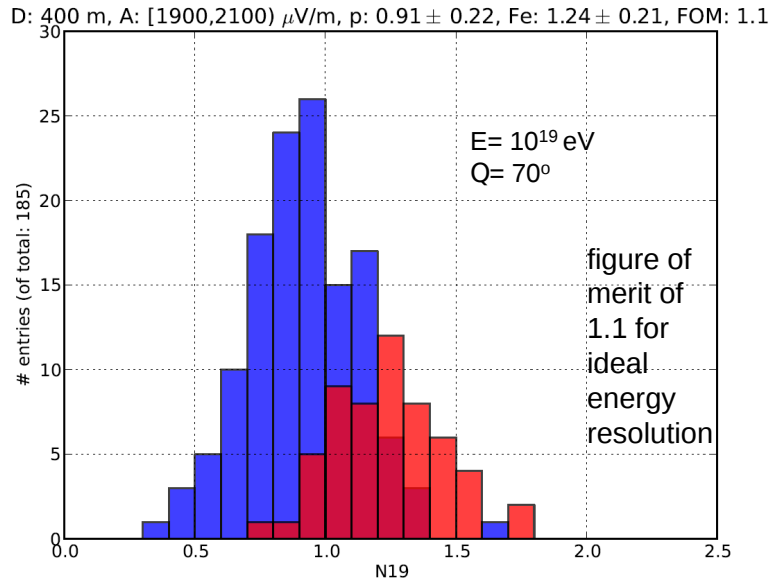


Figure 8.15.: N19 projection for a range of the electric field from 1900 $\mu\text{V}/\text{m}$ to 2100 $\mu\text{V}/\text{m}$ of the horizontal air shower simulation study. The merit factor is 1.1 [105].

Using the information above, the composition in measured RdHASObserver events can be examined. The energy estimator N19 is displayed as a function of the RD energy in figure 8.16. The histogram of the N19 parameter of the events is shown in figure 8.17 and the histogram of the RD energy is shown in figure 8.18. A threshold effect of N19 can be seen, because no N19 value below 0.07 is observed. This means that the energy reconstructed by SD has a certain reconstruction threshold too. All measured AERA events could be simulated with

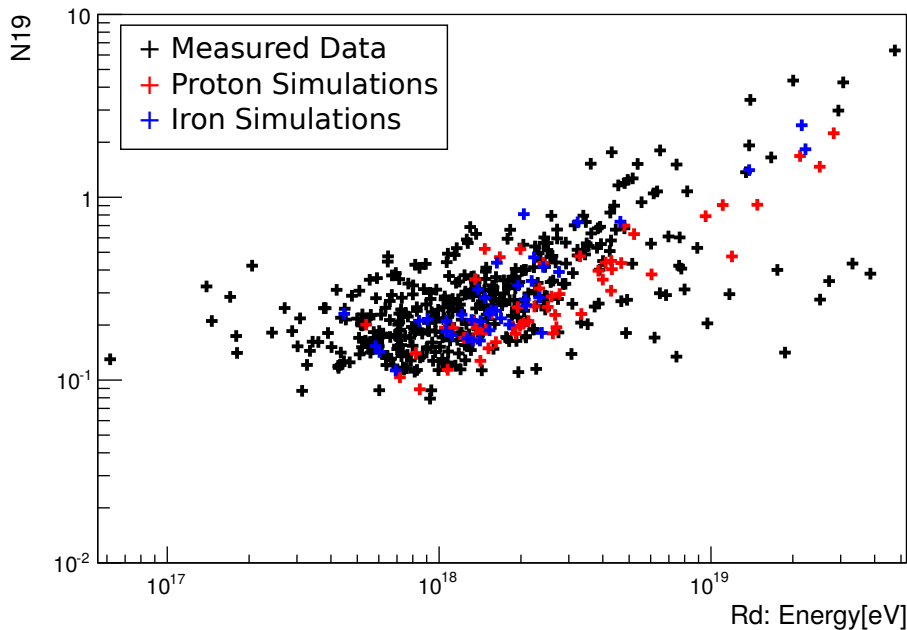


Figure 8.16.: The RD energy is plotted against the N19 energy estimator of the RdHASObserver events. The measured data is drawn in black, proton simulations are drawn in red and iron simulations are drawn in blue.

CoREAS, but not all simulated events could be reconstructed with Offline. The reason for this is that not all events below the full efficiency threshold of SD can be reconstructed by the SD HAS reconstruction. In iron-induced showers more muons are produced than in proton-induced showers, therefore the number of simulated events which could be reconstructed is higher for iron than for proton primaries. If many events would be simulated with varying core and Xmax, but the direction and energy fixed, the problem that simulated events resembling the measured data are not reconstructed could be solved. This is not done because of the high computing time of the CoREAS simulations. For the 51 events which could be reconstructed in data, proton and iron simulations the N19 distribution can be seen in figure 8.19. The showers with N19 below 0.4 can be considered as initiated by lighter and the showers above 0.4 can be considered as initiated by heavier primaries. Here, again

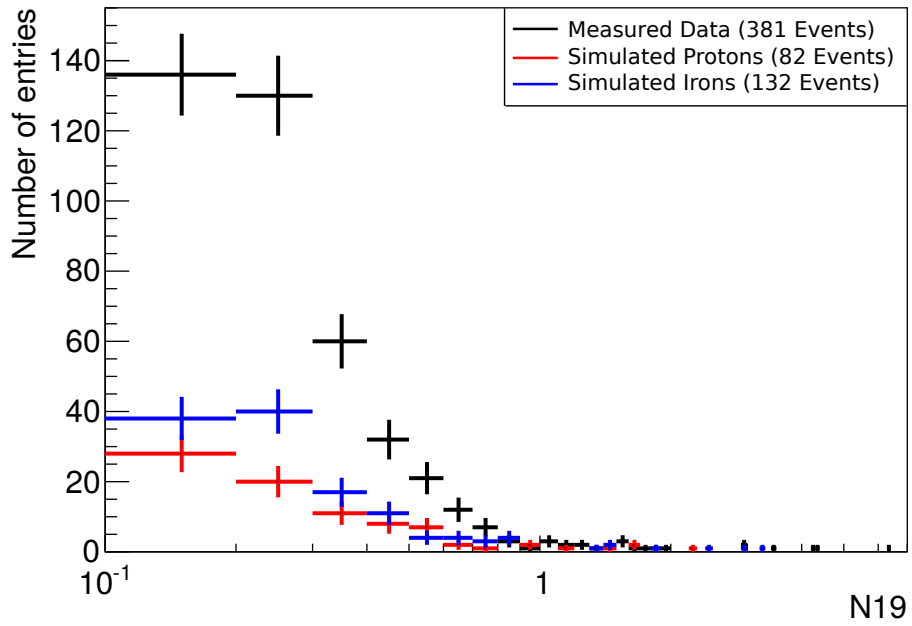


Figure 8.17.: N_{19} histogram of the RdHASObserver events.

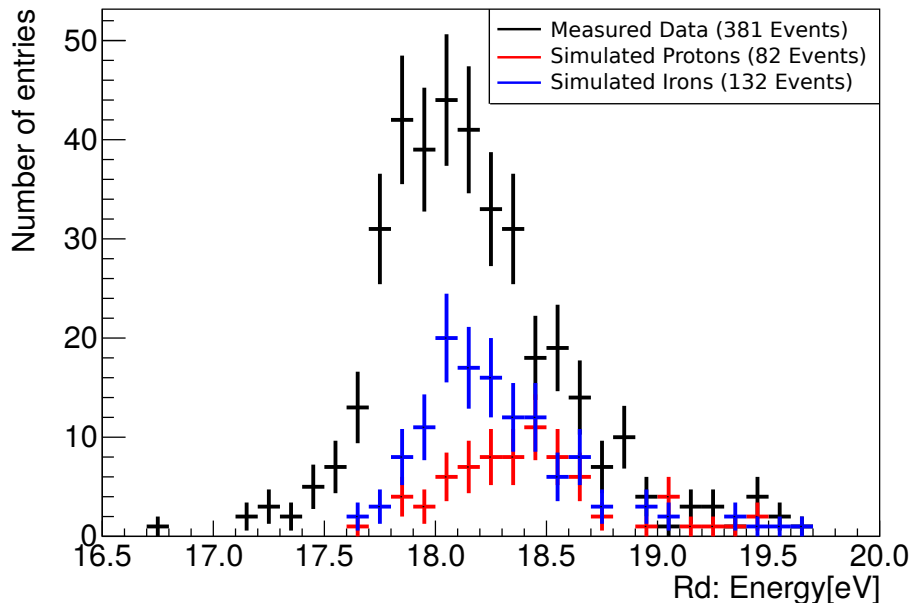


Figure 8.18.: RD energy histogram of the RdHASObserver events.

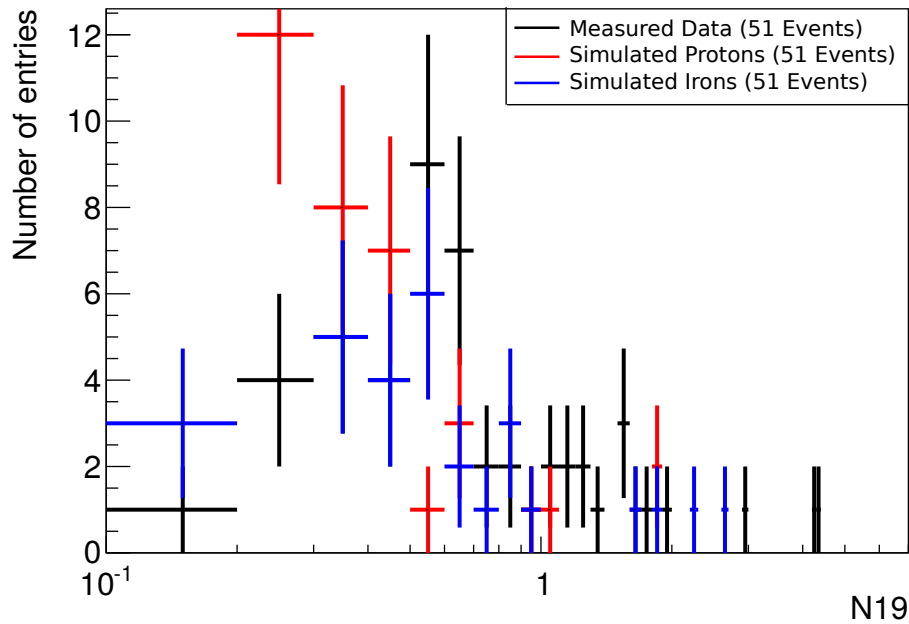


Figure 8.19.: N19 histogram of the RdHASObserver events which could be reconstructed in data, proton and iron simulation.

a larger data sample or an SD HAS Infill reconstruction will improve the separation power of this method. Muon measurements and the energy fraction visible in radio will increase the composition sensitivity by complementary information. In summary, composition measurements by hybrid detection of muons and radio for horizontal air showers seems to be feasible, but needs to be further optimised and elaborated with higher statistics.

8.3. Large-Scale Array of Radio Detectors

Simulation studies showed the feasibility of the radio detection of air showers with a grid size of 750 m [52]. Insights for a large-scale array of radio detectors can be gained with the existing AERA-153 detector. The distance of AERA stations is up to 750 m for the stations deployed on the southern part of the array. The extension of AERA-124 to AERA-153 tripled the sensitive area for horizontal air showers and allows us to test with reasonable statistics the potential of radio detection of horizontal air showers on a large-scale [106]. Higher energetic events are more likely to be detected and the hybrid detection will enable a composition determination. The analysed RdHASObserver data sample covers only half a year of AERA-153 data. In this time period the commissioning of the additional 25 AERA stations was work in progress and the software on the Butterfly stations was updated. Thus, not many events with the additional 25 stations are contained in the present data sample. One example event is shown in figure 8.20. Three of the additional 25 stations were taking data. CoREAS simulations show that all additional 25 stations could have been above the SNR cut for a horizontal air shower (see figure 7.5).

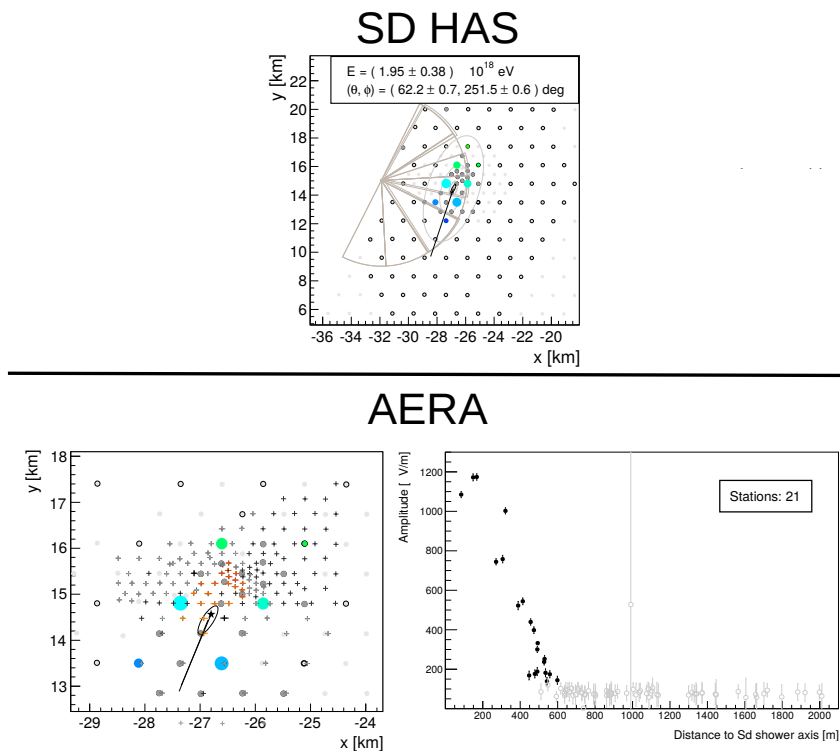


Figure 8.20.: Example event of AERA-153 with installed AERA stations up to a grid size of 750 m are included.

The statistics of events with AERA stations with up to a grid size of 750 m will increase due to the ongoing measurements. The question whether an array in which all radio stations are arranged with a grid size of 750 m is sufficient for detecting horizontal air showers can be answered already with AERA-153. This can be achieved by removing some AERA stations in the reconstruction of the data sample to ensure a grid size of around 750 m. This works because the stations are scalable and not depending on each other. How this looks like can be seen in figure 8.21. The red circles mark the AERA-153 stations considered in the reconstruction. The AERA stations in the upper right corner are self-triggered by scintillators and are not sensitive to horizontal air showers due to the small effective area of the scintillators [107]. The RdHASObserver applied on the AERA data sample of January 1, 2012 to August 15, 2015 considering the grid shown in figure 8.21 results in 411 events. This is about half of the events obtained by applying the RdHASObserver on the data sample with the normal AERA grid. For the modified grid in case one station is not taking data in this time period the distance to the next station will be 1500 m instead of 750 m. This means a stable data acquisition is essential for the detection of horizontal air showers in the energy range of around 10^{18} eV to $10^{18.5}$ eV on a large-scale if a minimum of three stations is required in the reconstruction.

How the example event shown in figure 7.6 looks like for a grid of 750 m AERA stations can be seen in figure 8.22. The original detected event by AERA (see figure 7.6 has an LDF of 75 stations. The modified AERA grid of a grid size of 750 m between the stations leads to an LDF of 18 station. For these kind of events a station grid of 750 m is sufficient to detect them.

Of the reconstructed RdHASObserver events on a large-scale 223 events passed the SD HAS quality cuts. The SD energy distribution of these events can be seen in figure 8.23. The mean value is $10^{18.14}$ eV and is slightly larger than the mean value of the RdHASObserver data sample of 10^{18} eV. This is expected because the larger grid size makes AERA sensitive to events with higher energies. The station multiplicity for the selected events can be seen in figure 8.24. The maximum number of stations is 17, like for the RdObserver data sample in the range of around 0° to 45° of zenith angle (figure 6.3). The station multiplicity and the number of events detected can be increased by an optimised reconstruction for events detected by a large-scale array. The energy estimator described in section 8.1.1 requires five AERA stations for fitting the two-dimensional LDF or three AERA stations if the core is fixed by the SD geometry. Due to the large uncertainties of the SD core determination a simpler approach should be considered to determine the energy on a large-scale with radio detectors. The adaptation of the AERA-153 grid in the reconstruction of measured AERA data shows that detection of horizontal air showers in radio with a grid size of 750 m is feasible.

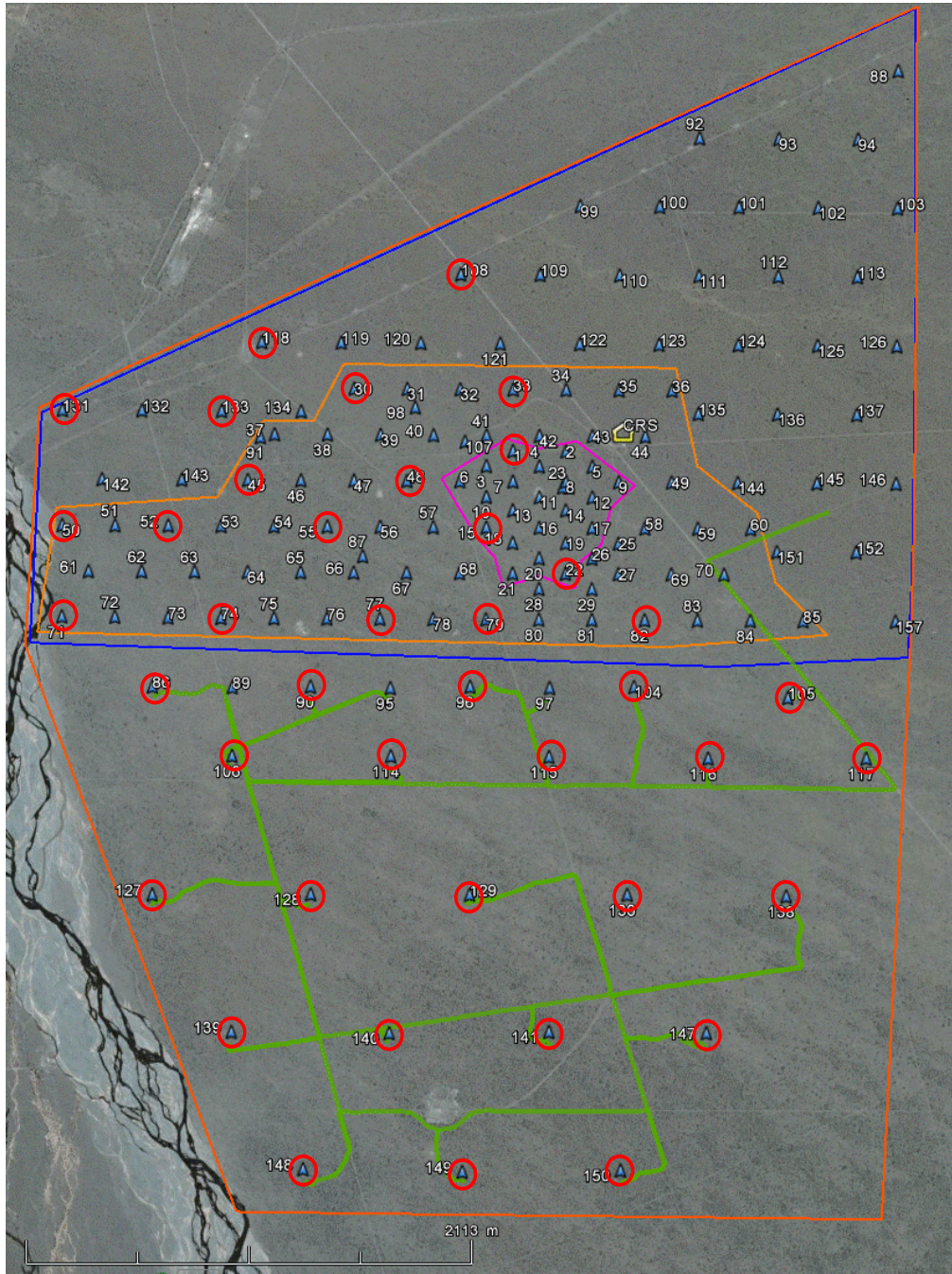


Figure 8.21.: AERA-153 as a large-scale detector with grid size of 750 m. Google Earth map with AERA stations, marked with blue triangles with station numbers and the paths how to reach additional the stations [108]. The borders of AERA-24 are drawn in pink, of AERA-124 are drawn in blue and of AERA-153 are drawn in red. In orange the stations with grid size of smaller than 250 m are framed. The stations marked with red circles are considered for the large-scale array of around 750 m grid size.

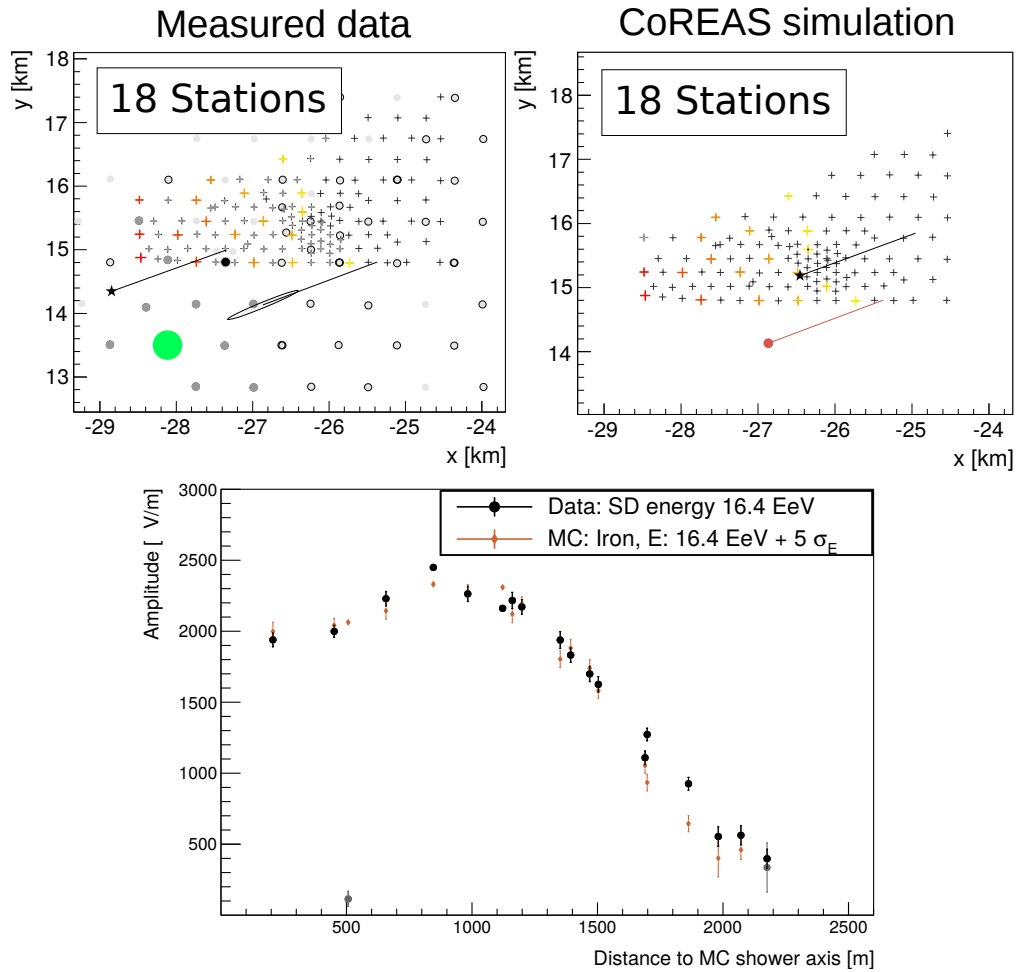


Figure 8.22.: The event already shown in figure 7.6, now reconstructed by a large-scale array where the AERA stations are arranged in a grid of 750 m spacing. On the upper left plot the array of the measured data is shown and on the upper right plot the array for the simulated event with iron primary. The LDF which can be seen on the lower plot consists of data from 18 stations for the measured event and 18 stations for the simulated event (iron primary with $5 \sigma_E$ added to the energy reconstructed by SD, see section 7.5.2). The grid of AERA stations used in the reconstruction can be seen in figure 8.21

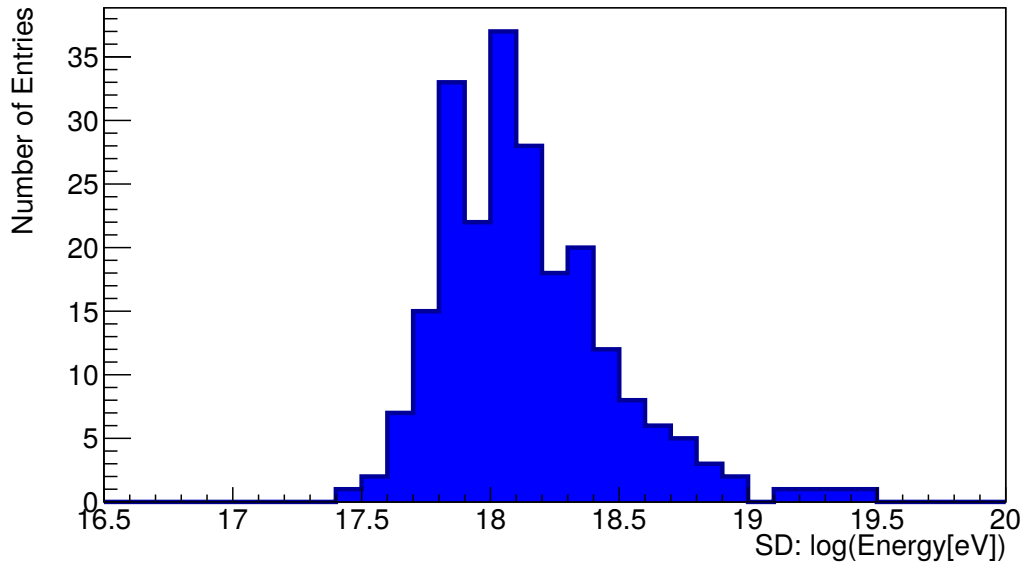


Figure 8.23.: SD energy distribution of the 223 selected RdHASObserver events with the large-scale grid of 750 m. The mean value is $10^{18.14}$ eV.

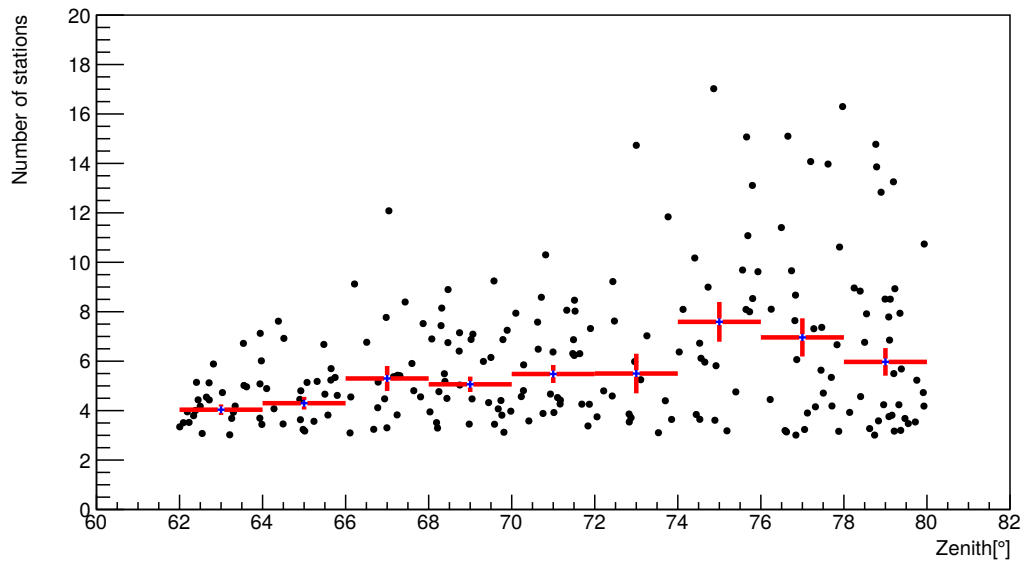


Figure 8.24.: Station multiplicity of the 223 selected RdHASObserver events with the large-scale grid of 750 m. The minimum of three stations is required for a direction reconstruction. The maximum number of stations is 17 for the data sample.

8.4. Detection of Neutrinos

Neutrino-induced air showers can be identified in Auger by looking at the shape and timing behaviour of the signals in the SD tanks or the SD triggering pattern (see section 2.5 for the methodical approach). No neutrino candidate was found in the SD data sample from 1 January 2004 to 20 June 2013. This leads to the 90% C.L. single-flavour limit of the diffuse flux of ultra-high energy neutrinos with an E^{-2} spectrum in the energy range 1.0×10^{17} eV – 2.5×10^{19} eV of $E_\nu^2 dN_\nu/dE_\nu \leq 6.4 \times 10^{-9}$ GeV cm $^{-2}$ s $^{-1}$ sr $^{-1}$ [54]. The zenith angle range is 60° to 75° and 75° to 90° for down-going neutrinos and 90° to 95° for earth-skimming neutrinos.

AERA is sensitive in this energy range and the detection of horizontal air showers is possible on a larger scale as shown in the last section. Therefore, the radio detection of horizontal air showers could contribute to the search for neutrino-induced air showers at Auger. With radio the energy of the shower could be determined from the electromagnetic component independent from the interaction or starting point of the shower (close by or already died out).

To study how the LDF of neutrino-induced air showers detected by AERA would look like two CoREAS simulation sets were generated with electron neutrino primaries resembling the measured events of the RdHASObserver selection. Due to the small cross section of neutrinos the vertical interaction height of the CORSIKA shower has to be fixed for the simulations. A value of 5 km and 12.345 km has been chosen for the vertical height of the first interaction of the neutrino-induced showers. There is no official Offline reconstruction available for the reconstruction of neutrino-induced showers, thus no SD HAS quality cuts were applied on the reconstructed simulated events. The zenith angle range of 60 to 95° is considered for the detection of neutrino-induced air shower in Auger (see section 2.5).

Of the 866 reconstructed RdHASObserver events without SD HAS quality cuts applied 409 simulated events with neutrino primaries with an interaction height of 5 km and 840 simulated events with neutrino primaries with an interaction height of 12.345 km can be reconstructed with AERA when noise is added (see section 6.3). The station multiplicity of the simulated events with neutrino primaries at 5 km interaction height can be found in figure 8.25 and the simulated events with neutrino primaries at 12.345 km interaction height in figure 8.26. Zenith angles of 25° to 95° can be reconstructed for the data sets and station multiplicities of 3 to 80 AERA stations. The footprints of neutrino-induced showers with energies and direction resembling the measured RdHASObserver events are detectable with several AERA stations.

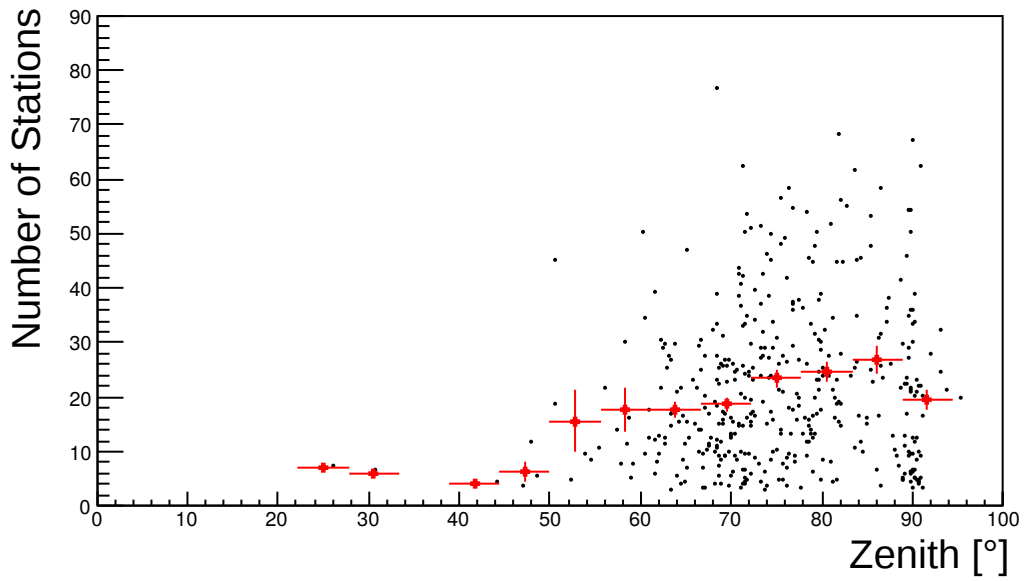


Figure 8.25.: Station multiplicity of the simulated events with neutrino primaries with interaction height at 5 km. 409 simulated events could be reconstructed with noise in AERA.

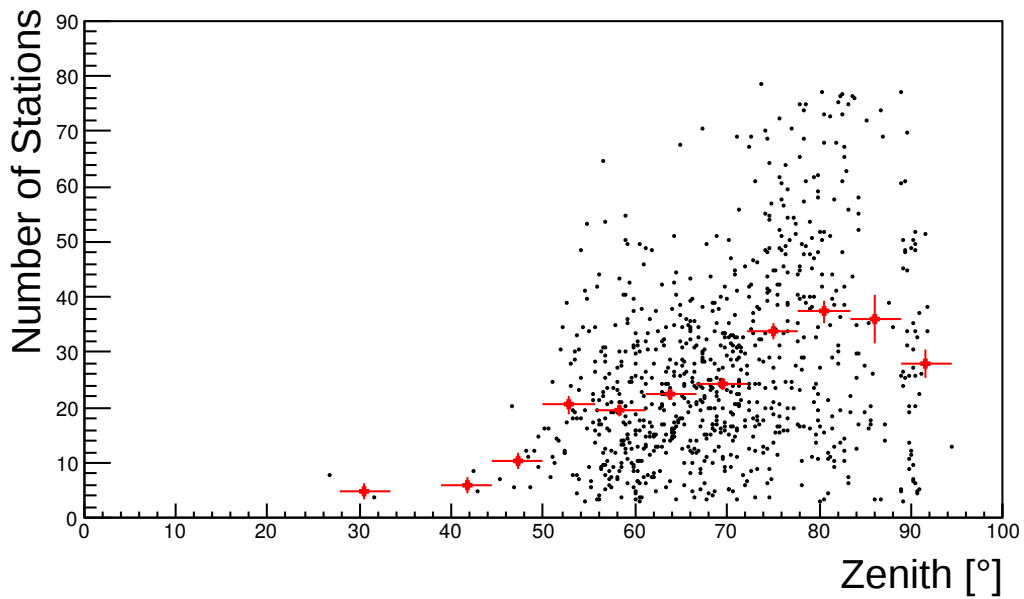


Figure 8.26.: Station multiplicity of the simulated events with neutrino primaries with interaction height at 12.345 km. 840 simulated events could be reconstructed with noise in AERA.

To the LDF of the example event shown in figure 7.6 now the two LDFs of the simulated events with neutrino-induced air showers can be added. In figure 8.27 the LDF of the measured event and the LDFs of the simulated events with proton, iron and neutrino primaries can be seen. The LDF of a simulated event with neutrino primary at the interaction height of 5 km will be called young neutrino-induced shower in the following. The LDF of the simulated event with neutrino primary at the interaction height of 12.345 km has a similar shape as the simulated events with proton and iron primaries but has a different slope at the edge of the LDF. The neutrino induced shower with interaction height at 12.345 km could develop over a longer distance before it reaches the detector compared to the neutrino-induced shower with an interaction height of 5 km and has therefore a broader LDF and will be called old neutrino-induced shower in the following.

The amplitude comparisons of neutrino-induced air showers and simulated events

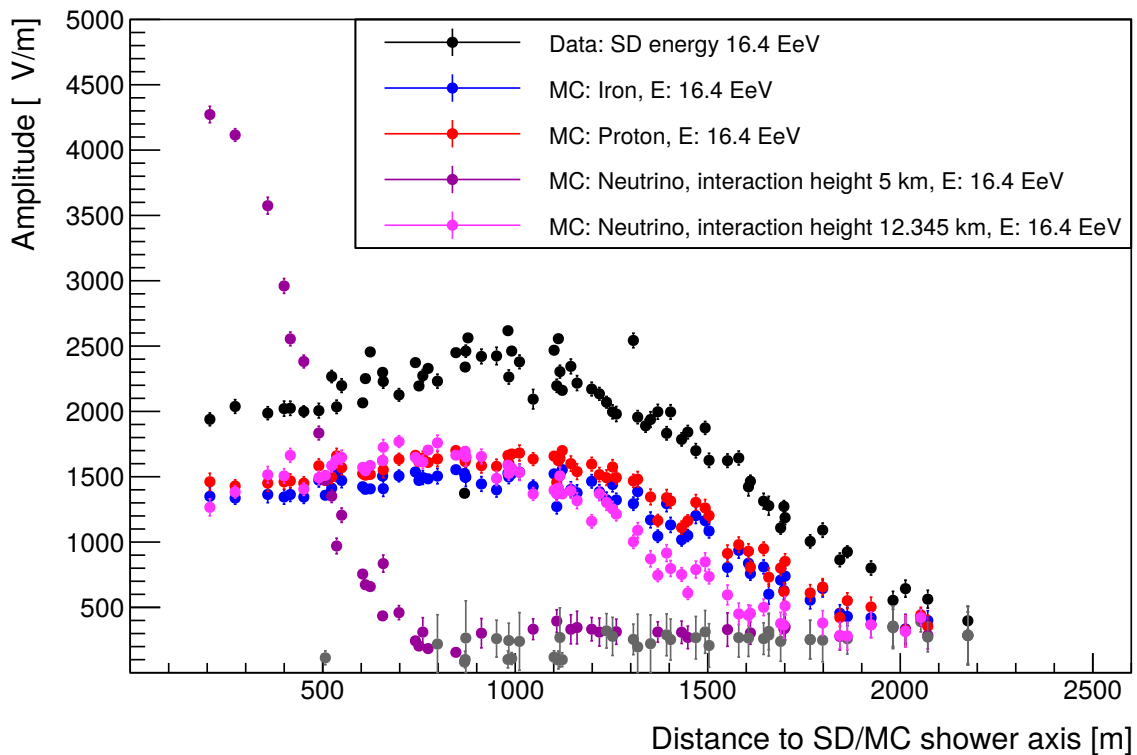


Figure 8.27.: Measured event shown in figure 7.6. The LDFs of simulated events for proton (in red), iron (in blue) and neutrino primaries with an interaction height of 5 km (in violet) and with an interaction height of 12.345 km (in pink) can be seen.

with proton primaries can be seen in figure 8.28. The scatter of the data point is much larger than for the amplitude comparison of simulated events with proton and

8. Physics with Horizontal Air Showers Detected by AERA

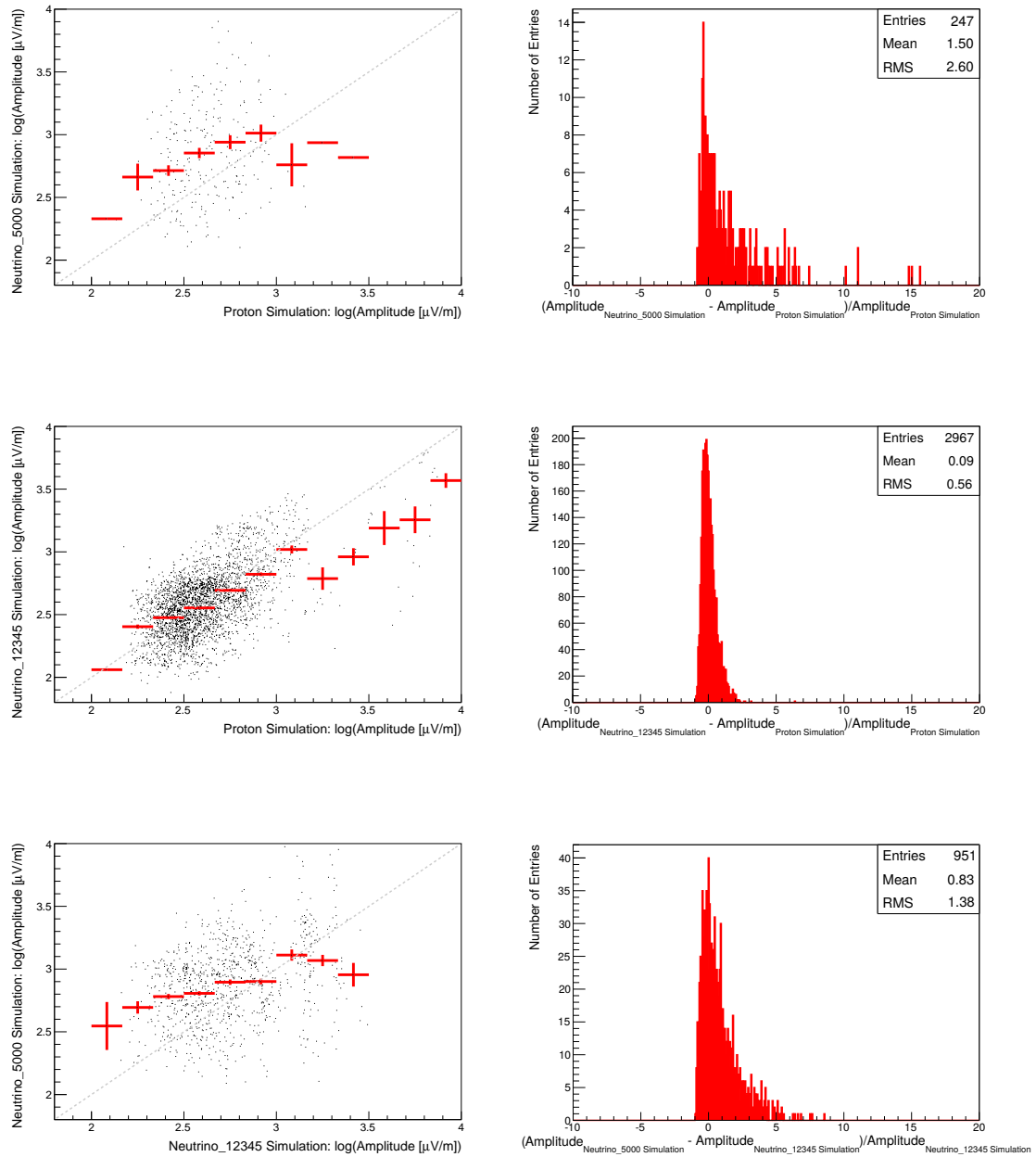


Figure 8.28.: Amplitude comparison of simulated events with neutrino primaries with an interaction height of 5 km and simulated events with proton primaries in the upper plots. The plots in the middle show an amplitude comparison of simulated events with neutrino primaries with an interaction height of 12.345 km and simulated events with proton primaries. The lower plots show an amplitude comparison of simulated events with neutrino primaries with an interaction height of 12.345 km and simulated events with neutrino primaries with an interaction height of 5 km.

iron primaries (see figure 8.13). The mean value of the relative difference of simulated events with neutrino primaries and simulated events with proton primaries is 1.51 for the young neutrino-induced showers and 0.09 for the old neutrino-induced showers. This means a young neutrino-induced shower would be easier to distinguish from a proton-induced shower by the shape of the LDF than an older neutrino-induced shower. Additionally, a young neutrino-induced shower has a smaller footprint, therefore fewer amplitudes of AERA stations can be compared with the amplitudes of simulated events with proton primaries and the number of entries is lower in the right upper plot in figure 8.28 than for the old neutrino shower in figure 8.28 in the middle right plot. The mean value of the relative difference of simulated events with young and old neutrino-induced showers is 0.83. This means young and old neutrino-induced showers could easily be distinguished by the LDF. Together with a hybrid detector like SD which measures the muonic component of the horizontal air shower, radio which would measure the electromagnetic component, would be a complementary detector to search for neutrino-induced showers. Detecting a young horizontal air shower with electromagnetic and muonic component would be a signal of a neutrino-induced air shower.

8.5. Summary

In this chapter the physics with horizontal air showers detected by AERA showed that

- a preliminary energy estimator for horizontal air showers could be established with an relative difference of 49% for the RdHASObserver data sample (combined uncertainties of SD and RD).
- applying the preliminary energy estimator for horizontal air showers on simulated events resembling the RdHASObserver data sample results in the relative difference of 22% of the energy estimation for proton primaries and 21% of energy estimation for iron primaries for radio alone.
- cross checks with FD events lack of low statistics of SD-FD-RD events. This can be improved by implementing an SD HAS reconstruction for the SD Infill.
- simulated events with proton and iron primaries differ on the 1% level in the amplitude for horizontal air showers. This makes the composition determination with radio alone difficult.
- the composition determination with the energy estimator of SD and the preliminary energy estimator with radio suffers of low statistics of reconstructible simulated events below the full efficiency of the SD HAS reconstruction. Here, again a SD HAS reconstruction for the SD Infill would improve the situation. Probably it will be provided by the Pierre Auger Collaboration in near future.
- a large-scale detection of horizontal air showers on a grid size of 750 m is possible. This has been shown with the AERA-153 data sample by modifying the AERA station map in the reconstruction of measured events selected by the RdHASObserver. Half of the events, and almost all high-energy events could be reconstructed with the artificial large-scale grid of AERA.
- the detection of neutrino-induced air showers is possible with AERA. Simulated events with neutrino primaries show a different shape for young and old neutrino-induced air showers. The LDF of a young neutrino-induced air shower differs from proton-induced and iron-induced air showers. The search for neutrino-induced air showers in a hybrid detection mode would profit from the radio detection measuring the electromagnetic component of the air shower.

9. Conclusion

In this thesis, the radio detection of horizontal air showers was studied. Due to the various sources of uncertainties and the fact that signals of horizontal air showers detected by radio detectors were not analysed for this zenith angle range before, the analyses made in this work were mainly data driven and compared only partly to simulations. Preparatory studies before the full data taking with calibrated and extended AERA helped to evaluate the potential of horizontal air showers. If applying loose cuts on the distance and the energy of the reconstructed cosmic ray air showers, about 30% of the events triggered by SD and detected by AERA found the highest pulse in a time window of $2 \mu\text{s}$ for vertical events and $7 \mu\text{s}$ for horizontal events in the time difference of measured and expected time. By hardening the cuts to higher energy and closer distance this efficiency could be considerably increased. This study helped to define the search window for the cosmic ray pulses in the Offline reconstruction pipeline of AERA data. After deploying tripole stations to measure the horizontal polarisation component of the electric field vector on the Auger site some hardware problems led to the detection of low-quality data. However, it contributed to the cognition that the measurement of the horizontal polarisation component of the signal is not necessarily needed to detect horizontal air showers. The deployed low-frequency station was working fine as planned. The predicted suppression of the noise background during night could not be confirmed which makes the detection of cosmic rays with low-frequency antennas difficult.

The missing reconstruction of horizontal air showers for the SD Infill reduced the number of possible reconstructed events at the AERA data sample. The reconstruction of horizontal air showers with a SD grid of 1500 m instead of 750 m led to higher uncertainties in energy and core position harming the analyses. Nevertheless, the reconstruction of the AERA data sample regarding horizontal air showers showed that the reconstructed events have a higher station multiplicity and this means the footprint of the air shower is larger than for vertical events. This is expected by simulations but confirmed experimentally for the first time.

A standard reconstruction for horizontal air showers was established for AERA. The analysis of horizontal air showers revealed the feasibility of the detection of horizontal air showers with radio detectors for zenith angles larger than 60° . Events were detected with reconstructable radio signals up to distances of 5 km. The characteristic shape of the lateral distribution function of horizontal air showers with the plateau of the Cherenkov cone valley, the elliptic shape and the sharp cut-off makes the studies of the lateral distribution more complex than for vertical events.

The amplitudes and the shape of the footprint could be reproduced with CoREAS simulations. The comparison with simulations showed that the lateral distribution function is sensitive to the core position of the shower and to the energy of the primary particle. With extended simulation studies the core and energy uncertainty in future can be reduced with radio.

Horizontal air showers are less sensitive to the composition of cosmic rays, which makes them a good estimator for the energy of the primary particle. An energy estimator for horizontal air showers was introduced and discussed. The relative uncertainty results in 49% for the RdHASObserver data sample, which is higher than the relative uncertainty of 29% for the AERA-24 data sample of vertical events. Considering the larger uncertainties of the SD reconstruction and possibility to optimise the fitting parameters of the two-dimensional lateral distribution function fit this uncertainty can be reduced by further improvements of the method. Applying the energy estimator for horizontal events to simulated events with proton and iron results in the relative uncertainty of 22% for proton and 21% for iron primaries. The cross check with superhybrid events detected by SD, FD and AERA lacked by the low statistic. In the future with a larger measurement period of AERA-153 this situation will be improved.

A composition determination of the horizontal air shower data sample with the energy estimator N19 of SD suffered again by the low statistics of reconstructable simulated events below the full efficiency of the SD HAS reconstruction. However, since the detected amplitudes of horizontal air showers are less depending on the composition of the cosmic ray shower, a higher precision in the coverage of the radio footprint is needed.

It was shown that a large radio detection of horizontal air showers on a grid size of 750 m is possible. This was shown with the AERA-153 data sample by modifying the AERA station map in the reconstruction of measured events.

In addition, it was found that the detection of neutrino-induced air showers is possible with AERA. Simulated events with neutrino primaries interacting late in the atmosphere show a different lateral distribution function than simulated events with neutrino primaries interacting early in the atmosphere or proton or iron primaries. In the search for neutrino-induced air showers a hybrid detector would profit by a radio detector measuring the electromagnetic component of air the shower.

A future GRAND experiment is in its design phase order to detect neutrino-induced cosmic air showers with around 1,000,000 radio detectors spread over 200,000 km². Believing common source models of neutrino-induced air showers the achieved sensitivity will be sufficient to first detect ultra-high energy cosmogenic neutrinos.

AERA located at the Pierre Auger Observatory provides unique opportunities for the detection of horizontal air showers and horizontal air showers should be further studied to answer some of the important questions the physics of cosmic rays raised.

Bibliography

- [1] V. F. Hess, Über Beobachtungen der durchdringenden Strahlung bei sieben Freiballonfahrten, *Physikalische Zeitschrift* 13: 1084–1091, 1912.
- [2] Nobel Lectures, Physics 1922-1941, Elsevier Publishing Company, Amsterdam, 1965.
- [3] S. H. Neddermeyer and C. D. Anderson, Note on the Nature of Cosmic-Ray Particles, *Physical Review* 51, S. 844, 1937.
- [4] G. P. S. Occhialini and C. F. Powell, Nuclear Disintegrations Produced by Slow Charged Particles of Small Mass, *Nature* 159, 186–190 & 160, 453–456, 1947.
- [5] G.D. Rochester and C.C. Butler, Evidence for the Existence of New Unstable Elementary Particles, *Nature* 160 (4077): 855–857, 1947.
- [6] Carl D. Anderson, The Positive Electron, *Physical Review* 43, S. 491, 1933.
- [7] LHC Machine, JINST 3 (2008) S08001.
- [8] A. Aab et al. [Pierre Auger Collaboration], The Pierre Auger Cosmic Ray Observatory, *Nucl.Instrum.Meth.* A798 (2015) 172-213.
- [9] A. Aab et al. [The Pierre Auger Collaboration], The Pierre Auger Observatory Upgrade - Preliminary Design Report, arXiv:1604.03637v1.pdf, 2016.
- [10] P. Abreu et al. [The Pierre Auger Coll.], Antennas for the Detection of Radio Emission Pulses from Cosmic-Ray induced Air Showers at the Pierre Auger Observatory, *JINST* 7 (2012) P10011.
- [11] T. Huege et al. [The LOPES Collaboration], The LOPES experiment—recent results, status and perspectives, *Nucl.Instrum.Meth.* A662 (2012) S72-S79.
- [12] J. Petrovic et al. [The LOPES Collaboration], Radio emission of highly inclined cosmic ray air showers measured with LOPES, *Astron.Astrophys.* 462 (2007) 389-395.
- [13] T. Antoni et al. [The KASCADE Collaboration], The Cosmic-Ray Experiment KASCADE, *Nucl.Instr. and Meth* A513 (2003) 490-510.

- [14] W. D. Apel et al. [The KASCADE Collaboration], The spectrum of high-energy cosmic rays measured with KASCADE-Grande, *Nucl. Instr. and Meth.* A513 (2010) 202.
- [15] H. Kawai et al. [Telescope Array Collaboration], *Nucl. Phys. B - Proc. Suppl.* 175-176, 221 (2008).
- [16] G.B. Thomson, Results from the Telescope Array Experiment, *PoS ICHEP2010* (2010) 448.
- [17] B.V. Antokhanov et al [The Tunka Collaboration], Tunka-133: preliminary results from the first year of operation, *Nuclear Physics B (Proc. Supp.)*, 2011, 212-213: 53-58.
- [18] P.A. Bezyazeev, et al. [The Tunka-Rex Collaboration], Radio measurements of the energy and the depth of the shower maximum of cosmic-ray air showers by Tunka-Rex, *JCAP* 1601 (2016) no.01, 052.
- [19] Olivier Martineau-Huynh et al., The Giant Radio Array for Neutrino Detection, 10.1051/epjconf/201611603005, 2015.
- [20] O. Kambeitz for the Pierre Auger Coll., Radio Detection of Horizontal Extensive Air Showers with AERA, *Proc. ARENA 2014*, Annapolis, USA, AIP Conf. Proc., to be published [arXiv:1509.08289].
- [21] J. Blümer, R. Engel, J. Hörandel, Cosmic Rays from the Knee to the Highest Energies, *Prog.Part.Nucl.Phys.* 63 (2009) 293-338.
- [22] H. Hu, Status of the EAS studies of cosmic rays with energy below 10^{16} eV, *Proc. of the 31rd ICRC 2009*, Łódź, Poland.
- [23] T. Huege, Radio detection of cosmic ray air showers in the digital era, *Phys.Rept.* 620 (2016) 1-52.
- [24] R. Engel, D. Heck, T. Pierog, Extensive air showers and hadronic interactions at high energy, *Ann. Rev Nucl. Part. Sci.* 61 (2011) 467-489.
- [25] P. M. Hansen, J. Alvarez-Muniz, R. A. Vazquez, A comprehensive study of shower to shower fluctuations, *Astroparticle Physics*, Volume 34, Issue 6, January 2011, Pages 503-512.
- [26] A. Haungs, H. Rebel, and M. Roth., Energy spectrum and mass composition of high-energy cosmic rays, *Rept.Prog.Phys.* 66 (2003) 1145-1206.
- [27] R. Engel, Composition Results from Auger, HAP Workshop COMPOSITION, Karlsruhe, 2015.

-
- [28] D. Ardouin et al., Radio-detection signature of high-energy cosmic rays by the CODALEMA experiment, *Nucl.Instrum.Meth.* A555 (2005) 148.
- [29] A. Aab et al. [The Pierre Auger Collaboration] Probing the radio emission from air showers with polarization measurements. *Phys. Rev.*, D89(5):052002, 2014.
- [30] D. Ardouin et al. [The CODALEMA Collaboration], Geomagnetic origin of the radio emission from cosmic ray induced air showers observed by CODALEMA, *Astropart.Phys.* 31 (2009) 192-200.
- [31] A. Zilles, private communication.
- [32] A. Aab et al. [The Pierre Auger Collaboration], Energy Estimation of Cosmic Rays with the Engineering Radio Array of the Pierre Auger Observatory, Submitted to: *Phys.Rev.D*, arXiv:1508.04267.
- [33] A. Aab et al. Nanosecond-level time synchronization of autonomous radio detector stations for extensive air showers. *JINST*, 11(01):P01018, 2016.
- [34] A. Bellétoile et al. [The CODALEMA Collaboration], Evidence for the charge-excess contribution in air shower radio emission observed by the CODALEMA experiment, *Astropart.Phys.* 69 (2015) 50-60.
- [35] P. Schellart et al., Detecting cosmic rays with the LOFAR radio telescope, *Astron.Astrophys.* 560 (2013) A98.
- [36] A. Nelles et al., A parameterization for the radio emission of air showers as predicted by CoREAS simulations and applied to LOFAR measurements, *Astropart.Phys.* 60 (2014) 13-24.
- [37] S. Buitink et al., A large light-mass component of cosmic rays at 10^{17} - $10^{17.5}$ eV from radio observations, *Nature* 531 (2016) 70.
- [38] H. Falcke et al. [The LOPES Collaboration], Detection and imaging of atmospheric radio flashes from cosmic ray air showers, *Nature* 435 (2005) 313-316.
- [39] D. Huber, Analysing the electric field vector of air shower radio emission, Doctoral thesis, KIT, 2014.
- [40] D. Ardouin et al., First detection of Extensive Air Showers by the TREND self-triggering radio experiment, *Astropart.Phys.* 34 (2011) 717-731.
- [41] D. Kostunin et al., Reconstruction of air-shower parameters for large-scale radio detectors using the lateral distribution, *Astropart.Phys.* 74 (2016) 79-86.

- [42] O. Martineau-Huynh et al. [The GRAND Collaboration], The Giant Radio Array for Neutrino Detection, EPJ Web Conf. 116 (2016) 03005.
- [43] GRAND workshop, Paris, France, 2015.
- [44] A. Aab et al. [The Pierre Auger Collaboration], Muons in air showers at the Pierre Auger Observatory: Mean number in highly inclined events, Phys.Rev. D91 (2015) no.5, 059901.
- [45] H. Dembinski, Measurement of the flux of ultra high energy cosmic rays using data from very inclined air showers at the Pierre Auger Observatory, Doctoral thesis, RWTH Aachen, 2009.
- [46] A. Aab et al. [The Pierre Auger Collaboration], Reconstruction of inclined air showers detected with the Pierre Auger Observatory, JCAP 1408 (2014) no.08, 019.
- [47] A. Aab et al. [The Pierre Auger Collaboration], Measurement of the cosmic ray spectrum above 4×10^{18} eV using inclined events detected with the Pierre Auger Observatory, JCAP 1508 (2015) 049.
- [48] J.Tiffenberg, UHE Neutrino searches with the Pierre Auger Observatory, <http://users.ictp.it/smr2246/monday/tiffenberg-NUSKY.pdf>.
- [49] M. Roth, Composition Results from Auger, HAP Workshop COMPOSITION, Karlsruhe, 2015.
- [50] E. Holt, private communication.
- [51] T. Huege and C. W. James, Full Monte Carlo simulations of radio emission from extensive air showers with CoREAS, Proc. of the 33rd ICRC 2013, Rio de Janeiro, Brazil.
- [52] E. Holt, Simulationsstudie für ein großskaliges Antennenfeld zur Detektion von Radioemission ausgedehnter Luftschauer, Diploma thesis, KIT, 2013.
- [53] P. Abreu et al. [The Pierre Auger Collaboration], A search for ultra-high energy neutrinos in highly inclined events at the Pierre Auger Observatory, Phys.Rev. D84 (2011) 122005.
- [54] A. Aab et al. [The Pierre Auger Collaboration], An improved limit to the diffuse flux of ultra-high energy neutrinos from the Pierre Auger Observatory, Phys.Rev. D91 (2015) no.9, 092008.
- [55] P. Abreu et al. [The Pierre Auger Collaboration], The Pierre Auger Observatory V: Enhancements, Proc. 32nd ICRC 2011, Beijing, China.

- [56] T. Winchen, Detector components of the Pierre Auger Observatory, Malargue Argentina, https://en.wikipedia.org/wiki/File:PierreAugerObservatory_DetectorComponents.jpg, accessed December 8, 2015.
- [57] J. Abraham et al. [Pierre Auger Collaboration], Trigger and aperture of the surface detector array of the Pierre Auger Observatory, *Nucl.Instrum.Meth. A613* (2010) 29-39.
- [58] D. Ravnani for the Pierre Auger Collaboration, Measurement of the energy spectrum of cosmic rays above 3×10^{17} eV using the AMIGA 750 m surface detector array of the Pierre Auger Observatory, Proc. of the 33rd ICRC 2013, Rio de Janeiro, Brazil.
- [59] Pierre Auger Collaboration, https://www.auger.org/images/Observatory/SD_-2pics.png, accessed April 26, 2016.
- [60] J. Abraham et al. [The Pierre Auger Collaboration], The Fluorescence Detector of the Pierre Auger Observatory, *Nucl.Instrum.Meth. A620* (2010) 227-251.
- [61] Pierre Auger Collaboration, https://www.auger.org/images/Observatory/FD_-2pics.png, accessed April 26, 2016.
- [62] A. Aab et al. [The Pierre Auger Coll.], Prototype muon detectors for the AMIGA component of the Pierre Auger Observatory, *JINST 11* (2016) no.02, P02012.
- [63] E. Holt for the Pierre Auger Coll., The Auger Engineering Radio Array and multi-hybrid cosmic-ray detection, Proc. TAUP Conference 2015, Torino, Italy, 2015.
- [64] A. Almela, private communication.
- [65] D. Charrier, Design of a low noise, wide band, active dipole antenna for a cosmic ray radiodetection experiment, *Antennas and Propagation Society International Symposium*, pp. 4485 - 4488, 9-15 June 2007.
- [66] R. Krause, Horizontal Antenna, Auger Collaboration Meeting, Malargue, Argentina, 2014.
- [67] E. Holt, private communication.
- [68] F. Schröder for the Pierre Auger Coll., Radio detection of high-energy cosmic rays with the Auger Engineering Radio Array (PISA 2015), DOI: 10.1016/j.nima.2015.08.047.

- [69] S. Argiro, et al., The Offline Software Framework of the Pierre Auger Observatory, Nucl.Instrum.Meth. A580 (2007) 1485-1496.
- [70] D. Heck et al., Forschungszentrum Karlsruhe Report FZKA 6019 (1998).
- [71] A. Ferrari et al, FLUKA: a multi-particle transport code, CERN-2005-10 (2005), INFN/TC_0511, SLAC-R-773.
- [72] S. Ostapchenko, Monte Carlo treatment of hadronic interactions in enhanced Pomeron scheme: I. QGSJET-II model, Phys.Rev. D83 (2011) 014018.
- [73] T. Huege, M. Ludwig, C.W. James, Simulating radio emission from air showers with CoREAS, AIP Conf.Proc. 1535 (2013) 128.
- [74] R. Brun and F. Rademakers, ROOT - An Object Oriented Data Analysis Framework, Proceedings AIHENP conference, Lausanne, 1996, Nucl. Inst. & Meth. in Phys. Res. A 389 (1997) 81-86.
- [75] P. Abreu et al. [The Pierre Auger Collaboration], Advanced functionality for radio analysis in the Offline software framework of the Pierre Auger Observatory, Nucl.Instrum.Meth. A635 (2011) 92-102.
- [76] P. A. Bezyazeev et al. [The Tunka-Rex Collaboration], Radio measurements of the energy and the depth of the shower maximum of cosmic-ray air showers by Tunka-Rex, JCAP01(2016)052, 2016.
- [77] A. Nelles, Radio emission of air showers, Doctoral thesis, Radboud University Nijmegen, 2014.
- [78] D. Heck and T. Pierog, Extensive Air Shower Simulations with CORSIKA: A User's Guide, 2016.
- [79] J. Knapp, On Hidden Uncertainties (in CORSIKA), HAP Workshop COMPOSITION, Karlsruhe, 2015.
- [80] T. Huege, Simulation of radio signals with CoREAS, CORSIKA School, Freudenstadt, 2014.
- [81] M. Melissas and T. Huege, Comparison of the AERA event 100220/35479 with CoREAS simulations, GAP Note 2013-046.
- [82] H. Schoorlemmer et al., Detailed comparison of ZHaireS simulation and measured radio signals for event 20666019, Gap Note 2013-044.
- [83] C. W. James et al, General description of electromagnetic radiation processes based on instantaneous charge acceleration in 'endpoints', Phys.Rev. A84 (2011) 056602.

- [84] A. A. Al-Rubaiee and A. Jumaah, Estimation of Lateral Distribution Function in Extensive Air Showers by Using AIRES Simulation System, *Int.J.Appl.Nat.Sci.* 2 (2013) 41-44.
- [85] J. Alvarez-Muniz, W. R. Carvalho and E. Zas, Monte Carlo simulations of radio pulses in atmospheric showers using ZHAireS, *Astropart.Phys.* 35 (2012) 325-341.
- [86] K. Belov et al. [The T-510 Collaboration], Accelerator measurements of magnetically-induced radio emission from particle cascades with applications to cosmic-ray air showers, *Phys.Rev.Lett.* 116 (2016) no.14, 141103.
- [87] A. Nelles et al., A parameterization for the radio emission of air showers as predicted by CoREAS simulations and applied to LOFAR measurements, *Astropart.Phys.* 60 (2014) 13-24.
- [88] O. Kambeitz, Update on the efficiency, AERA Analysis Meeting, Paris, France, 2013.
- [89] O. Krömer, Active Short Wave Antenna for the Detection of the 3-dimensional E-field Vector generated by the Radio Emission of Cosmic Ray Air Showers, internal note, 2013.
- [90] D. Huber, private communication.
- [91] D. Huber et al. [The LOPES Collaboration], LOPES 3D reconfiguration and first measurements, *Proc. 32rd ICRC 2011*, Beijing, China.
- [92] R. Krause, private communication.
- [93] P. Kessler, Untersuchung des Hintergrundrauschens und Suche nach Radiosignalen kosmischer Strahlung im Frequenzbereich 1.5-6.5 MHz bei AERA, Bachelor thesis, KIT, 2016.
- [94] ITU, Recommendations and reports of the CCIR (1982) - Rep 670: Worldwide minimum external noise levels, 0.1 Hz to 100 GHz, volume I (Spectrum utilization and monitoring).
- [95] J. Neuser, Cosmic Rays and the Atmospheric Electric Field, Doctoral thesis, Bergische Universität Wuppertal, 2015.
- [96] A. Schulz for the Pierre Auger Collaboration, The measurement of the energy spectrum of cosmic rays above 3×10^{17} eV with the Pierre Auger Observatory, *Proc. of the 33rd ICRC 2013*, Rio de Janeiro, Brazil.

- [97] J. Maller for the Pierre Auger Coll., Technological developments for the Auger Engineering Radio Array (AERA), Proc. ARENA 2014, Annapolis, USA, AIP Conf. Proc., to be published.
- [98] I. Valino et al., Characterisation of the electromagnetic component in ultra-high energy inclined air showers, *Astropart.Phys.* 32 (2010) 304-317.
- [99] A. Nelles, J. Schulz, and J. Hörandel, A parameterization for the radio signal measured with AERA, 2014, GAP-2014-073.
- [100] J. Schulz, Cosmic Radiation, Doctoral thesis, Radboud University Nijmegen, 2016.
- [101] W. D. Apel et al. [The LOPES Collaboration], Reconstruction of the energy and depth of maximum of cosmic-ray air-showers from LOPES radio measurements, *Phys.Rev. D*90 (2014) no.6, 062001.
- [102] T. Huege, M. Ludwig, and C.W. James, Simulating radio emission from air showers with CoREAS, *AIP Conf.Proc.* 1535 (2013) 128.
- [103] J. Schulz et al. [The Pierre Auger Collaboration], The Pierre Auger Observatory: Contributions to the 34th International Cosmic Ray, Conference (ICRC 2015), arXiv:1509.03732, 2015.
- [104] T. Huege, et al., Precision measurements of cosmic ray air showers with the SKA, *PoS AASKA14* (2015) 148.
- [105] T. Huege and Q. Dorosti, Composition sensitivity of SD - RD hybrid HAS measurements, Auger Collaboration Meeting, Malargue, Argentina, 2014.
- [106] A. Haungs and O. Kambeitz, HAS Events at AERA, AugerNext Symposium 2015, Karlsruhe, 2015.
- [107] J. Schulz et al. , The Scintillators of the Auger Engineering Radio Array, GAP-2014-122, 2014.
- [108] H. Bolz, private communication.

Appendix

A. Tables

A.1. ModuleSequence - Data

```
<!-- RdHASObserver Reconstruction of Data. -->
  <loop numTimes="unbounded">
    <module> EventFileReaderOG </module>
    <module> RdEventPreSelector </module>

<!-- Observer/ModuleSequence_SDHAS.xml -->
  <module> SdQualityCutTaggerOG </module>
  <module> SdPMTQualityCheckerKG </module>
  <module> TriggerTimeCorrection </module>
  <module> SdCalibratorOG </module>
  <module> SdStationPositionCorrection </module>
  <module> SdBadStationRejectorKG </module>
  <module> SdSignalRecoveryKLT </module>
  <module> SdEventSelectorOG </module>
  <module> TopDownSelector </module>

<!-- SD reconstruction (HAS) -->
  <module> SdPlaneFitOG </module>
  <module> SdHorizontalReconstruction </module>
  <module> SdHorizontalEventSelectorHOG </module>

<!-- RdHASObserver -->
  <module> RdEventInitializer </module>
  <module> RdStationPositionCorrection </module>
  <module> RdStationRejector </module>
  <module> RdChannelADCToVoltageConverter </module>
  <module> RdChannelSelector </module>
  <module> RdChannelPedestalRemover </module>
  <module> RdChannelResponseIncorporator </module>
  <module> RdChannelBeaconTimingCalibrator </module>
  <module> RdChannelBeaconSuppressor </module>
  <module> RdStationTimingCalibrator </module>
```

```

    <module> RdStationTimeWindowConsolidator    </module>
    <module> RdChannelTimeSeriesTaperer        </module>
    <module> RdChannelBandstopFilter           </module>
    <module> RdChannelUpsampler                 </module>
    <module> RdChannelRiseTimeCalculator        </module>
    <module> RdAntennaChannelToStationConverter </module>
    <module> RdStationSignalReconstructor     </module>
    <module> RdStationEFieldVectorCalculator   </module>

    <loop numTimes="unbounded">
      <module> RdTopDownStationSelector </module>
      <module> RdPlaneFit                </module>
    </loop>

    <module> RdClusterFinder                </module>
    <module> RdPlaneFit                      </module>
    <module> RdStationRiseTimeCalculator     </module>
    <module> RdEventPostSelector            </module>
    <module> RdLDFMultiFitter               </module>
    <module> Rd2dLDFFitter                  </module>

<!-- FD reconstruction -->
    <try>
      <module> FdCalibratorOG                </module>
      <module> FdEyeMergerKG                 </module>
      <module> FdPulseFinderOG               </module>
      <module> FdSDPFinderOG                 </module>
      <module> FdAxisFinderOG                </module>
      <module> HybridGeometryFinderOG        </module>
      <module> HybridGeometryFinderWG        </module>
      <module> FdApertureLightKG             </module>
      <module> FdEnergyDepositFinderKG       </module>
      <module> FdProfileReconstructorKG      </module>
    </try>

    <module> RdStationTimeSeriesWindowCutter </module>
    <module> RdStationTimeSeriesTaperer     </module>
    <module> RdREASSimPreparator            </module>
    <module> EventFileExporterOG            </module>
    <module> RecDataWriterNG                </module>
  </loop>

```

A.2. ModuleSequence - Simulation

```

<!-- RdHASObserver Reconstruction of Simulation. -->
  <loop numTimes="unbounded" pushEventToStack="yes">
    <module> EventFileReaderOG </module>
    <loop numTimes="1" pushEventToStack="yes">
<!-- Radio reconstruction -->
      <module> RdStationAssociator </module>
      <module> RdAntennaStationToChannelConverter </module>
      <module> RdChannelResponseIncorporator </module>
      <module> RdChannelResampler </module>
      <module> RdChannelTimeSeriesClipper </module>
      <module> RdChannelVoltageToADCConverter </module>
      <module> RdChannelNoiseImporter </module>
      <module> RdEventInitializer </module>
      <module> RdStationRejector </module>
      <module> RdChannelADCToVoltageConverter </module>
      <module> RdChannelSelector </module>
      <module> RdChannelPedestalRemover </module>
      <module> RdChannelResponseIncorporator </module>
      <module> RdChannelTimeSeriesTaperer </module>
      <module> RdChannelBandstopFilter </module>
      <module> RdChannelUpsampler </module>
      <module> RdChannelRiseTimeCalculator </module>
      <module> RdAntennaChannelToStationConverter </module>
      <module> RdStationSignalReconstructor </module>
      <module> RdStationEFieldVectorCalculator </module>
      <loop numTimes="unbounded" pushEventToStack="no">
        <module> RdTopDownStationSelector </module>
        <module> RdPlaneFit </module>
      </loop>
      <module> RdPlaneFit </module>
      <module> RdStationRiseTimeCalculator </module>
      <module> RdLDFMultiFitter </module>
      <module> Rd2dLDFFitter </module>
      <module> RdStationTimeSeriesWindowCutter </module>
      <module> RdStationTimeSeriesTaperer </module>
      <module> RecDataWriterNG </module>
    </loop>
  </loop>

```


Danksagung

Ich bedanke mich ganz herzlich bei Prof. Dr. Dr. Blümer für die Möglichkeit am Institut für Kernphysik promovieren zu dürfen und für die Unterstützung bei der Anfertigung dieser Arbeit.

Prof. Dr. Husemann danke ich für die Übernahme des Korreferats und die regelmäßigen Treffen, bei denen er mich die Astroteilchenphysik aus dem Blickwinkel eines Teilchenphysikers sehen lassen hat. Bedanken möchte ich mich auch für konstruktiven Ratschläge zur Analyse und zum Verfassen dieser Arbeit.

Mein ganz besonderer Dank gilt Dr. Andreas Haungs, der mich bereits bei meiner Berufsorientierung am Gymnasium in der Forschungsgruppe LOPES am Institut für Kernphysik betreut hat. Dies hat mich in meinem Entschluss bestärkt Physikerin zu werden. Ich möchte mich für die sehr gute Betreuung und den ansteckenden Optimismus während meiner Promotion bedanken. Die Einblicke, die ich in die Strukturen, Prozesse und Spielregeln der Wissenschaft gewinnen konnte, nehme ich mit auf meinen weiteren Weg.

Bei Dr. Tim Huege möchte ich mich für die Unterstützung bei allen Analyse- und Simulationsfragen bedanken. Die Diskussionen mit Dr. Frank Schröder haben mir immer weiter geholfen das Große und Ganze nicht aus den Augen zu verlieren.

Für die sehr gute Atmosphäre möchte ich mich bei allen Kollegen des Instituts für Kernphysik und des Instituts für Experimentelle Kernphysik bedanken. Dem Admin-Team Klaus Bekk, Doris Wochele und Dieter Manger die mich immer mit den nötigen Ressourcen bezüglich Rechenzeit und Hardware ausgestattet haben, möchte ich meinen Dank aussprechen. Vielen Dank auch an Sabine Bucher, die immer für einen reibungslosen Ablauf in organisatorischen Fragen gesorgt hat.

Ohne die großartige Unterstützung durch meine Familie, besonders durch meinen Mann Manuel, durch meine Eltern Natalia und Artur und meinen Bruder Rainer, wäre diese Arbeit nicht zum erfolgreichen Abschluss gekommen. Vielen Dank, dass ihr immer für mich da seid und euch so gut um Felix gekümmert habt, während ich gearbeitet habe.